DEVELOPMENT OF METAL OXIDE/METAL CARBOXYLATE CHEMISTRY FOR THE SYNTHESIS OF METAL TUNGSTATES, MOLYBDATES, AND FERRITES AND EXTRACTION OF IRON FROM ORES

By
KHALID ALRASHIDI

Bachelor of Science in Chemistry
King Saud University
Riyadh, Saudi Arabia
2012

Master Of Science in Chemistry
Oklahoma State University
Stillwater, Oklahoma
2018

Submitted to the Faculty of the
Graduate College of the
Oklahoma State University
in partial fulfillment of
the requirements for
the Degree of
DOCTOR OF PHILOSOPHY
May, 2022

DEVELOPMENT OF METAL OXIDE/METAL CARBOXYLATE CHEMISTRY FOR THE SYNTHESIS OF METAL TUNGSTATES, MOLYBDATES, AND FERRITES AND EXTRACTION OF IRON FROM ORES

Dissertation Approved:

Dr. Allen W. Apblett

Dissertation Adviser

Dr. Spencer P. Pitre

Dr. Elijah Schnitzler

Dr. Patricia Rayas-Duarte

ACKNOWLEDGEMENTS

Thanks to merciful Allah for all the countless gifts you have offered and thanks to my family and my friends for their love and support. My deepest thanks and gratitude to my mother for her extraordinary support, prayers, and unconditional love. Also, my appreciation is extended to my wife Fatimah for her support.

It is a great pleasure to acknowledge my deepest thanks to my adviser Prof. Allen Apblett. I am thankful for Professor Apblett, a faculty member at Oklahoma State University, for his encouragement, creative, and comprehensive advice until this research work came to existence. It is a great honor to work under his supervision. This thesis would not have been possible without the help and support of advisor Prof. Apblett. Also, I would like to thank Dr. Spencer P. Pitre, Dr. Elijah Schnitzler and Dr. Patricia Rayas-Duarte for their guidance, advice and help.

I would also like to express my extreme sincere gratitude and appreciation to King Saud University for sponsoring and supporting.

Name: KHALID ABDULLAH ALRASHIDI

Date of Degree: MAY, 2022

Title of Study: DEVELOPMENT OF METAL OXIDE/METAL CARBOXYLATE CHEMISTRY FOR THE SYNTHESIS OF METAL TUNGSTATES, MOLYBDATES, AND FERRITES AND EXTRACTION OF IRON FROM ORES

Major Field: CHEMISTRY

Abstract: The research reported in this dissertation explored the application of the reactions between metal oxides and metal carboxylates for the synthesis of useful ternary metal oxides containing either molybdenum or tungsten, a green extraction process for iron ores, and the production of single-source precursors for ferrites. The reaction of lanthanum acetate with molybdenum trioxide and tungstic acid and tungsten trioxide (i.e. the MO_x/acetate process) was found to produce lanthanum acetate molybdate $Ln(O_2CCH_3)(MoO_4)\bullet 1.05H_2O$ lanthanum acetate tungstate $Ln(O_2CCH_3)(WO_4)\bullet 0.95H_2O$, respectively. These compounds served as single-source precursors for β-$Ln_2Mo_2O_9$ and α-$Ln_2W_2O_9$ at relatively low temperatures. Notably, it was possible to isolate the ionic-conductor, β-$Ln_2Mo_2O_9$, as a metastable phase at room temperature. Reaction of WO_3 with aqueous lanthanum acetate was incomplete and produced a green solid due to reduction of W(VI) indicating that the MO_x/acetate process works best for layered compounds where intercalation of the reactants is possible. Thus, by the use of layered tungstic acid, H_2WO_4, the MO_x/acetate process was expanded to the preparation metal tungstates, a broad class of useful materials. One limitation of the MO_x/acetate process has been the hydrolytic instability of several metal acetates such as aluminum and ferric acetates. Therefore, the reaction of iron(III) nitrate with MoO_3 in acetate buffer was explored that unexpectedly led to the first isolation of a trimetallic oxide via the MO_x/acetate process. The reaction of iron nitrate with two molar equivalents of molybdenum trioxide produced a crystalline compound with the formula $NaFe_2(MoO_4)_2\bullet 2H_2O$ that converted into the $NaFe_2Mo_2O_9$ (a promising battery anode material) upon dehydration at 670˚C. Changing the ratio of iron nitrate to molybdenum trioxide led to isolation of amorphous solids possibly related to ferrimolybdite and ferrihydrite that upon calcining produced $Fe_2(MoO_4)_3/Fe_2O_3$ composites that are useful partial oxidation catalysts. Lastly, a green process of extraction of iron from both pure iron oxide (Fe_2O_3) and iron ore were investigated using ethylenediaminetetraacetic acid (H_4EDTA). Unlike other extraction processes for iron, the acid can readily be recovered and reused leading to marked reduction in waste. Besides silica dross, the by-product of the process is potassium sulfate that can be used in fertilizer manufacture. Recovery of ethylenediaminetetraacetic acid was 94% while iron was isolated as pure iron oxide with greater than 98% efficiency. The extraction reaction produces Fe(HEDTA) that catalyzes the extraction of iron due to its high acidity. Furthermore, neutralization of Fe(HEDTA) can be used to produced chelated iron that is used in fertilizers to make lawns greener and to prevent chlorosis in plants. Also, two equivalents of Fe(HEDTA react with nickel(II) hydroxide to produce a stoichiometric precursor for nickel ferrite, $NiFe_2O_4$. This opens the path to the synthesis of a large range of commercially-important ferrites.

TABLE OF CONTENTS

Chapter Page

LIST OF TABLES

Table Page

LIST OF FIGURES

Figure Page

CHAPTER I

INTRODUCTION

Introduction

The research presented in this dissertation explored the application of the reactions between metal oxides and metal carboxylates to the synthesis of useful ternary metal oxides containing either molybdenum or tungsten and for the extraction of iron from ores. The work included an investigation of the reaction of lanthanum acetate with tungstic acid and tungsten trioxide (the acetate method), the development of a method for preparing iron molybdate via the acetate method despite iron acetate being hydrolytically unstable, the self-catalytic extraction of iron from ore using ethylenediaminetetraacetic acid, and the use of the resulting iron chelate for synthesis of nickel ferrite with precisely-controlled stoichiometry. This introduction to the research will provide background concerning the tungsten and molybdenum-containing starting materials and the early discoveries of the Apblett research group that formed the basis of the research reported herein.Molybdenum belongs to Periodic Group VI and is found in the 4d-block between Nb and Tc. It is a very refractory metal having a melting point of 2610 ℃. As a result, molybdenum can be employed in high-temperature applications as a high-strength material. Molybdenum is electrically conductive; therefore, it can be employed in a variety of applications. At 350°C, molybdenum oxidizes slowly in air, but at 650°C and higher, it oxidizes quickly. Molybdenum compounds are used in such technological areas as catalysis, lubrications, refractories, paints, and allied industries. For instance, liquid and MoS_2 can be utilized to prepare lubricants in both forms[18]. Over the past decade, molybdenum has expanded into other markets that employ the extraordinary characterizations of this many-faceted element[18-27]. The oxides of molybdenum and tungsten have useful chemical and physical properties that remain a treasure trove for developing new materials for meeting the demands of our society. They are used in a numerous applications, including catalysis, sensing devices,[28-36] electrodes,[37-58] lithium ion batteries,[59-80] and electrochromic or liquid crystal displays.[81-88]

Molybdenum trioxide plays an important role as a reagent in the research reported herein. MoO_3 is produced industrially by roasting its main ore, molybdenum disulfide, in air atmosphere within a multiple-hearth furnace at temperatures between 600 and 700 ºC. Low temperatures must be utilized because molybdenum trioxide has an unusually low melting point of 802˚C. This produces technical purity MoO_3 that is mainly used as an additive in steel and corrosion-resistant alloys. On the other hand, molybdenum trioxide purified by sublimation is used to manufacture molybdenum metal. When absolutely pure and stochiometric MoO_3 is white but is usually has variable color due to slight reduction or hydration leading to powder or granules that are slightly yellow to slightly bluish, respectively. A combination of small amounts of reduction and hydration lead to a pale green hue. MoO_3 is very useful for the synthesis of important binary and ternary metal oxides.[89] In most materials, molybdenum oxide has either tetrahedral or octahedral coordination. However, in the structure of α-MoO_3 (Figure 1.1), the MoO_6 octahedron is highly distorted. As a result, the molybdenum environment can be described as a square pyramid within the layer of the structure (Mo-O bond lengths of 1.67, 1.73, 2*1.95, and 2.25 A˚) with a sixth long bond (2.33A˚) from a corner-shared equatorial oxygen between two MoO_6 octahedra either above or below the vertex (Figure 1.2).[1]

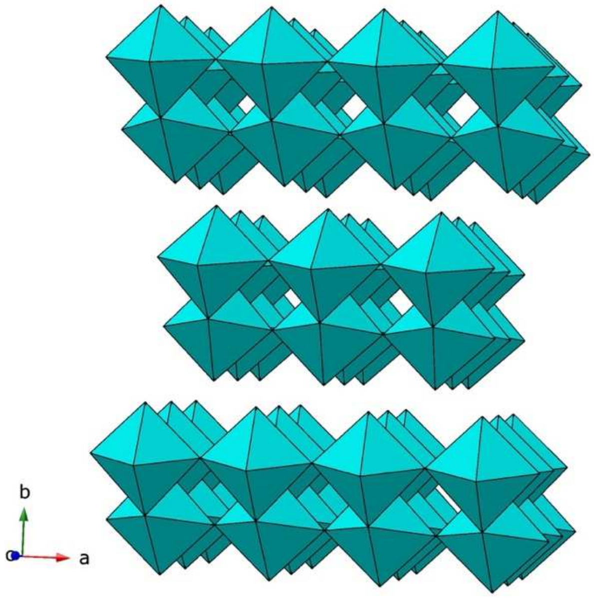

Figure 1-1 The structures of molybdenum trioxide (MoO_3). Drawn with data from Reference.[1]

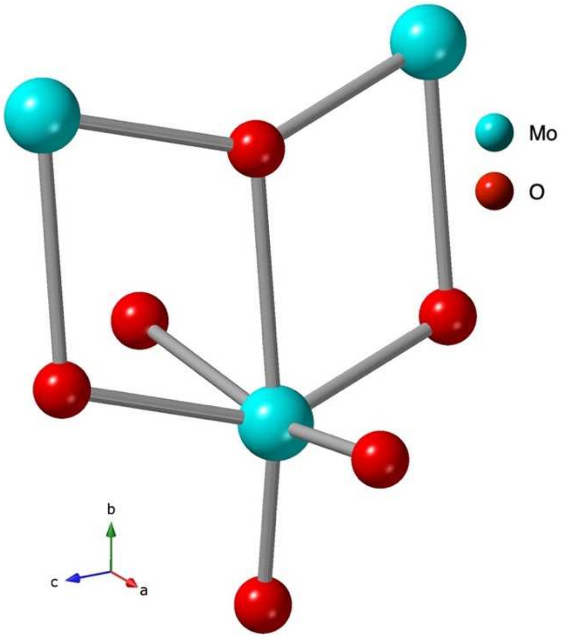

Figure 1-2 Ball and stick model of molybdenum trioxide (MoO_3) showing the bond variation around the molybdenum centers. Drawn with data from Reference [1].

Tungsten trioxide, another starting material in this investigation, has a completely different structure than that of MoO_3. Its structure is temperature dependent: it is tetragonal at temperatures above 740 °C, orthorhombic between 330 and 740 °C, monoclinic between 17 and 330 °C, triclinic from -50 to 17 °C, and becomes monoclinic again at temperatures below -50 °C.[90] These structures are related to each other through distortion and tilting of their WO_6 octahedral building blocks. The room temperature structure of WO_3, monoclinic with space group $P2_1/n$, is shown in Figure 1-3.[2] The structure is related to the cubic ReO_3 structure in which WO_6 octahedra share all six corners with six adjacent WO_6 octahedra to build a three-dimensional array. However, the symmetry of the room-temperature from is lowered from the ideal cubic ReO3 structure by tilting of the WO_6 octahedra and displacement of the tungsten ion from the center of the octahedra. The latter distortion of the octahedron leads to six quite different tungsten-oxygen bond lengths (1.825, 1.843. 1.899. 1.1919. 1.957 and 2.013 Å) as shown in Figure 1-4. The equatorial bond angles in this depiction of the WO_6 octahedra also vary widely: 81.6. 82.9. 97.2, and 97.7˚. The angle between the axial oxygen atoms is compressed from the ideal 180˚ to 163.5˚. There are strong ionic and covalent interactions in the structure leading to a wide band gap that makes WO_3 an electrical insulator[91-115]. Tungsten trioxide is insoluble in water and acids (with the exception of hydrofluoric acid), but readily dissolves in aqueous alkali hydroxide solutions or melts of alkali hydroxides or carbonates to create metal tungstates. It is the most significant, extremely pure feedstock for the manufacture of numerous tungsten compounds and tungsten metal powders. WO_3 is produced as an intermediate in the recovery of tungsten from its minerals when tungsten ores are treated with alkalis to produce aqueous tungstate solutions from WO_3 is isolated by precipitation with acid and heating. Reaction of the WO_3 thus produced with carbon or hydrogen gas reduces tungsten trioxide to the pure metal.

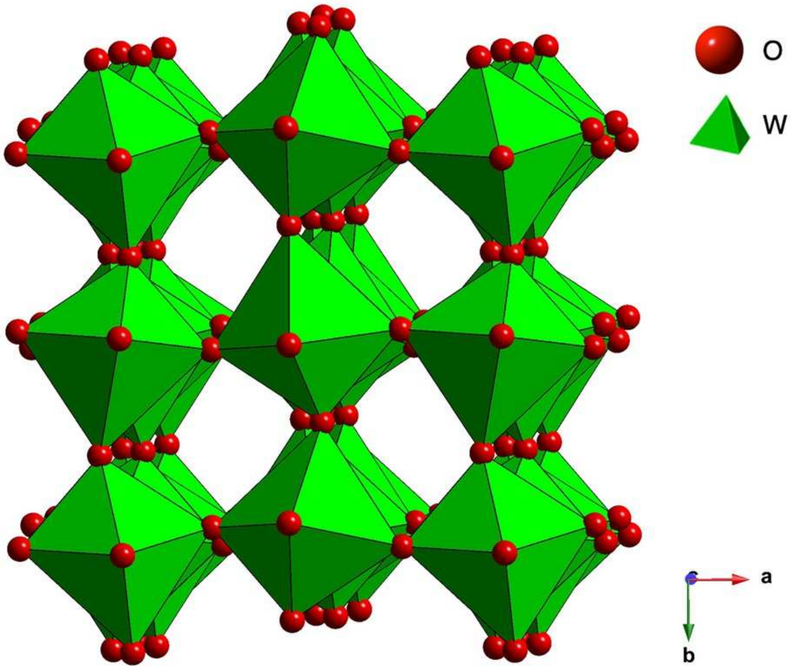

Figure 1-3 The structure of tungsten trioxide (WO_3). Drawn with data from Reference [2].

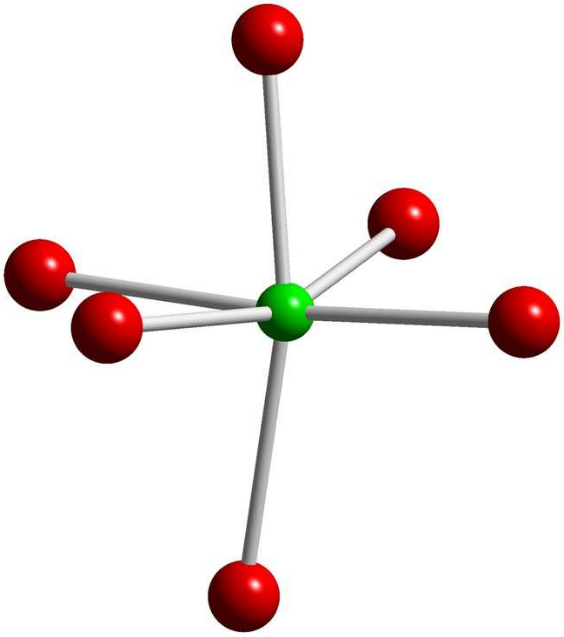

Figure 1-4 The distorted octahedron of tungsten trioxide (WO_3). Drawn with data from Reference [2].

Tungsten(VI) oxide does not exist as a mineral but occurs naturally in the form of hydrates such as meymacite WO_3•$2H_2O$ and tungstite WO_3•$2H_2O$. The tungstic acid, H_2WO_4, used in this investigation is related to tungstite. It is a layered compound that is easily prepared by acidification of a solution of an alkali metal tungstate (M_2WO_4, M= Li^+, Na^+, K^+, Rb^+, Cs^+) with hydrochloric acid. This produces a yellow solid that is actually a hydrate of tungsten trioxide (WO_3•H_2O). The crystal structure consists of layers built up from WO_6 octahedra that share four equatorial oxygens in the ac plane (Figure 1-5).[3] The water molecules occupy one of axial positions of the WO_6 octahedra so that each tungsten center has one water attached to it. The water molecules are attached so that they form rows down the c-axis with each row alternating up and down with respect to the plane in the a-axis direction. This arrangement and the offset of each layer with respect to each other allows hydrogen bonds to form between each axial oxygen ion with two water molecules attached to the WO_6 octahedra directly above or below it. In comparison to the three-dimensional structures of WO_3 (Figure 1-4) and the tungsten hydrogen bronzes, the layered structure of tungstic acid results in a significantly more open structure with more opportunity for reactions to take place[116-117]. It is this property that is taken advantage of in this investigation as the layered structure allows the intercalation of acetate and metal ions to allow formation of metal acetate tungstate compounds tungstic acid despite being a hydrate and not a true "H_2WO_4" acid like H_2SO_4, gets its name because it is fairly acidic with a pKa of 3.5. H_2WO_4 contains W^{6+} d^0 ions and would be expected to be colorless like WO_3. Its unexpected yellow color is due to a ligand to metal charge transfer from the water oxygen to the W^{6+} ion that occurs at 470 nm.[118-119] The color is very convenient for monitoring reactions since most W(VI) compounds are white solids or colorless in solution.

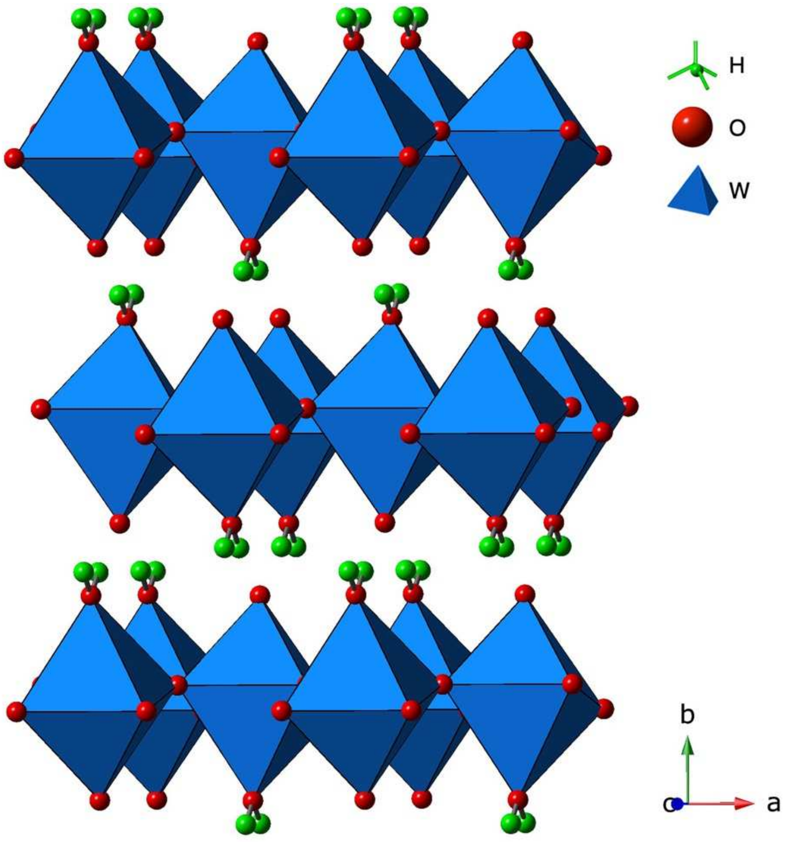

Figure 1-5 The structure of tungstic acid H_2WO_4. Drawn with data from Reference [3].

During an assessment of the utility of molybdenum trioxide for the removal of metal ions from simulated radioactive waste, the Apblett group identified an alternative for the production of lanthanum molybdenum oxide phases in aqueous media. Based on the layered structure of MoO_3, the Apblett research group chose to investigate if intercalation of metals between the sheets, followed by a reaction to generate molybdate phases, would be a useful technique for immobilization of radonuclides from nuclear waste. [120-123] In that invetigation they used a variety of lanthanide salts, uranium compounds, and thorium salts as surrogates for highly radioactive actinides such as plutonium and neptunium. The investigation eventually led to reactions of MoO_3 with metal acetates that forms the basis of this investigation.

Overall Dissertation and Scope

This dissertation is titled as "development of metal oxide/metal carboxylate chemistry for the synthesis of metal tungstates, molybdates, and ferrites and extraction of iron from ores". The first chapter (Chapter I) provides a broad outline of the dissertation and provides an overview of the research's objective and scope. Additionally, it provides a brief review of the materials of interest, their structures, and their synthesis. The main body of the dissertation is subdivided into three sections. The first section, Chapter II, discusses the synthesis of lanthanide molybdates and lanthanide tungstates via what the Apblett group now calls the MO_x Acetate process. The target of the research in the second chapter was to investigate the possibility of producing ternary oxide materials at low temperature using reaction of lanthanide acetates with molybdenum trioxide, tungstic acid, or tungsten trioxide. The precursors produced can be converted to bimetallic oxides ($Ln_2M_2O_9$, M= Mo, W) at temperatures much lower than is typically required for these compounds. Chapter III reports a successful approach to apply the MO_x Acetate process to metals, such as Fe^{3+}, that do not form hydrolytically stable acetates. Chapter IV reports a novel extraction process for iron ore that uses ethylenediaminetetraacetic acid (EDTA) as a reactant. This is a self-catalytic process as the ferric EDTA complexes formed catalyze the reaction with iron oxide. The kinetics of this process are reported along with the determination of the effect of the particle size on the extraction process. Further, the synthesis of nickel ferrite, $NiFe_2O_4$, was realized using the iron EDTA complex formed in the iron extraction Finally, Chapter V, provides a conclusion of the outcomes of the research as well as suggestions for future work.

CHAPTER II

SYNTHESIS OF LANTHANUM MOLYBDATE AND LANTHANUM TUNGSTATE VIA REACTIONS OF MOLYBDENUM(VI) OXIDE OR TUNGSTIC ACID WITH AQUEOUS ACETATE SALTS

Introduction

The discovery of the MO_x/Acetate process occurred when Chehbouni and Apblett performed a reaction of molybdenum trioxide with an aqueous solution of uranyl acetate.[107] They had previously performed a reaction with uranyl nitrate (Equation 2-1) and discovered that the reaction only proceeded to a small degree due to a rapid drop in pH to a very low value that prevented further reaction. The researchers switched to acetate salts, reasoning that a buffer would form as acetate neutralizes the protons produced in the reaction (Equations 2.2 and 2.3).

$$UO_2(NO_3)_{2(aq)} + MoO_{3(s)} + H_2O_{(l)} \longrightarrow UO_2MoO_{4(s)} + 2\ H^+_{(aq)} + 2\ NO_3{}^{1-}{}_{(aq)} \qquad \text{(Eq 2.1)}$$

$$UO_2(O_2CH_3)_{2(aq)} + MoO_{3(s)} + H_2O_{(l)} \longrightarrow UO_2MoO_{4(s)} + CH_3CO_2H_{(aq)} \qquad \text{(Eq 2.2)}$$

$$CH_3CO_2H_{(aq)} \rightleftharpoons CH_3CO_2{}^{1-}{}_{(aq)} + H^+{}_{(aq)} \qquad \text{(Eq 2.3)}$$

A reaction was performed with an excess of uranyl aceate (MoO_3 to $UO_2{}^{2+}$ molar ratio = 1:1.43) with the objective of having excess acetate in solution to prevent a large drop in pH. Over a period of one week, the MoO_3 absorbed 165% by weight of uranium pruducing a solid with a 1:1 ratio of molybdenum to uranium. The product had the characteristic yellow color of hexavalent uranium and its infrared spectrum was consistant with the formation of a hydrated compound containing uranyl ions and molybdenum oxide octahedra. This was confirmed by X-ray powder diffraction that identified the product as the mineral umohoite, $(UO_2)MoO_4(H_2O)_2$. Heating of this product to 600˚C produced phase-pure $UMoO_6$.

The reaction of metal acetates with molybdenum trioxide to form hydrated bimetallic molybdenum oxide phases was extended to a wide range of divalent transition and lanthanide metals and it was found that this is a quite general reaction.[121] Relevant to the investigation reported herein is the reaction of aqueous gadolinium acetate with molybdenum trioxide.[120] This reaction was performed with a 2:3 Gd:Mo molar ratio at reflux for seven days using 0.10 M gadolinium acetate. At the end of the reaction all of the gadolinium had been absorbed from solution to yield a white solid. The formula of this product was determined to be $Gd_2(MoO_4)_3{\cdot}2.2H_2O$ (Equation 2.4). XRD analysis showed that the product was a crystalline phase but no match to known gadolinium or molybdenum phases could be found. Upon heating to 600˚C the solid was converted to $Gd_2Mo_3O_9$. When the reaction was performed with a molar ratio of 1:1 Gd:Mo, a different compound was formed with the formula $GdMoO_4(OH){\bullet}1.5H_2O$ (Equation 2.5). The product can be described as gadolinium molybdate hydroxide, but the infrared spectrum indicates that it is not a true molybdate but contains molybdenum with a higher coordination number. A novel $Gd_2Mo_2O_9$ phase was produced upon heating to 550˚C. Notably, when, lanthanum acetate was reacted with MoO_3 under similar conditions, a lanthanum molybdate acetate, $La(MoO_4)(O_2CCH_3){\bullet}H_2O$ (Equation 2.6) was produced that served as a precursor for the oxide ion conductor, $La_2Mo_2O_9$, upon heating to 550˚C.

$$2\ Gd(O_2CCH_3)_3 + 3\ MoO_3 + 5.2H_2O \rightarrow Gd_2(MoO_4)_3{\bullet}2.2H_2O + 6\ CH_3CO_2H \qquad \text{(Eq. 2.4)}$$

$$Gd(O_2CCH_3)_3 + MoO_3 + 3.5\ H_2O \rightarrow GdMoO_4(OH){\bullet}1.5H_2O + 3\ CH_3CO_2H \qquad \text{(Eq. 2.5)}$$

$$La(O_2CCH_3)_3 + MoO_3 + 3\ H_2O \rightarrow La(MoO_4)(O_2CCH_3){\bullet}H_2O + 2\ CH_3CO_2H \qquad \text{(Eq. 2.6)}$$

Alrashidi and Apblett performed an investigation to determine what factors controlled the formation of a lanthanide molybdate hydroxide versus a lanthanide molybdate acetate.[124] It was found that formation of the acetate product only occurred in a narrow range of 1.01 Å to 1.03 Å (Figure 2-1).

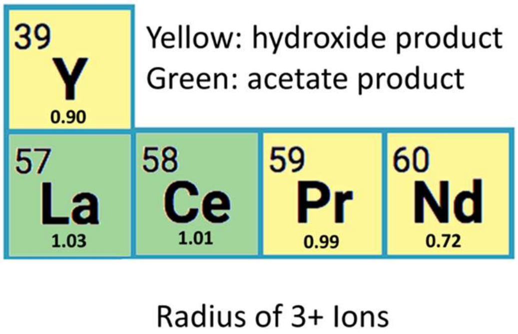

Figure 2-1. Dependence of product formed in MoO_3/lanthanide acetate reactions on the radius of the lanthanide.

This investigation reported in this chapter targeted the synthesis of an important tungstate material, $La_2W_2O_9$ by extending the MO_x/Acetate process to tungsten-containing materials. Reactions of lanthanum acetate with WO_3 and H_2WO_4 were both explored. The preparation of the molybdenum analog, $La_2Mo_2O_9$, via the MO_x/Acetate process is also discussed. In this case, MoO_3 served as the source for the reactant for lanthanum acetate.

$La_2Mo_2O_9$ has two polymorphs, a low temperature form, α-$La_2Mo_2O_9$ that transitions to β-$La_2Mo_2O_9$ above 580˚C. α-$La_2Mo_2O_9$ is particularly interesting because of its unusual structure which has an enormous unit cell that has a volume of 8796 $Å^3$ and contains 48 $La_2Mo_2O_9$ formula units![4] Figure 2-2 shows ball and stick and polyhedral models of the unit cell of α-$La_2Mo_2O_9$.

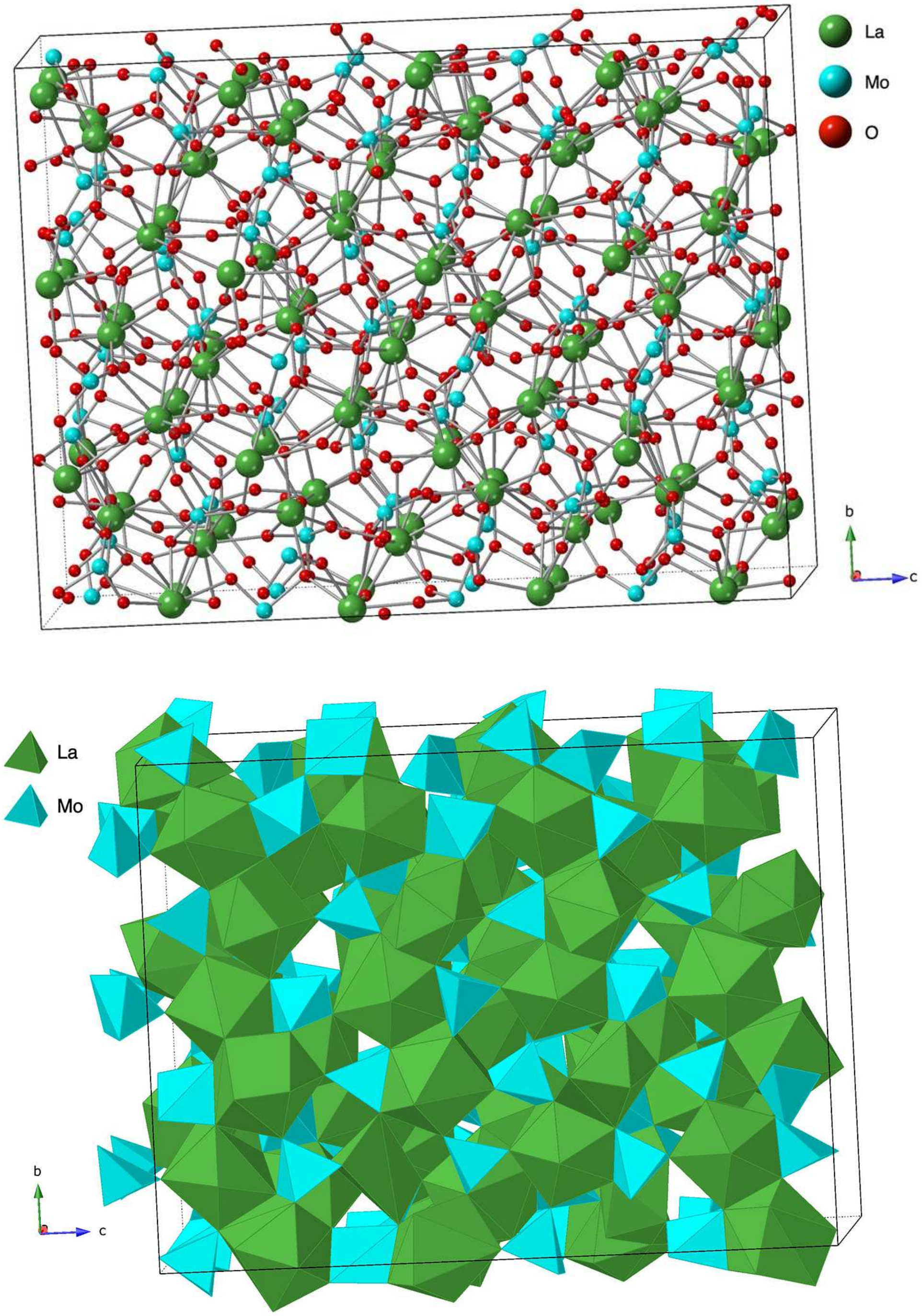

Figure 2-2 Ball and stick model (top) and polyhedral model (bottom) of the unit cell of α-$La_2Mo_2O_9$. Drawn with data from Reference [4].

The Mo atoms in α-$La_2Mo_2O_9$ are present in three different basic coordination types: there are fifteen distorted MoO_4 tetrahedra, fifteen distorted MoO_4 trigonal bipyramids, and eighteen distorted MoO_6 octahedra. These are shown in Figure 2-3 and their distribution in the unit cell is shown in Figure 2-4.

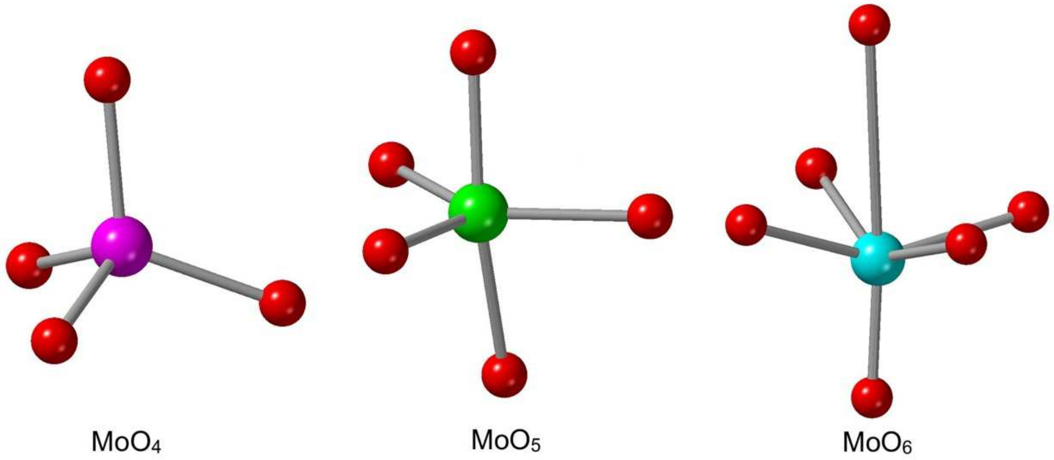

Figure 2-3. Molybdenum coordination modes in α-$La_2Mo_2O_9$. Drawn with data from Reference [4].

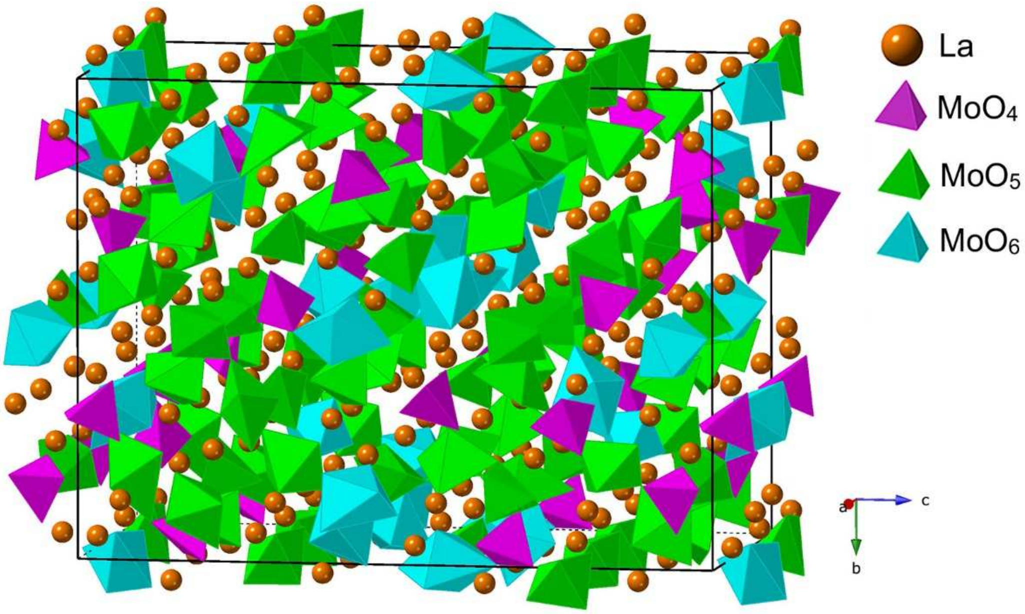

Figure 2-4. Distribution of molybdenum coordination modes in α-$La_2Mo_2O_9$. Drawn with data from Reference [4].

β-$La_2Mo_2O_9$ has significant technical value because it is a fast oxide ion conductor that exhibits an ion conductivity as high as 6×10^{-2} S/cm at 800˚C. It normally transitions to the alpha phase upon cooling below 580 ˚C but it can be stabilized to room temperature by substitution of some of the lanthanum ions with Sr, Ba, K, or Bi, $(La_{2-x}A_x)Mo_2O_9$, or by substituting some of the molybdenum ions with Re, S, W, Cr or V, $La_2(Mo_{2-x}B_x)O_9$.[125] The crystal structure β-$La_2Mo_2O_9$ is cubic and much simpler than the alpha-phase. The structure is strongly related to that of β-$SnWO_4$ shown in Figure 2-5.[5] The latter is built from isolated WO_4 tetrahedra that coordinate to tin(II) octahedra by corner-sharing. The SnO_6 is very distorted because the tin lone pair occupies one face.

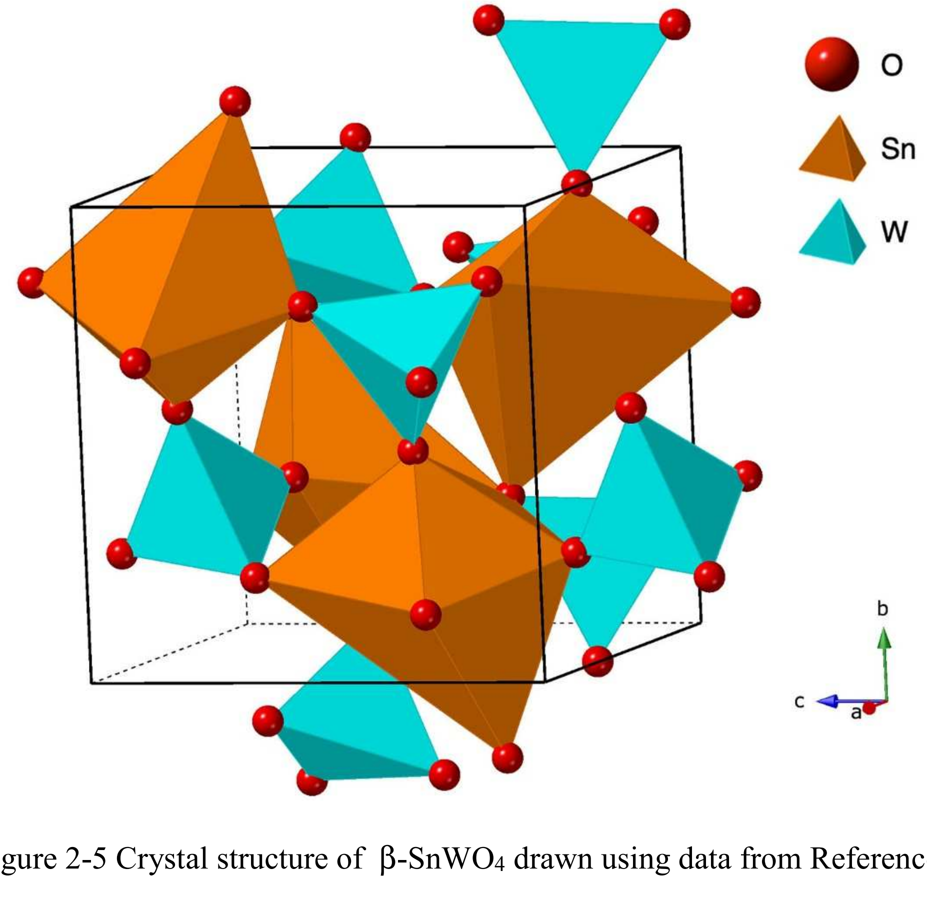

Figure 2-5 Crystal structure of β-$SnWO_4$ drawn using data from Reference [5].

In β-$La_2Mo_2O_9$, the lone pair of tin is replaced by an oxygen ion to produce a LaO_7 moiety.[6] As, shown in Figure 2-6, the solved X-ray crystal and neutron crystal structure shows a 15-coordinated lanthanum center. The lanthanum ion appears to have this highly unusual high coordination number because the oxygens are disordered such that the O2 and O3 sites are only partially occupied. Such disorder is not uncommon in oxide conductors. The O2 site is 2/3 occupied while the O3 site is 1/3 occupied. The O1 sites are not disordered. Once the disordered oxygens are accounted for, the lanthanum ions are really, on average, have a more normal, expected nine-coordination (6 O2+ 6 O3 + 3 O1 = 2/3×6 + 1/3×6 + 3 = 9). Similarly, the molybdenum centers appear to be hepta-coordinate but once the occupation of the oxygen sites is taken into account, the overall valency of the molybdenum ion corresponds, on average, to MoO_4^{2-} (3 O2 + 3 O3 + O1= 2/3×3 + 1/3×3 + 1 = 4).

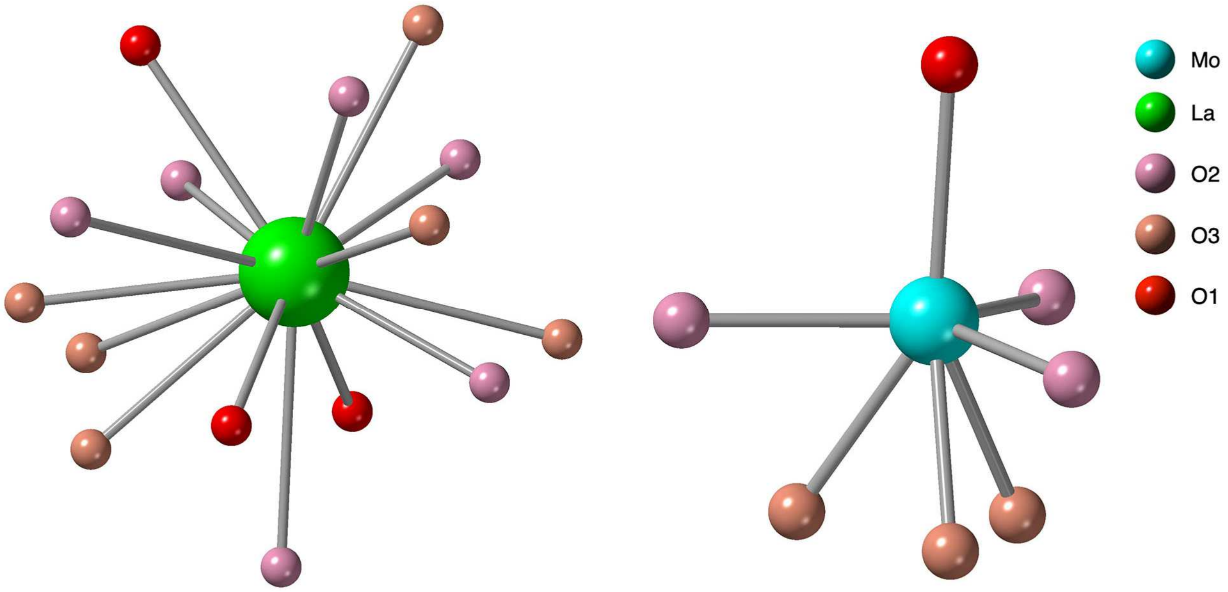

Figure 2-6 Coordination of lanthanum and molybdenum in β-$La_2Mo_2O_9$. O2 positions are 2/3 occupied and the O3 positions are 1/3 occupied. Drawn with data from Reference [6].

The overall structure of β-$La_2Mo_2O_9$ is shown in Figure 2-7. Notably, the formation of a new class of fast oxide conductors (termed LAMOX) based on a related tin (II) structure spurred the search for other oxide ion conductors based on replacing tin and its lone pair with another ion and an accompanying oxygen ion.

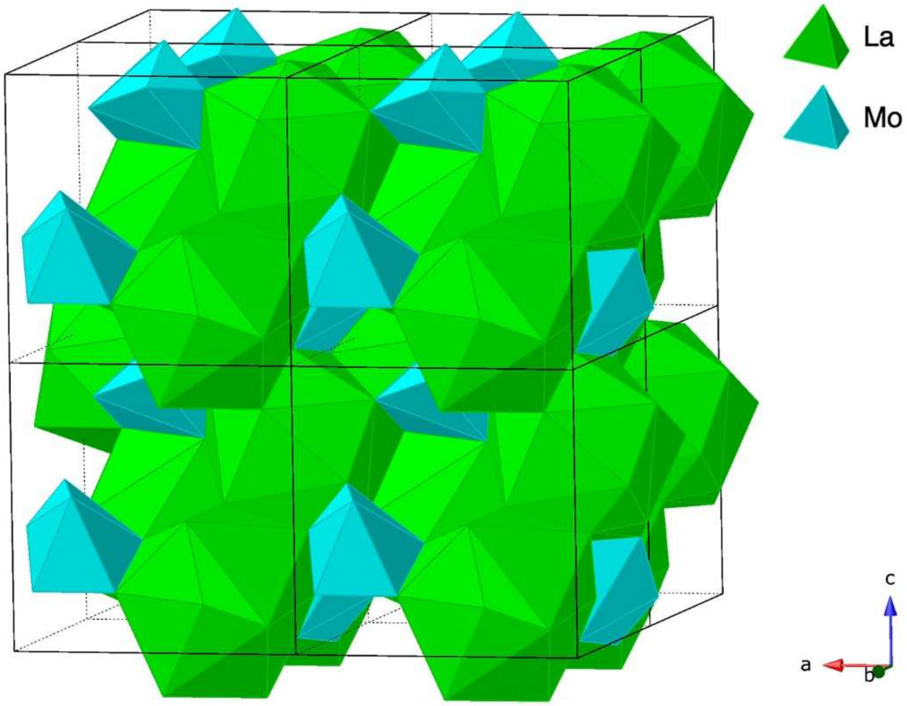

Figure 2-7 Crystal structure of β-$La_2Mo_2O_9$. Drawn with data from Reference [6].

There are a few other applications of $La_2Mo_2O_9$ beyond fast ionic conductors. For example, replacement of some La^{3+} ions with Nd^{3+} ions produces a novel monoclinic phase that is promising for applications of ultra-short pulse lasers. On the other hand, doping with Eu^{3+} produces red phosphors.[7] Further, it was found that $La_2Mo_2O_9$ displays giant electrostriction effects and surface phases that are manifestly polar that make it a promising electromechanical material system.[126]

In this investigation, the target tungsten-containing ternary metal oxide was $La_2W_2O_9$, a material that finds application as red-emitting phosphors when doped with Eu^{3+}.[127-129] Notably, the tungstate group can compensate for the low absorption coefficient of most trivalent rare earth activators through the process of host sensitization that takes advantage of tungstate's unique capability for self-activation followed by efficient energy transfer to the activator.[130-134] Eu^{3+}-doped $La_2W_2O_9$ red phosphors were used to fabricate white hybrid LEDs by combining them with a yellow organic dye and near-UV LEDs.[135] The white hybrid LED showed an excellent color rendering index (83%), with CIE color coordinates (0.313, 0.365) and a correlated color temperature of 6280 K. $La_2W_2O_9$ doped with Fe^{3+}, a highly near-infrared reflective pigment with a reflectance of 89.25% between 700 and 2500 nm.[136] The absorption of light in the visible range by Fe^{3+} leads to a peach color (CIELAB profile: L = 74.20, a = 22.69, and c = 22.42 , Figure 2-8). It was estimated that a homeowner could save $7.32 per month in air-conditioning costs by coating the walls and roofs of the building with an energy-saving paint containing $La_2W_{1.8}Fe_{0.2}O_{9-\delta}$.

Figure 2-8. Color of Fe-doped $La_2W_2O_9$.

The triclinic structure of α-$La_2W_2O_9$ is complicated and unusual in the fact that it contains isolated $[W_4O_{18}]^{12-}$ rings that are built of alternating WO_6 octahedra and WO_5 trigonal bipyramids connected to each other by corner-sharing (Figure 2-9 left).[137] The rings are arranged with their centers at the corners of the ab planes of the unit cells, forming stacks down the c-axis (Figure 2-9 right).

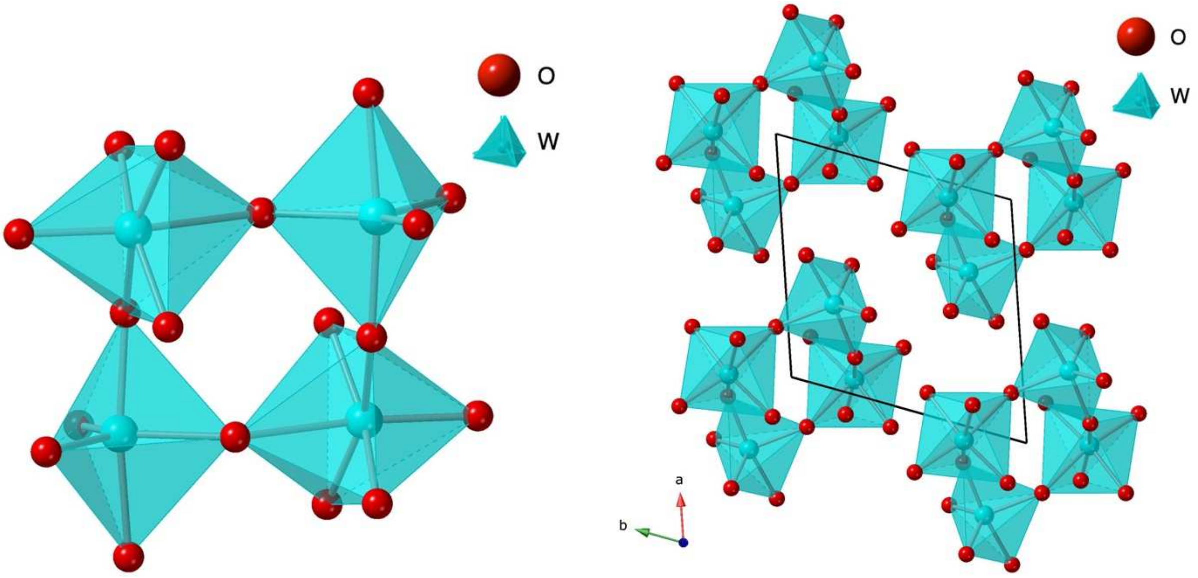

Figure 2-9. $[W_4O_{18}]^{12-}$ rings in α-$La_2W_2O_9$. Drawn with data from Reference.[7]

There are two types of lanthanum present in the structure, one (La2) that is coordinated by 12 oxygen ions and one that is coordinated by 10 oxygen ions (La1) as shown in Figure 2-6 The latter polyhedra are tricapped trigonal prisms, whereas the former look like distorted cubes with two capped adjacent faces. These polyhedra are connected one to each other by edges and corners to build up a three-dimensional network (Figure 2-11).

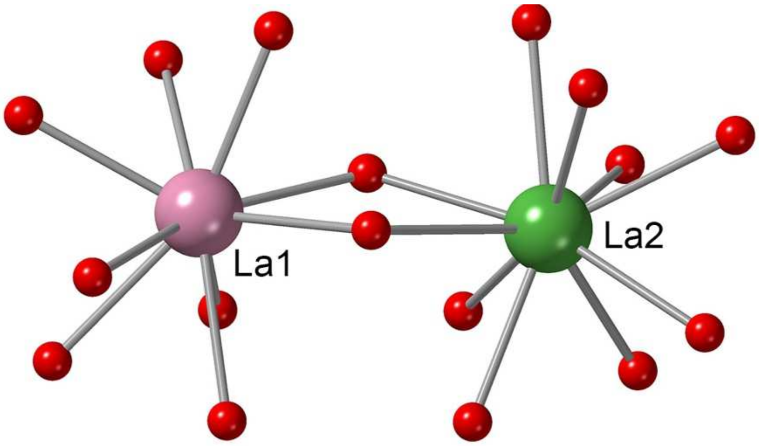

Figure 2-10. Lanthanum polyhedra in α-$La_2W_2O_9$. Drawn with data from Reference [7]

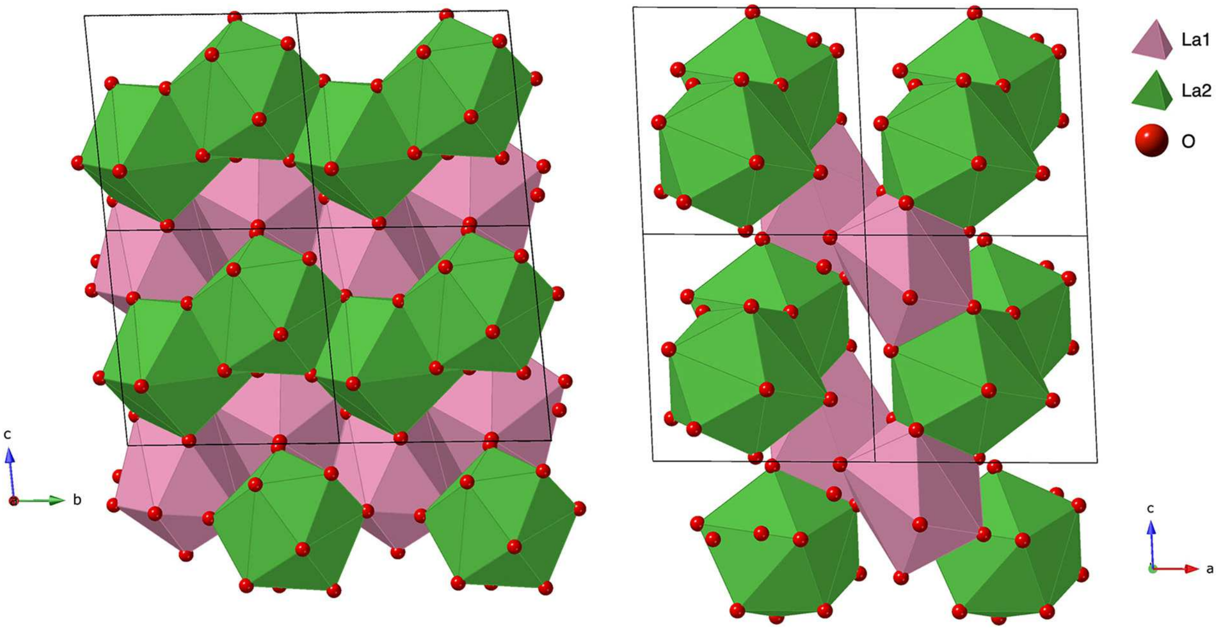

Figure 2-11. Two views of the network of lanthanum polyhedra in α-$La_2W_2O_9$. Drawn with data from Reference [7].

A comparison of the cell parameters of α-$La_2W_2O_9$ (a=7.2489 Å, b=7.2878 Å, and c=7.0435 Å, α=96.367˚, β=94.715˚, and γ=70.286˚) with those of β-$La_2Mo_2O_9$ (a=7.2014 Å, α=β=γ=90˚) shows the two structures are related. The a, b, α, and β parameters are quite close between the two structures and only the c axis is significantly different. The average of the cell lengths on α-$La_2W_2O_9$ is 7.1934. This is only 0.1% different from the lattice constant of β-$La_2Mo_2O_9$. The smaller c axis length is compensated by a decrease of the γ angle. In both structures, a cubic arrangement for the cations in the unit cell is observed for the two structures. This is shown for α-$La_2W_2O_9$ in Figure 2-12. Combining all of the elements of the structure discussed so for gives the overall structure shown in Figure 2-13 for α-$La_2W_2O_9$.

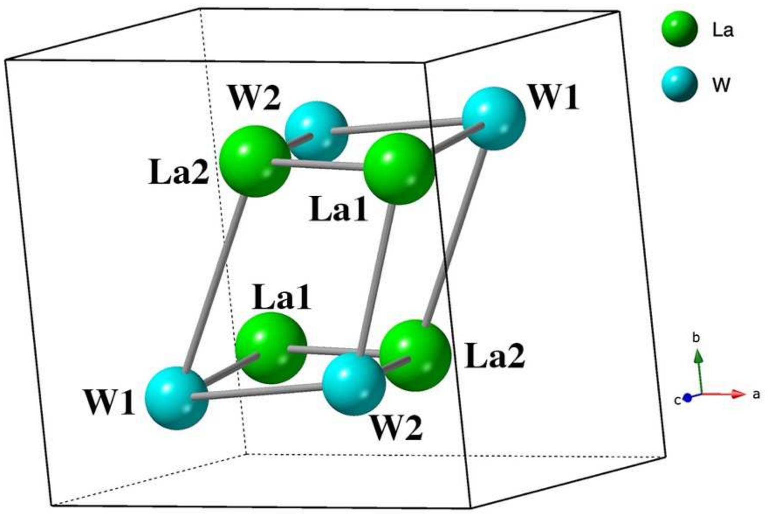

Figure 2-12 Cubic arrangement for the cations in the unit cell of α-$La_2W_2O_9$. Drawn with data from Reference [7].

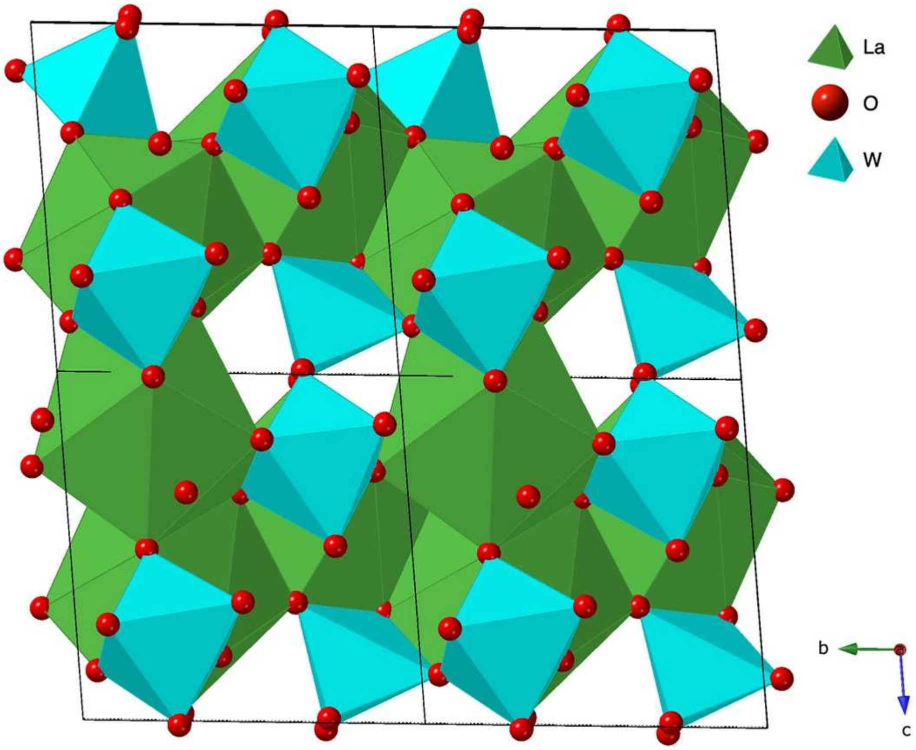

Figure 2-13 Crystal structure of α-$La_2W_2O_9$. Drawn with data from Reference [7].

Triclinic α-$La_2W_2O_9$ undergoes a phase transition at 1070˚C to form a cubic phase analogous to *β*-$La_2Mo_2O_9$ that could potentially also be an oxide ion conducting phase. Unfortunately, it has been difficult to stabilize the cubic phase at lower temperature. Ions such as Sr^{2+}, Ba^{2+}, K^{+}, Nb^{5+} and V^{5+}, have been introduced into the *α*-$La_2W_2O_9$ structure but only high levels of Ba^{2+} and V^{5+} substitutions retained the cubic form at room temperature after firing above 1100 °C and quenching rapidly.[138] Unfortunately, these phases are metastable and irreversibly transform into the triclinic *α*-phase above 700 °C, making it impossible to take advantage of fast ionic conduction that requires higher temperature.

Hybrid $La_2W_2O_9$/ $La_2M_2O_9$ materials were prepared by both the ceramic method and microwave synthesis.[8] It was found that for $La_2W_{2-x}Mo_xO_9$, when x= 0.3 to 0.7, the *β*-phase can be isolated at room temperature by quenching rapidly. Interestingly, if these materials are slowly cooled, mixtures of α and β phases are obtained in which the β phase is enriched in molybdenum while the α-phase is correspondingly deficient in that element. When x is 0.1 or 0.2, only mixed α and β phases are produced by quenching the β phase rapidly. The room temperature stability of β-$La_2W_{1.7}Mo_{0.3}O_9$ made it possible to determine its structure (Figure 2-14) via the Rietveld method analysis of its X-ray powder diffraction pattern.[8] The structure of this compound and, presumably, β-$La_2W_2O_9$ is isostructural with β-$La_2Mo_2O_9$.

Overall, $La_2W_2O_9$ and $La_2Mo_2O_9$ materials have interesting structural chemistry and compelling applications that make them excellent targets for preparation via the MO_x/Acetate process. The results of an investigation of the reaction of aqueous lanthanum acetate and MoO_3, WO_3, and H_2WO_4 is presented herein.

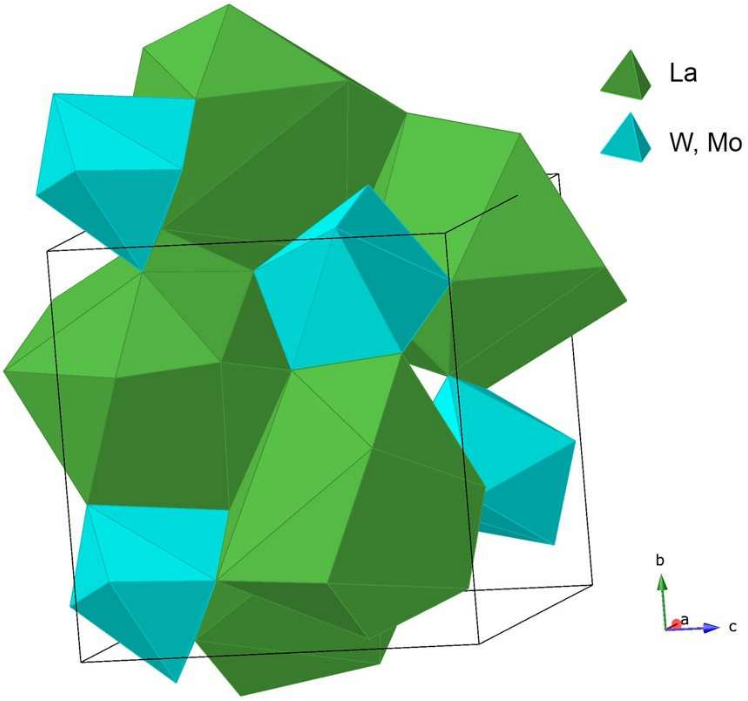

Figure 2-14 Crystal structure of α-$La_2W_2O_9$. Drawn with data from Reference [8].

Experimental

Materials and Methods

Commercially available reagents of ACS grade purity or better were used without further purification. Water was purified by reverse osmosis followed by deionization. Metal concentrations were determined by microwave plasma–atomic emission spectrometry using an Agilent 4200 microwave plasma atomic emission spectrometry (MP-AES) instrument and NIST-traceable standards. Thermogravimetric analysis (TGA) was performed using a Mettler TGA instrument. Thermal decomposition experiments were performed in an alumina crucible under an air atmosphere with a ramp rate of 5 °C min^{-1}. Infrared spectra were recorded on a Nicolet iS50 FT-IR spectrometer in the range of 4000–500 cm^{-1} and Raman spectra were recorded on a Nicolet 9610 Raman Spectrometer in the range of from 500–10 cm^{-1} with 4 cm^{-1} resolution. X-ray powder diffraction (XRD) patterns were obtained using a Bruker AXS D-8 Advance X-ray powder diffractometer with Cu Kα radiation. Crystalline phases were identified using a search/match program and the PDF-2 database of the International Center for Diffraction Data. The crystallite size of calcined products was evaluated using the Scherrer equation. Scanning electron microscopy (SEM), performed with a FEI Quanta 600 field emission gun environmental scanning electron microscope, was used to determine the particle sizes and morphologies of products. Surface areas were determined by nitrogen physisorption using the Brunauer–Emmett–Teller (BET) method on a Quanta Chrome Nova 1200 instrument. The pH changes over time were measured using an ISFET pH meter (model IQ125) obtained from IQ Scientific, USA.

Reaction of molybdenum trioxide (MoO_3) with lanthanum acetate

$La(CH_3CO_2)_3 \cdot 1.5\ H_2O$ (7.138 g, 20 mmol) was dissolved in 100 ml of distilled water in a round bottom flask. Next, molybdenum trioxide (MoO_3) (1.446 g, 10 mmol) was added to the solution of lanthanum acetate. The pH was determined to be 7 at the beginning of the reaction. The mixture was heated to reflux for nine days. After that, the reaction mixture was cooled to room temperature and the solid product was isolated by filtration, washed extensively with water, and dried in vacuum at room temperature for two days. This produced $La(O_2CCH_3)(MoO_4) \cdot 1.05H_2O$ as a white solid in a yield of 3.757 g (99.94 %). The pH of the filtrate was determined to be 4.3.

Reaction of tungstic acid (H_2WO_4) with lanthanum acetate

$La(CH_3CO_2)_3 \cdot 1.5\ H_2O$ (6.840 g, 20 mmol) was dissolved in 100 ml of distilled water in a round bottom flask. Next, tungstic acid (H_2WO_4) (1.446 g, 10 mmol) was added to the solution of lanthanum acetate and the mixture was heated to reflux for four days. During that time, the pH changed from 6.3 to 4.4 and the yellow color of the tungstic acid solid faded to white. The solid product was isolated by filtration, washed extensively with water, and dried in vacuum at room temperature for two days. The white solid, later identified as $La(O_2CCH_3)(WO_4)•0.95H_2O$, was isolated in a yield of 4.80 g.

Reaction of tungsten trioxide (WO_3) with lanthanum acetate

$La(CH_3COO)_3•1.5\ H_2O$ (6.828 g, 20 mmol) was dissolved in 100 ml of distilled water in a round flask. Tungsten trioxide (WO_3) was subsequently added to the result solution. The mixture was then heated to reflux for two days. The pH at the beginning of the reaction was found to be 6.8 while at the end it was 5.53. The green product was isolated by filtration, washed with water, and then dried in a vacuum for 48 hours. The yield of the green solid was 3.193 g.

Results and Discussion

The reactions of aqueous lanthanum acetate with both molybdenum trioxide and tungstic acid produced white solids whose yields were close to what was expected for formation of $La(O_2CCH_3)(MO_4)$ where M=Mo or W. The pH of the reaction mixtures fell from near neutral to 4.3 and 4.4, respectively. In these reactions, lanthanum acetate was used in a 2-fold excess so that sufficient acetate would be present to buffer the reaction mixture. When 20 mmol of $La(O_2CCH_3)_3$ reacts with 10 mmol of tungstic acid or MoO_3, 20 mmol of protons are produced that react with acetate to form 20 mmol of acetic acid. 10 mmol of the original 40 mmol of acetate remain in the $La(O_2CCH_3)(MO_4)$ products, leaving 40-20-10=10 mmol of acetate in solution. Therefore, at the end of the reaction in 100 ml of water, the solution should contain 0.1 M acetate and 0.2 M acetic acid. The later has a pKa of 4.75, so the final pH should be 4.4 which is what is observed. In the case of WO_3 the final pH was high (5.53) and the yield of solid was low indicating an incomplete reaction. Furthermore, the solid was green in color suggesting that reduction of W(VI) had taken place. These results certainly suggest that the use of layered compounds such as molybdenum trioxide and tungstic acid certainly facilitates the reaction with lanthanum acetate possibly by allowing the ions to intercalate between the layers leading to complete reactions.

Infrared spectroscopy is an ideal method to identify the presence of acetate in a solid since acetate has two distinctive strong infrared absorptions that correspond to the symmetric and asymmetric stretching vibration of the carboxylate C-O bonds. The infrared spectra of the reaction products and the $La(CH_3COO)_3$•1.5 H_2O starting material are shown in Figures 2.15 to 2.18. All of the products have peaks in the range of 1600 to 1350 cm^{-1} indicating that they do contain acetate.

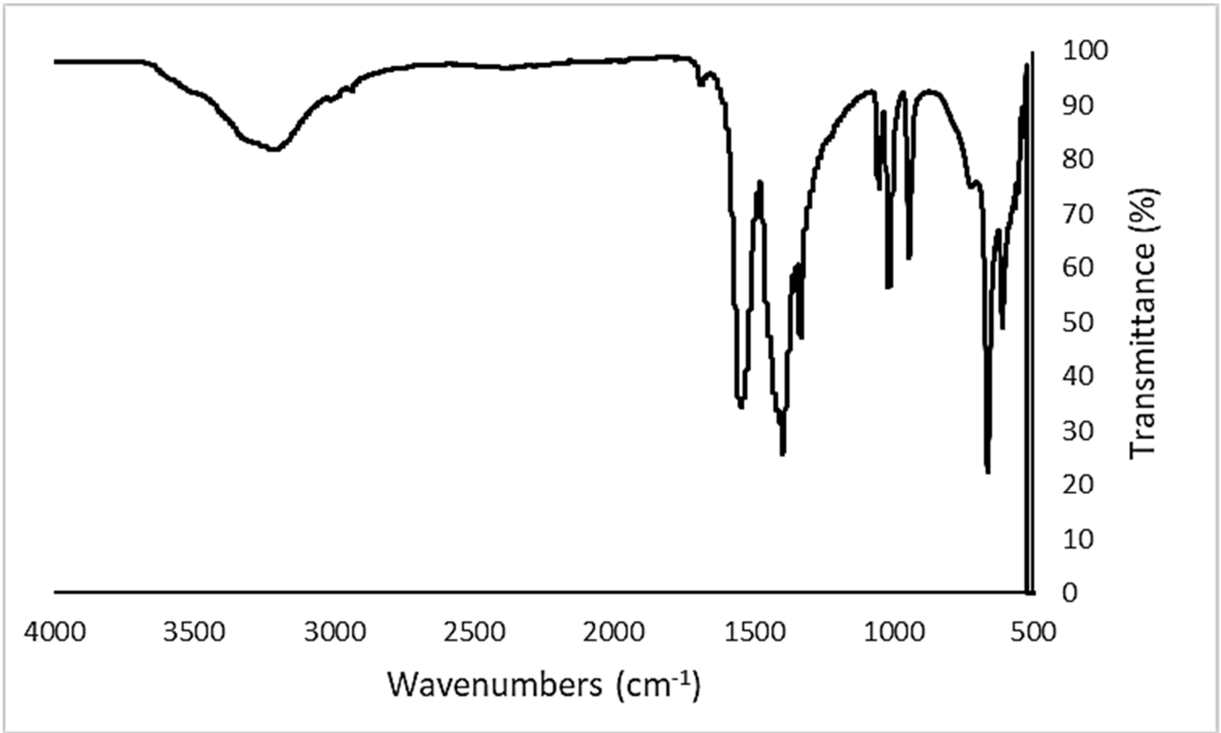

Figure 2-15. Infrared Spectrum of $La(O_2CCH_3)_3$•1.5H_2O

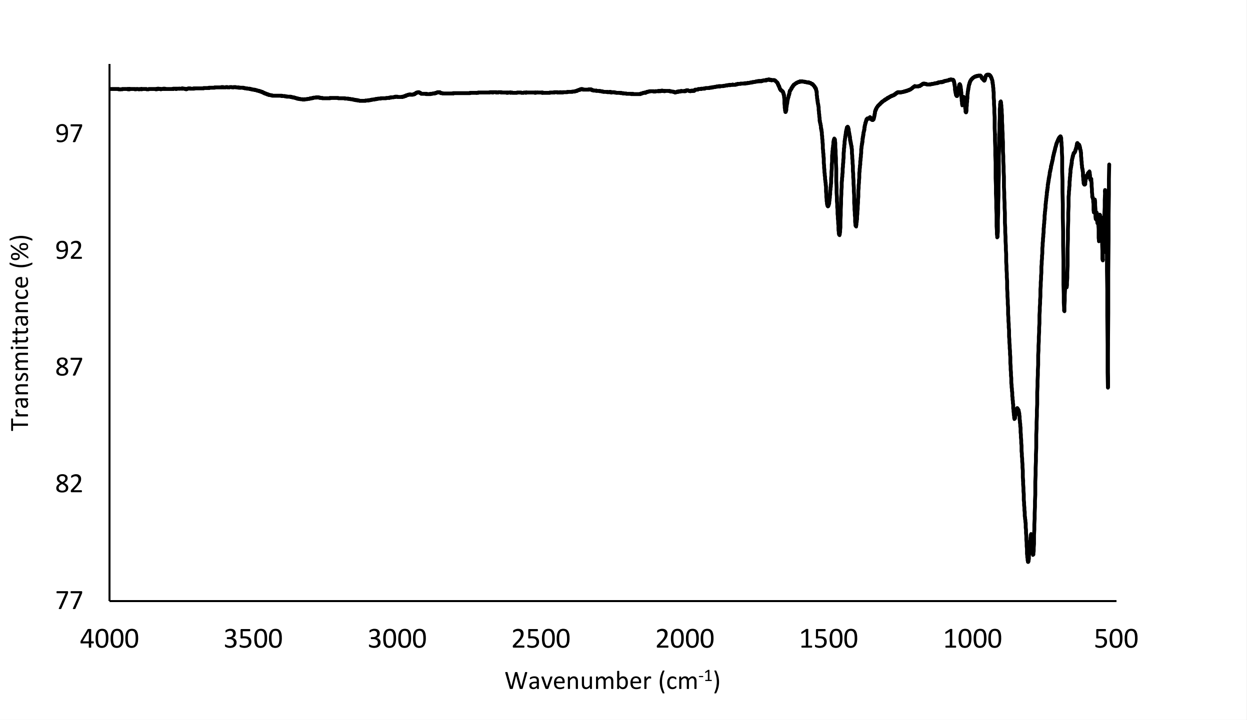

Figure 2-16. Infrared spectrum for the product from reaction of lanthanum acetate with MoO_3.

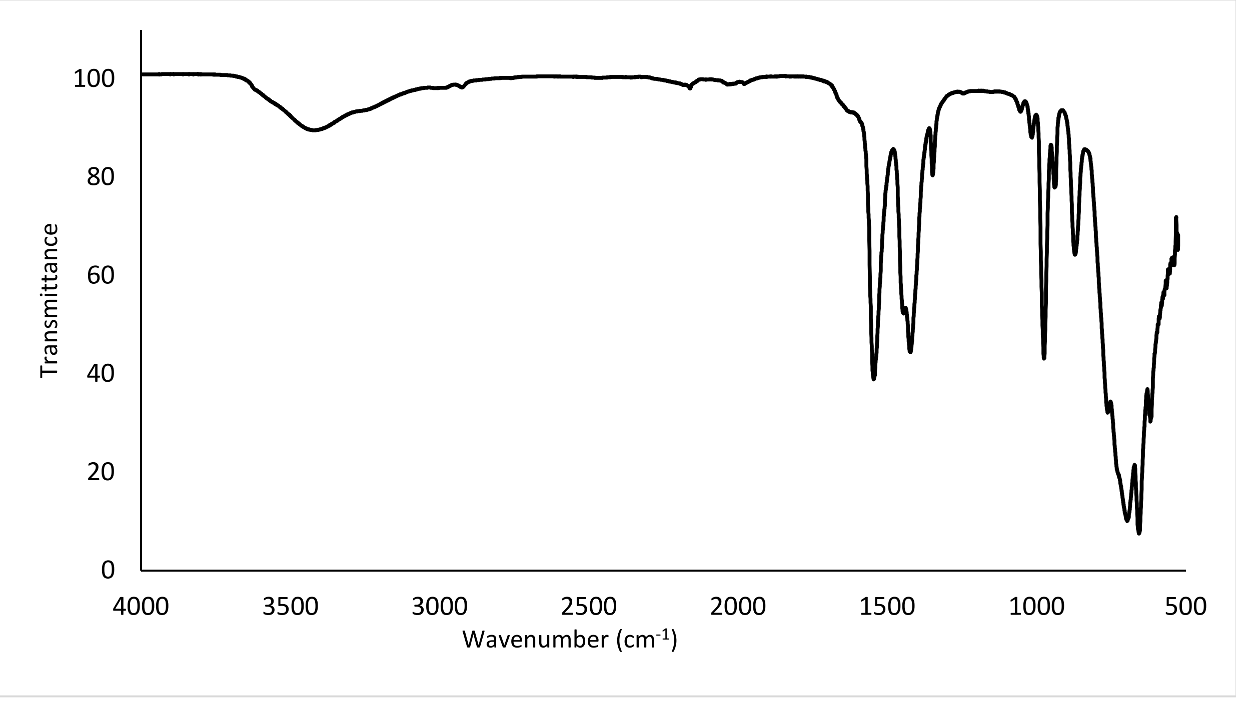

Figure 2-17. Infrared spectrum for the product from reaction of lanthanum acetate with H_2WO_4.

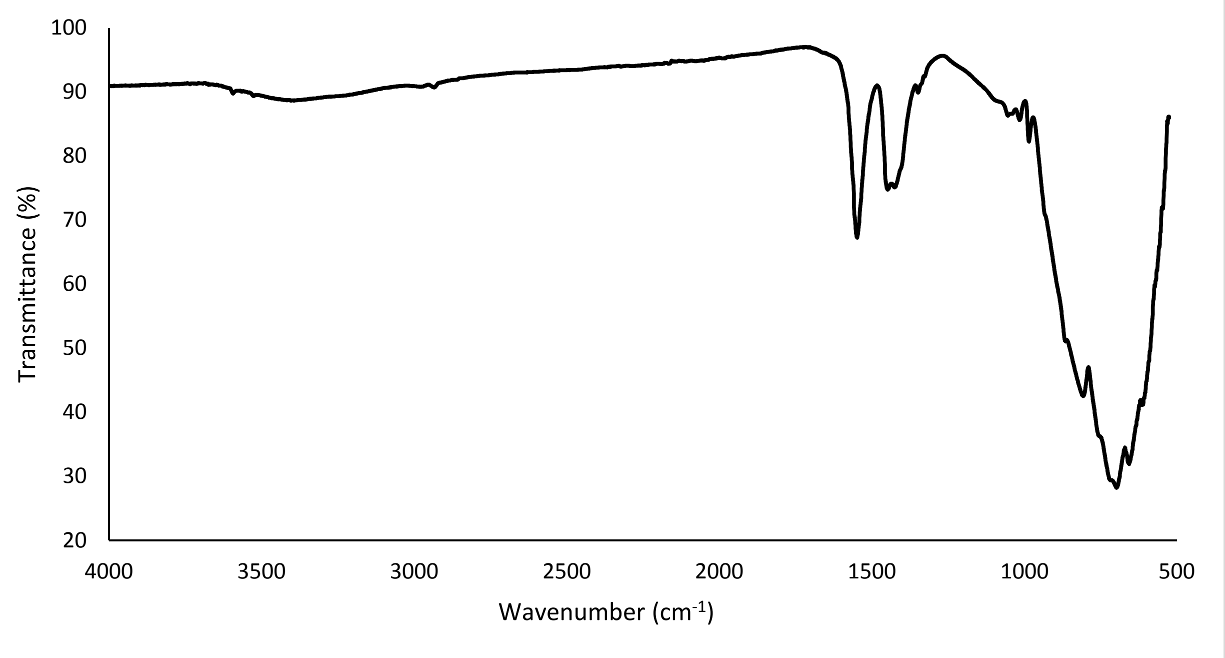

Figure 2-18. Infrared spectrum for the product from reaction of lanthanum acetate with WO_3.

The mode of binding of acetate can often be determined from the separation (Δ) between the symmetric (ν_s) and asymmetric (ν_{as}) COO stretches.[139] The four possible coordination modes, monodentate (I), chelating (II), bridging (III) and polymeric (IV) are shown in Figure 2-19. Monodentate acetates (Type I) typically have a large Δ greater than 200 cm^{-1} while chelating acetate groups (Type II) tend to have Δ below 105 cm^{-1}. The bridging and polymeric modes typically have Δ between these two extremes.

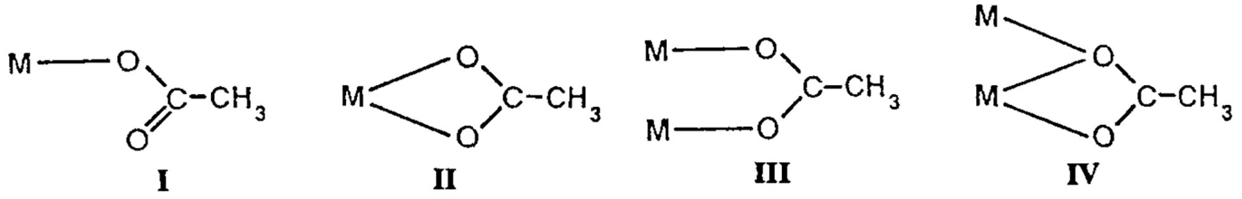

Figure 2-19. Coordination modes for acetate

Since the positions and spacings between the carboxylate modes are somewhat dependent on the metal, infrared spectra of acetate-containing lanthanum complexes were accessed in the literature where both the crystal structure and the peak positions for the carboxylates were reported.

Unfortunately, a suitable report for a unidentate complex was not found but this was not necessary for determining the likely arrangement of the compounds produced in this study. The reference compounds indicated that chelating acetates would have Δ less than or equal to 92 cm^{-1} while bridging or polymeric acetates would have Δ above 110 cm^{-1}. The product from reaction of lanthanum acetate with molybdenum trioxide has three peaks in the infrared spectrum that are due to two acetate groups with overlapping symmetric stretches. The presence of two different acetate environments was confirmed by solid-state carbon-13 NMR spectroscopy where two sets of acetate peaks were observed (Figure 2-20). These peaks had Δ of 58 cm^{-1} and 95 cm^{-1}, clearly indicating that the acetates were chelating. On the other hand, the product from the reaction of lanthanum acetate with tungstic acid had Δ= 124 cm^{-1} suggesting the presence of bridging acetate groups. Thus, it may be concluded both the products from molybdenum trioxide and tungstic acid contain acetate groups but the acetate coordination modes, and therefore the structure of the compounds are different from each other. The green product from the reaction of tungsten trioxide with lanthanum acetate did have infrared peaks due to acetate but these were weak in comparison to the product from the reaction of tungstic acid. Notably, the peak positions were the same for the two compounds. This, and the fact that the tungsten trioxide product also a broad peak at 695 cm^{-1} attributable to unreacted tungsten trioxide, suggests that this reaction failed to go to completion. The end result was likely a core of tungsten trioxide (or WO_{3-x} giving rise to the green color) surrounded by an outer shell of insoluble lanthanum acetate tungstate product. It is possible that use of nanoparticulate tungsten trioxide can allow complete reaction with lanthanum acetate to occur, but it is much more convenient to use tungstic acid as its layered structure facilitates complete reaction.

Table 2-1. Carboxylate stretching vibration positions for lanthanum acetate complexes.

Compound	Acetate Arrangement	ν_{as} (cm^{-1})	ν_s (cm^{-1})	Δ (cm^{-1})	Reference
$EuL^1Ac_2 \bullet 5H_2O$*	Chelating	1437	1355	82	[140]
$LaAc_3 \bullet 1.5H_2O$	Polymeric	1560	1420	149	[141]
$LaAc_3 \bullet H_2O$	Polymeric	1590	1425	165	[142]
$LaAc_3 \bullet H_2O$	Bridging	1560	1450	110	[142]
$LaAcL^2(NCS)_2$**	Chelating	1520	1428	92	[143]
$LaAcMoO_4 \bullet 1.05H_2O$	Unknown	1498	1403	95	This work
$LaAcMoO_4 \bullet 1.05H_2O$	Unknown	1461	1403	58	This work
$LaAcWO_4 \bullet 1.05H_2O$	Unknown	1544	1420	124	This work

* L^1= 2,9-diformylphenanthrolinebis(benzoyl)hydrazone
** L=$C_{25}H_{28}N_6$ Schiff base from 1,2-diaminobenzene and 2,6-pyridinecarboxaldehyde

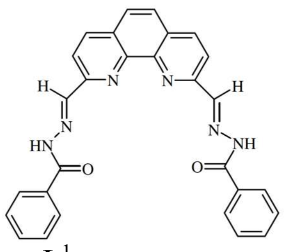

L^1

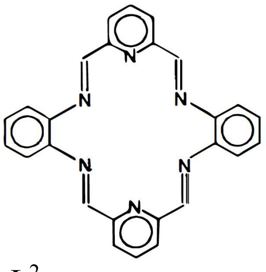

L^2

The infrared spectra also provide information on the molybdenum or tungstate species present in the products. The product from reaction of lanthanum acetate with MoO_3 has strong peaks at 884, 835, and 805 cm^{-1} that can be attributed to the asymetric Mo-O stretching mode of molybdate (MoO_4^{2-}) anions. For comparison, the corresponding vibrations are at 880 and 839 cm^{-1} in $La_2(MoO_4)_3$ and 813 cm^{-1} in $CaMoO_4$.[144-145] The tungstic acid/lanthanum acetate product has infrared absorptions attributable to W-O stretching modes of tungstate (WO_4^{2-}) anions at 974, 870, 745, and 660 cm^{-1}. The corresponding peaks are found at 938, 836, 735, and 681 cm^{-1} in $La_2(WO_4)_3$.[146]

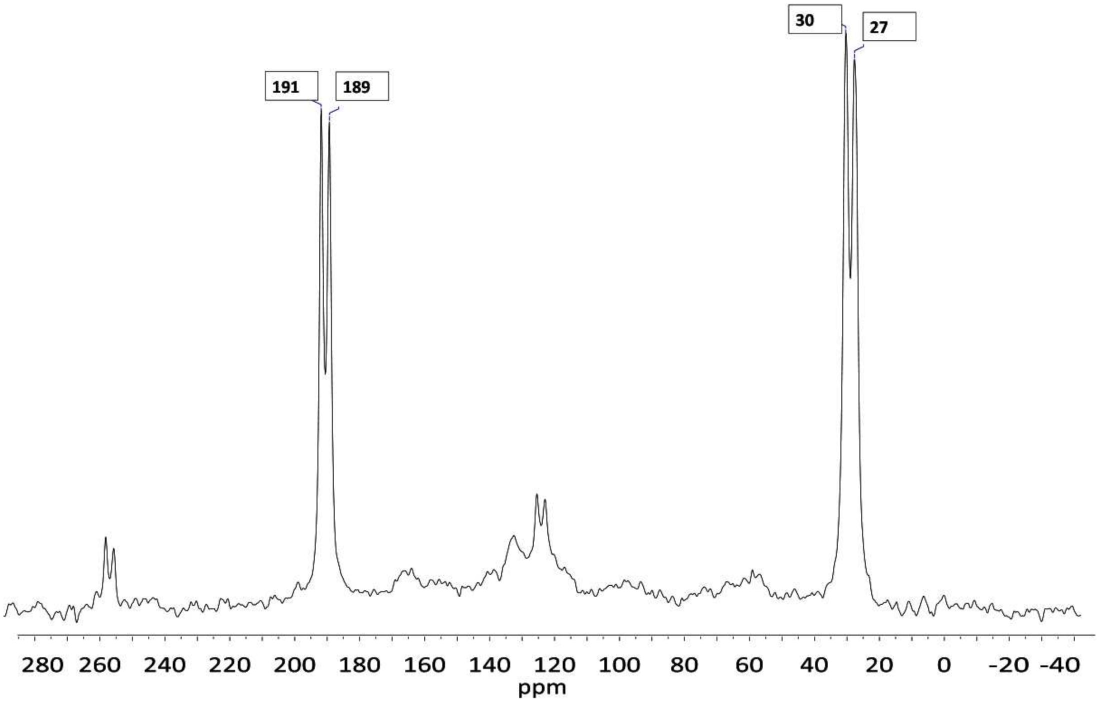

Figure 2-20. Carbon-13 Solid state NMR spectrum of product from reaction of lanthanum acetate with MoO_3.

Having established that the materials produced from the reaction of lanthanum acetate with molybdenum trioxide contains acetate and molybdate groups and that from the reaction of lanthanum acetate with tungstic acid contains acetate and tungstate groups it remained to determine the ratio of the anions and the water content. Thermal gravimetric analysis was used to gather this data and to identify the temperature required for conversion of the compounds to ceramic materials. The thermal gravimetric traces for the products are provided in Figures 2-21 to 2-23.

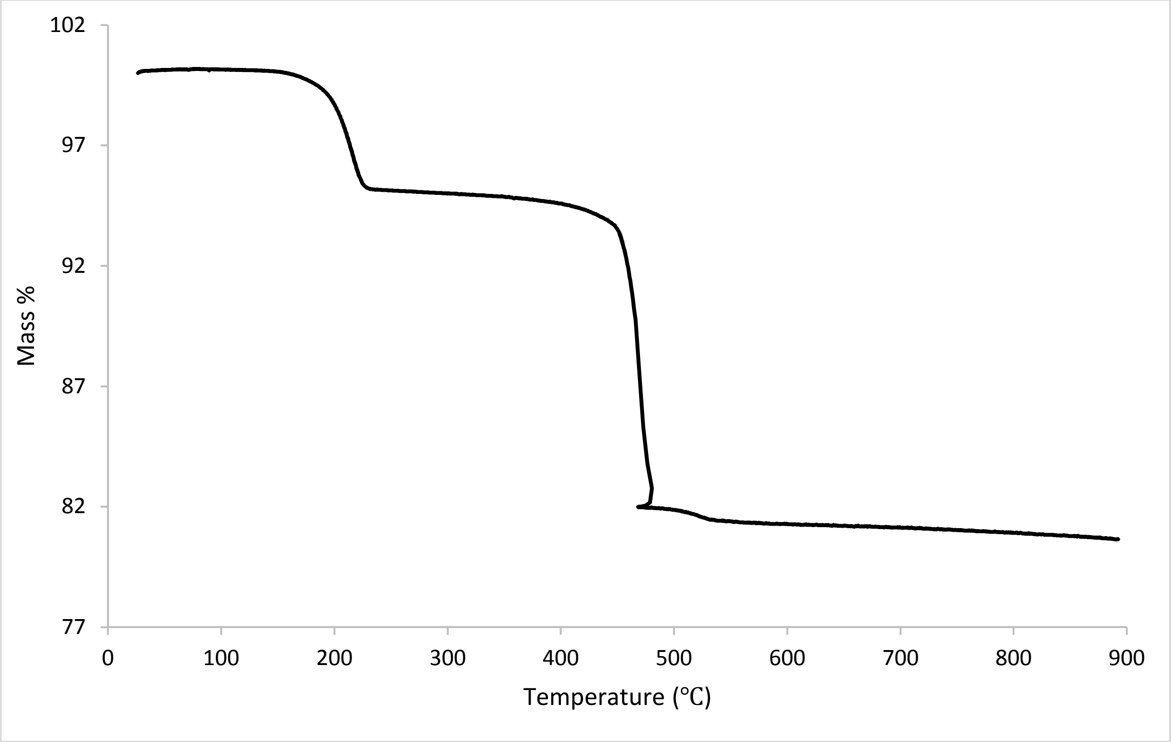

Figure 2-21 Thermal gravimetric analysis of the product from the reaction of lanthanum acetate with MoO_3.

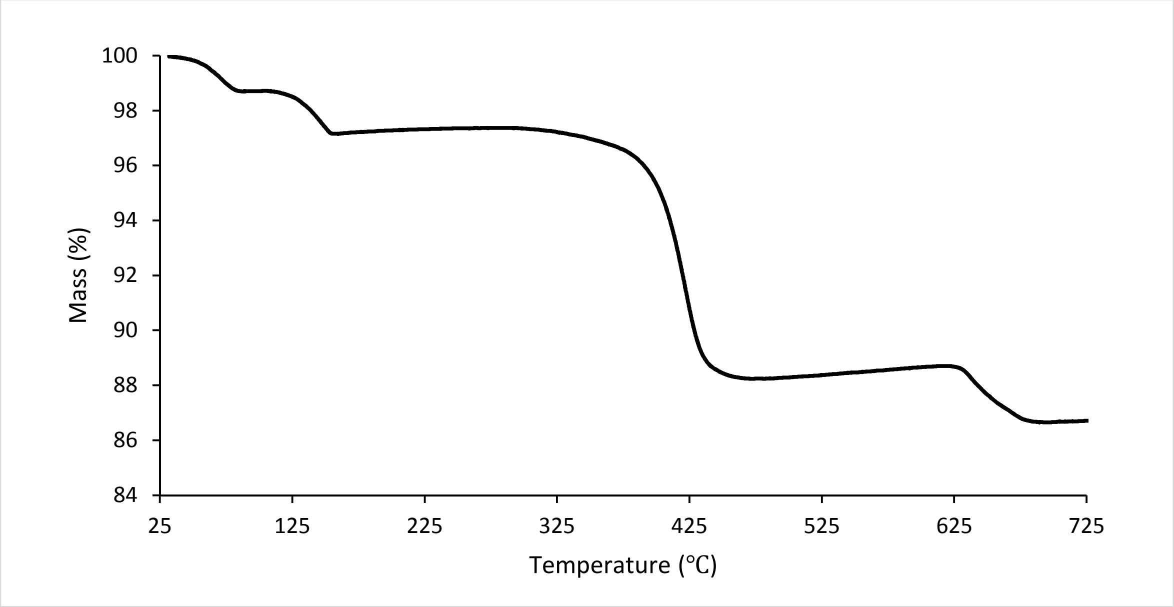

Figure 2-22 Thermal gravimetric analysis of the product from the reaction of lanthanum acetate with H_2WO_4.

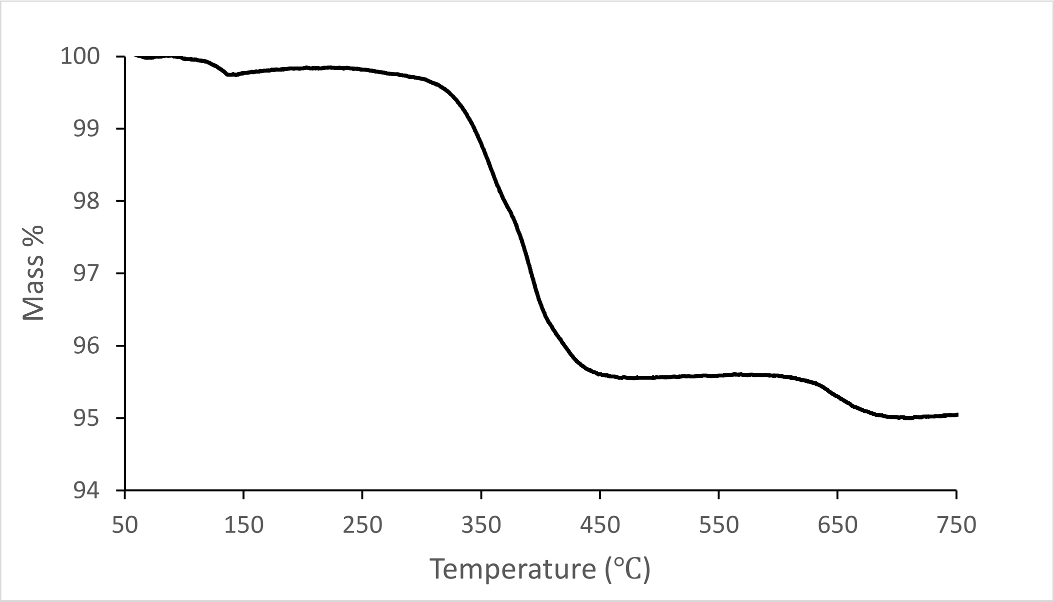

Figure 2-23 Thermal gravimetric analysis of the product from the reaction of lanthanum acetate with WO_3.

The ceramic yield of the product from the reaction of lanthanum acetate with MoO_3 was 80.64% (Figure 2-21). Assuming the formation of $La_2Mo_2O_9$, this corresponds to a formula weight for the reaction product per lanthanum of 380.5 g/mol. Two weight loss steps were observed in the TGA trace. The first step was a loss of 4.87% that occurred over the temperature range of 157□ to 246□ can be attributed to the loss of 1.05 equivalents of water. The second weight loss of 13.83 %, occurred over the range of 324□ to 564□ corresponded to the conversion of one equivalent of acetate to a half equivalent of oxide. A strong exotherm indicated that this step involved combustion of the organic residues. This caused a temporary temperature rise that caused the squiggle in the TGA trace at 484˚C. Therefore, the thermal gravimetric analysis led to a formula $La(O_2CCH_3)(MoO_4)\bullet 1.05H_2O$. The formula was confirmed by carbon analysis by combustion. The calculated percent carbon for this formula is 6.39 % while the analytical result was 6.43 %.

The product from the reaction of lanthanum acetate with tungstic acid had four weight steps leading to a ceramic yield of 86.65 (Figure 2-22). A formula weight of 461.2 g/mol can be calculated per lanthanum assuming the ceramic product is $La_2W_2O_9$. The weight loss steps, the reactions involved, and the intermediate and final products formed are listed in Table 2-2. There are two initial weight loss steps that correspond to the evolution of 0.95 molar equivalents of water. There is a high temperature step in the range of 639 to 723˚C that is attributed to decomposition of one-sixth of an equivalent of carbonate to oxide and carbon dioxide as this is similar to the decomposition temperature of $La_2O_2CO_3$ derived from pyrolysis of lanthanum acetate (613 to 771˚C).[147] The formation of carbonate strongly suggests that the acetate group is associated with lanthanum and not tungsten as the latter is too highly charged to form a stable carbonate. Since a carbonate is formed, the third weight loss step must involve decomposition of acetate ions to both oxide and carbonate. The TGA data imply a formula of $La(O_2CCH_3)(WO_4)\cdot 0.95H_2O$ was also confirmed by carbon analysis by combustion as the calculated percent carbon for this formula is 5.19 % while the analytical result was 5.64 %. The slightly high value may be due to some adhering acetic acid. Notably, the slightly high yield of product of 104% supports this hypothesis.

Table 2-2 Thermal analysis results for $La(O_2CCH_3)(WO_4)\cdot 0.95H_2O$

Step	Temp. Range (˚C)	Mass Loss (%)	Reaction	Compound Formed
1	36-91	1.91	$- 0.50\ H_2O$	$La(O_2CCH_3)(WO_4)(H_2O)_{0.45}$
2	106-159	1.77	$- 0.45\ H_2O$	$La(O_2CCH_3)(WO_4)$
2	353-485	9.16	$CH_3CO_2^{-1} \longrightarrow \frac{1}{6}CO_3^{2-} + \frac{1}{3}O^{2-} + \text{volatiles}$	$LaWO_{4.17}(CO_3)_{0.33}$
4	639-723	1.92	$\frac{1}{6}CO_3^{2-} \longrightarrow \frac{1}{6}O^{2-} + \frac{1}{6}CO_2$	$LaWO_{4.5}$ ($La_2W_2O_9$)

The thermal analysis of the product from reaction of lanthanum acetate with tungsten trioxide superficially appears to similar to that produced tungstic acid except that only one water loss step was observed, and weight losses were significantly smaller. Nevertheless, acetate is certainly present. The ceramic yield at 712°C was 95.00 %. From this, the total mass of metal oxides in the product can be calculated to be 95% of the reaction yield or 3.033 g. Assuming that none of the 2.318 g of WO_3 was lost, this means the product contains 0.715 g of "$LaO_{1.5}$" which translates as 0.439 molar equivalents of lanthanum per tungsten. So, the reaction appears to be only about 44% complete.

The X-ray powder diffraction patterns of the as-isolated reaction products $La(O_2CCH_3)(MoO_4){\bullet}1.05H_2O$ and $La(O_2CCH_3)(WO_4){\bullet}0.95H_2O$ (Figures 2-24 and 2-25, respectively) show that the products are crystalline and that they were not contaminated with starting material. There were no matches to these patterns in the ICDD database indicating that these materials are novel and there are no other compounds with similar structures. The pattern for $La(O_2CCH_3)(WO_4){\bullet}0.95H_2O$ has a strong peak at low angle ($2\theta = 5.4463^\circ$) and much weaker peaks through the rest of the pattern. This indicates that the structure is most likely a layered structure. If so, assigning the first X-ray peak to hkl=001, indicates a d-spacing of 14.83 Å. By comparison, the distance between the tungsten centers in adjacent layers in tungstic acid is 5.4463 Å.[3] Thus, if this is a layered compound, a significant separation between the layers must exist. In order for this to be the case, the acetate groups must extend into the inter layer space. An example of a structure with acetates intercalated between metal oxide or hydroxide layers is provided by copper hydroxy acetate, $Cu_2(OH)_3(CH_3COO){\bullet}H_2O$, (Figure 2-26) where the spacing between layers is 9.464 Å.[9]

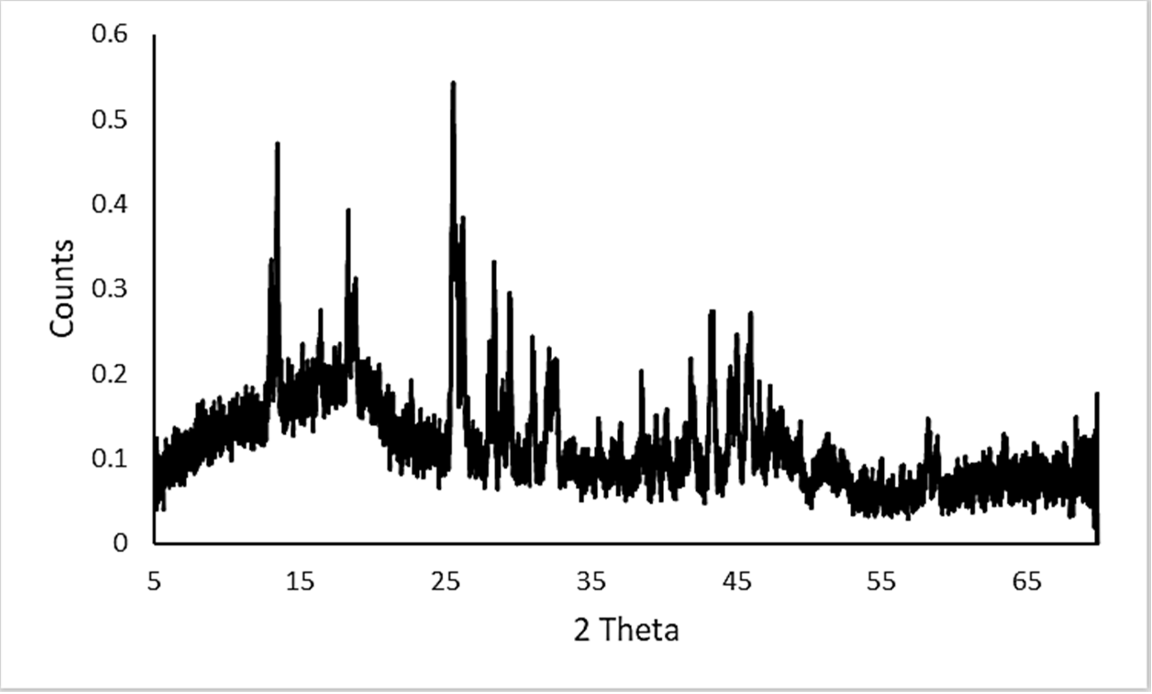

Figure 2-24. XRD pattern of $La(O_2CCH_3)(MoO_4)•1.05H_2O$

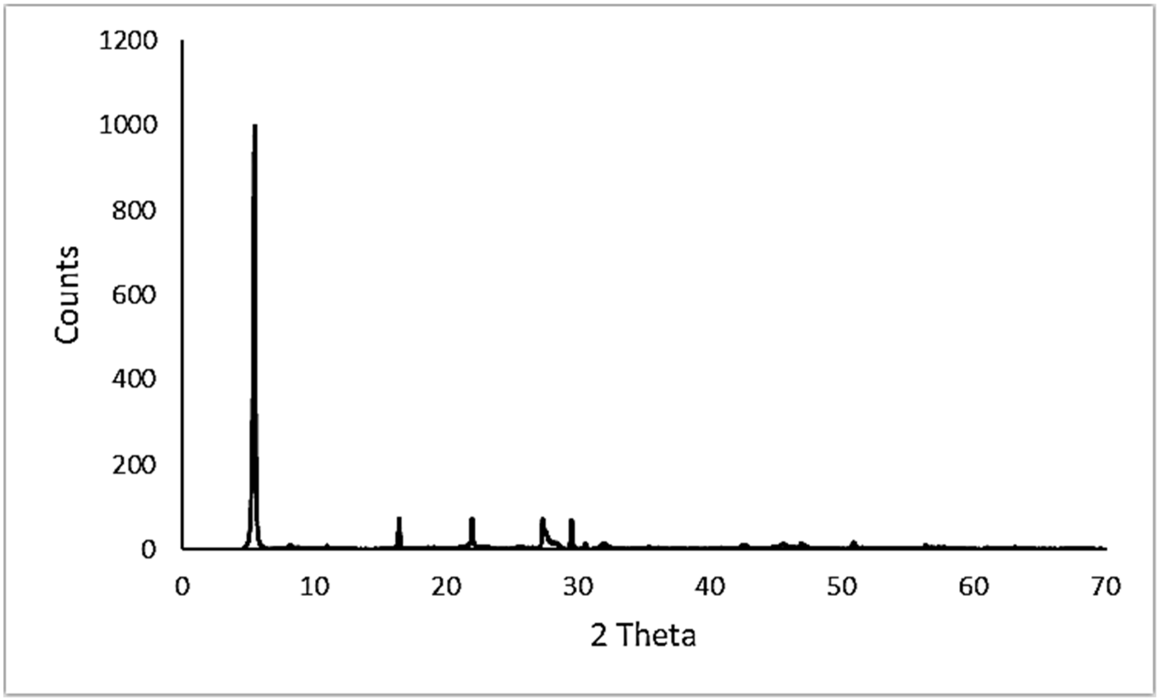

Figure 2-25. XRD pattern of $La(O_2CCH_3)(WO_4)•0.95H_2O$

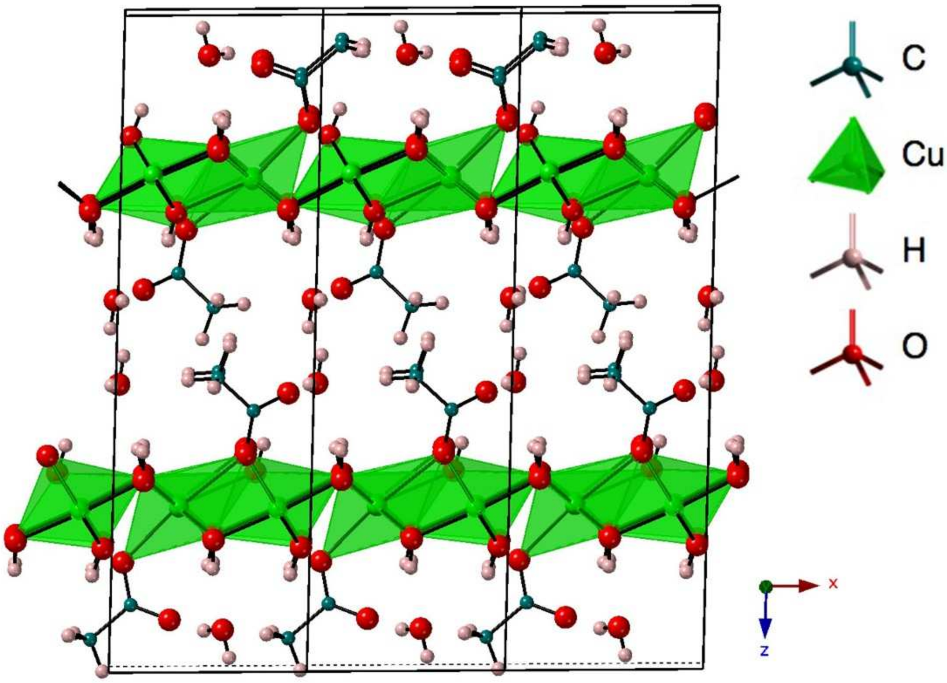

Figure 2-26. Crystal structure of $Cu_2(OH)_3(CH_3COO)\bullet H_2O$. Drawn with data from Reference [9].

The analysis so far has provided information concerning the building blocks of the structures of $La(O_2CCH_3)(MoO_4)\bullet 1.05H_2O$ and $La(O_2CCH_3)(WO_4)\bullet 0.95H_2O$, the actual structures remain uncertain for now. The literature does provide two structures that might be indicative of the appearance of $La(O_2CCH_3)(MoO_4)\bullet 1.05H_2O$ and $La(O_2CCH_3)(WO_4)\bullet 0.95H_2O$. The first of these is $[Ce(H_2O)(MoO_4)]_2$[fumarate].[10] Essentially, the formula of this compound is related to the compounds in this investigation by replacement of two acetates by a dicarboxylic acid (and molybdenum by tungsten in one case). The structure of the compound consists of slabs of cerium and molybdenum polyhedral that are bridged by fumarate groups. Each carboxylate of the fumarate bridges two cerium atoms, a motif that was determined to exist in $La(O_2CCH_3)(WO_4)\bullet 0.95H_2O$. In this material, there are two crystallographically independent Ce ions, one of which is eight-coordinated by five different unidentate molybdate anions, two carboxylates, and one terminal water molecule. The second one is nine-coordinate due to one of the molybdate anions being bidentate. A close up of the coordination around lanthanum is shown in Figure 2-28. Note that half of the molybdate ions share a corner with two cerium centers creating edge-shared cerium polyhedra. There is a significant possibility that the structure of La(O_2CCH_3)(WO_4)•0.95H_2O has a layered structure that is related to that of [Ce(H_2O)(MoO_4)]$_2$[fumarate]. The infrared peaks for the bridging carboxylates in this compound occur at ν_{as} = 1521 cm^{-1} and ν_s = 1406 cm^{-1} and Δ of 115 cm^{-1}.[10] The Δ value is quite close to that of La(O_2CCH_3)(WO_4)•0.95H_2O which has ν_{as} = 1544 cm^{-1} and ν_s = 1420 cm^{-1} and Δ of 124 cm^{-1}. La(O_2CCH_3)(MoO_4)•1.05H_2O might also have a structure that contains a similar arrangement of the metal oxide blocks but it does not appear to be layered and has two independent chelating acetates instead of bridging ones.

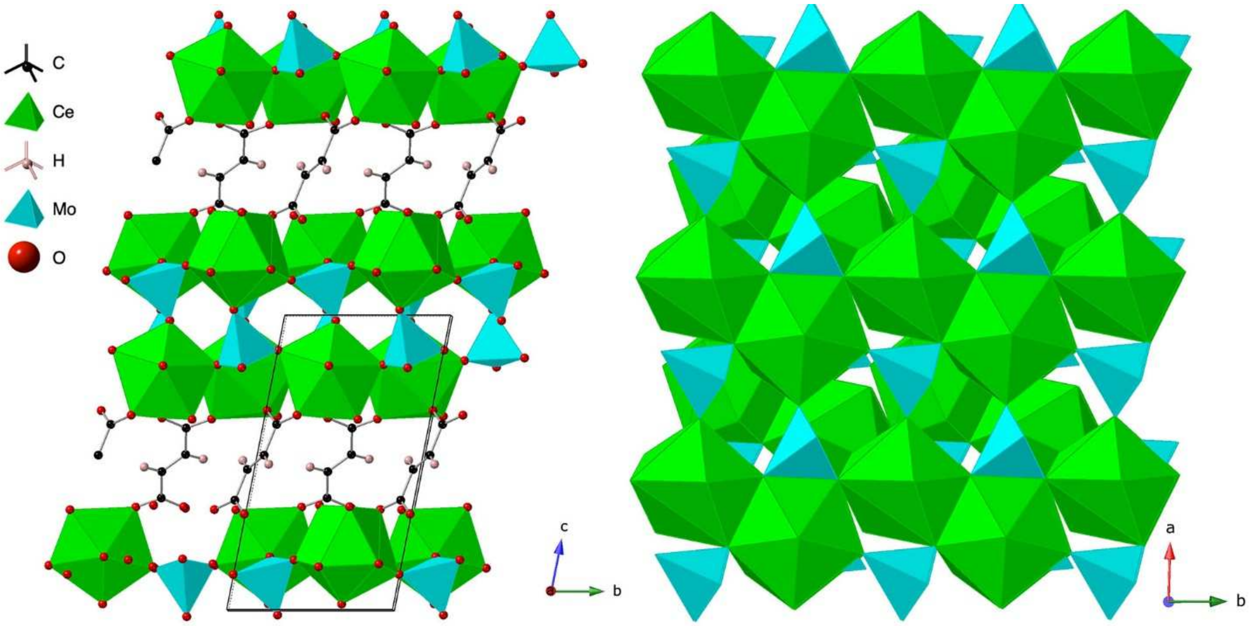

Figure 2-27. Two views of the crystal structure of [Ce(H_2O)(MoO_4)]$_2$[fumarate]. Drawn with data from Reference [10].

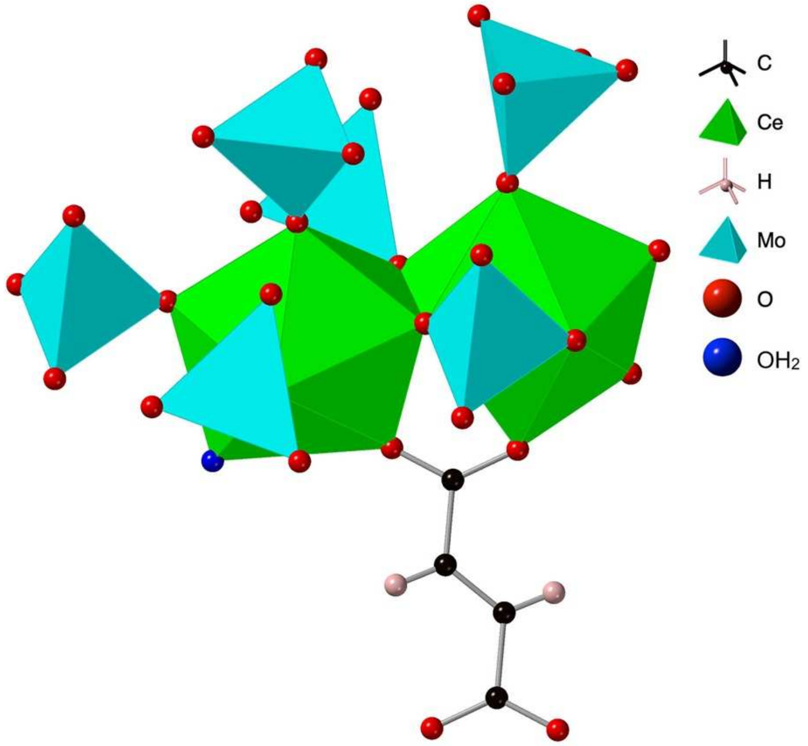

Figure 2-28. View of the coordination around lanthanum in $[Ce(H_2O)(MoO_4)]_2$[fumarate]. Drawn with data from Reference [10].

The second example of a structure that may be similar to that of the products from the reaction of lanthanum with MoO_3 and H_2WO_4 (especially the latter) is $[La(H_2O)WO_4]_2$[1,5-NDS] where 1,5-NDS is 1,5-naphthalenedisulfonate (Figure 2-29).[10] This is a pillared layered structure that is similar to the fumarate structure described above. The inorganic sheets contain trilayers of lanthanum and tungstate polyhedra with the latter sandwiched between the former. The lanthanum ions that are eight-coordinate and are ligated by one water molecule, two 2,5-NDS anions, and five tungstate anions (Figure 2-30). Note that the tungstate ions share corners with two lanthanum ions so that adjacent lanthanum ions are also linked by shared corners. The sulfonate groups of the 1,5-naphthalenedisulfonate bridge two adjacent lanthanum atoms in the mixed-metal oxide sheet and also pillar the layers by connecting to two lanthanum ions in one layer with one of the sulfonate groups and to two lanthanum ions in the adjacent layer with the other sulfonate group.

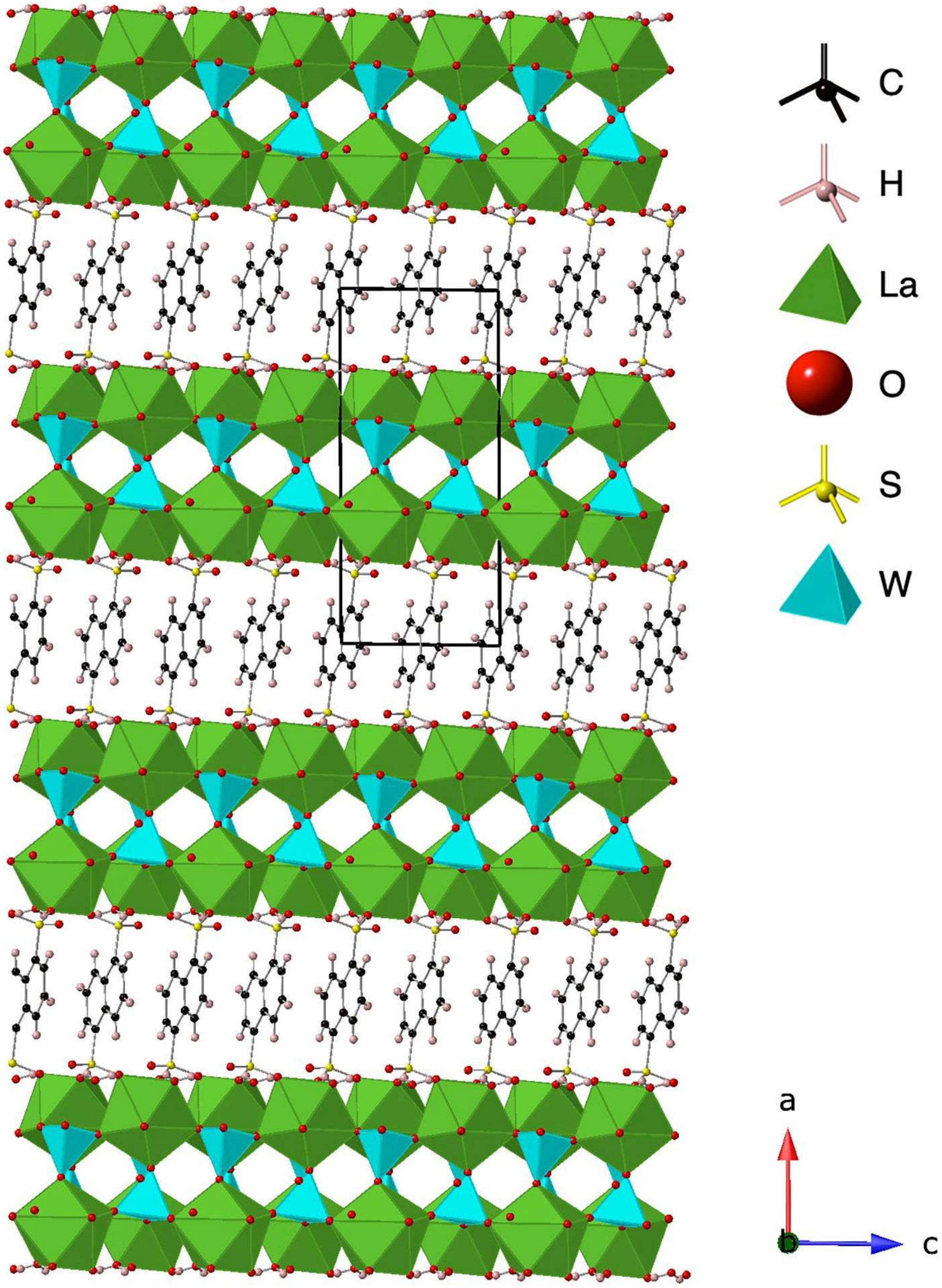

Figure 2-29. Crystal structure of $[La(H_2O)WO_4]_2[1,5\text{-NDS}]$. Drawn with data from Reference [10].

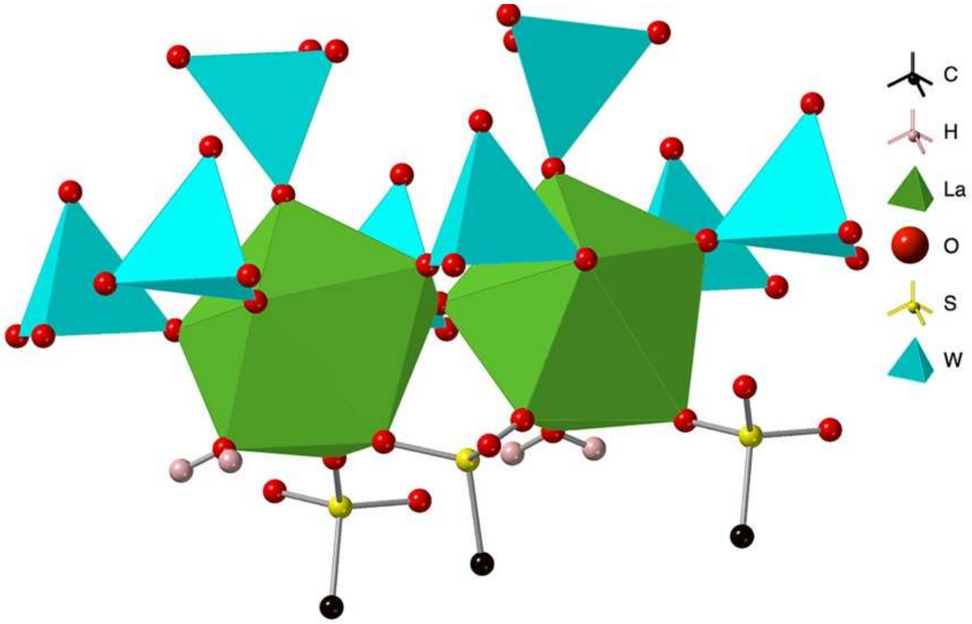

Figure 2-30. Arrangement of ligands around $[La(H_2O)WO_4]_2[1,5\text{-NDS}]$. Note that the NDS ligands are truncated. Drawn with data from Reference [10].

$La(O_2CCH_3)(MoO_4){\bullet}1.05H_2O$ and $La(O_2CCH_3)(WO_4){\bullet}0.95H_2O$ crystalize with the correct stoichiometry to produce $La_2Mo_2O_9$ and $La_2W_2O_9$, respectively, when calcined. X-ray powder diffraction (Figures 2-31 and 2-32) confirmed that these phases are indeed formed when the precursor compounds are heated to the temperatures required for complete removal of acetate and water groups. This was 650˚C for lanthanum acetate molybdate and 750˚C for lanthanum acetate tungstate. Interestingly, the high-temperature cubic form of $La_2Mo_2O_9$ was obtained (β-$La_2Mo_2O_9$, ICDD# 00-23-1145). It is not obvious why the cubic structure was stabilized so that a phase change to the alpha form does not occur. This might be due to the tightly-controlled stoichiometry of lanthanum to molybdenum or some impurity incorporated into the ceramic product. In the case of $La_2W_2O_9$, the low temperature triclinic phase was produced (α-$La_2W_2O_9$, ICDD # 01-75-7873). However, the sample was heated well below the temperature at which transition to β-$La_2W_2O_9$ occurs (1070˚C).

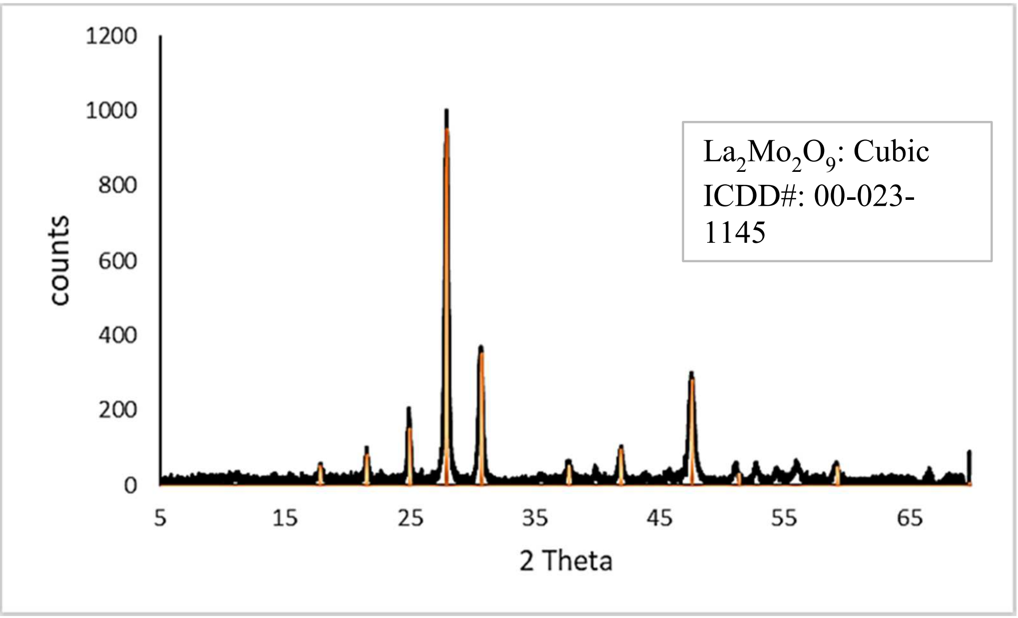

Figure 2.31. The XRD pattern and match with ICDD# 00-23-1145 (β-$La_2Mo_2O_9$) for the ceramic produced by calcining $La(O_2CCH_3)(MoO_4)•1.05H_2O$ at 650 □

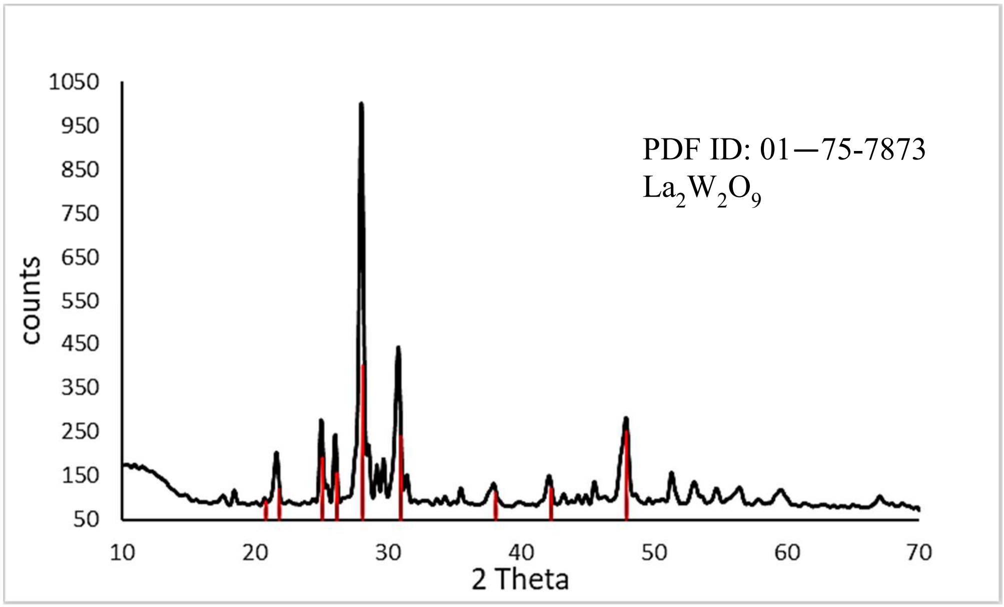

Figure 2.32. The XRD pattern and match with ICDD# 00-23-1145 (α-$La_2W_2O_9$)for the ceramic produced by calcining $La(O_2CCH_3)(WO_4)•0.95H_2O$ at 750□

The infrared spectra of the ceramic products (Figures 2-33 and 2-34) demonstrated the disappearance of the acetate groups and displayed significant changes in the molybdenum oxygen vibrations and tungsten oxygen vibrations as the molybdate and tungstate ions were converted into polymeric metal oxides with coordination numbers greater than four. The narrow vibrations of $La(O_2CCH_3)(MoO_4)•1.05H_2O$ were replaced with a very broad unresolved peak that extended over the range from the 535 to 940 cm^{-1} upon firing at 650˚C. On the other hand, the tungsten oxygen vibrations remain sharp peaks. Peaks are observed at 903, 737, 672, and 572 cm^{-1} that are likely due to La-O stretches, and W-O stretches in WO_5 and WO_6 polyhedra.

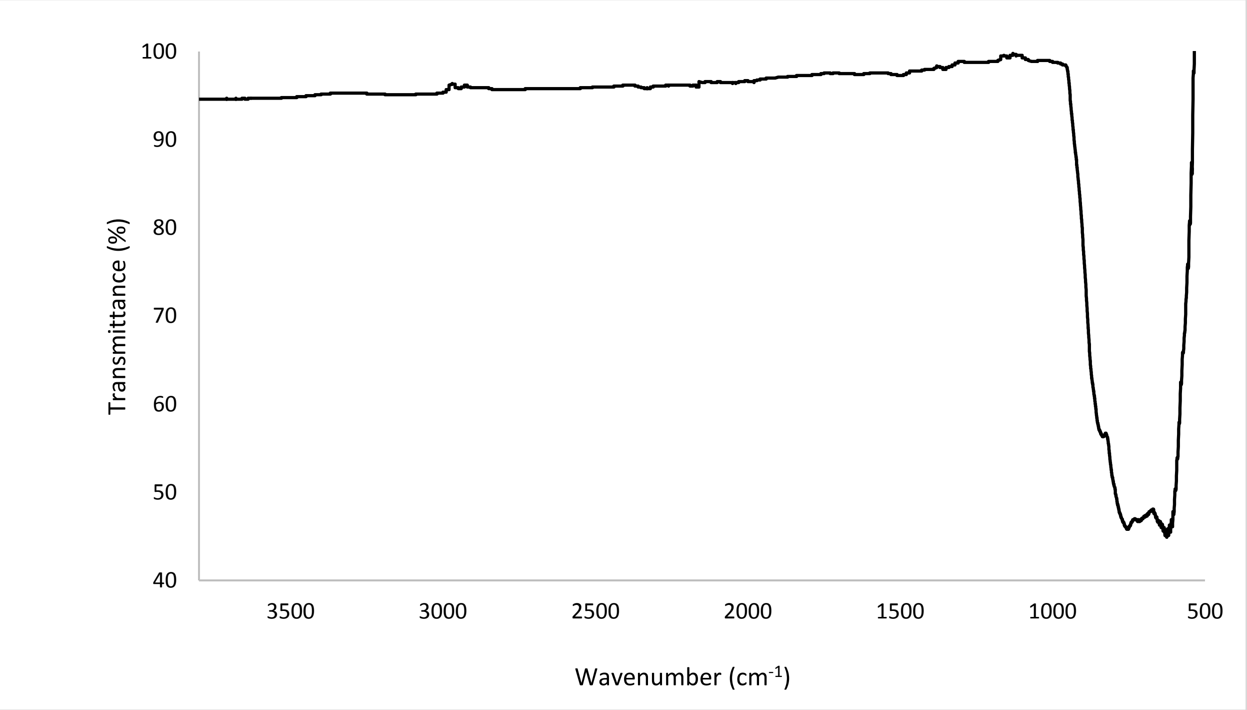

Figure 2-33. Infrared spectrum of β-$La_2Mo_2O_9$ produced from the 650˚C calcination of $La(O_2CCH_3)(MoO_4)•1.05H_2O$

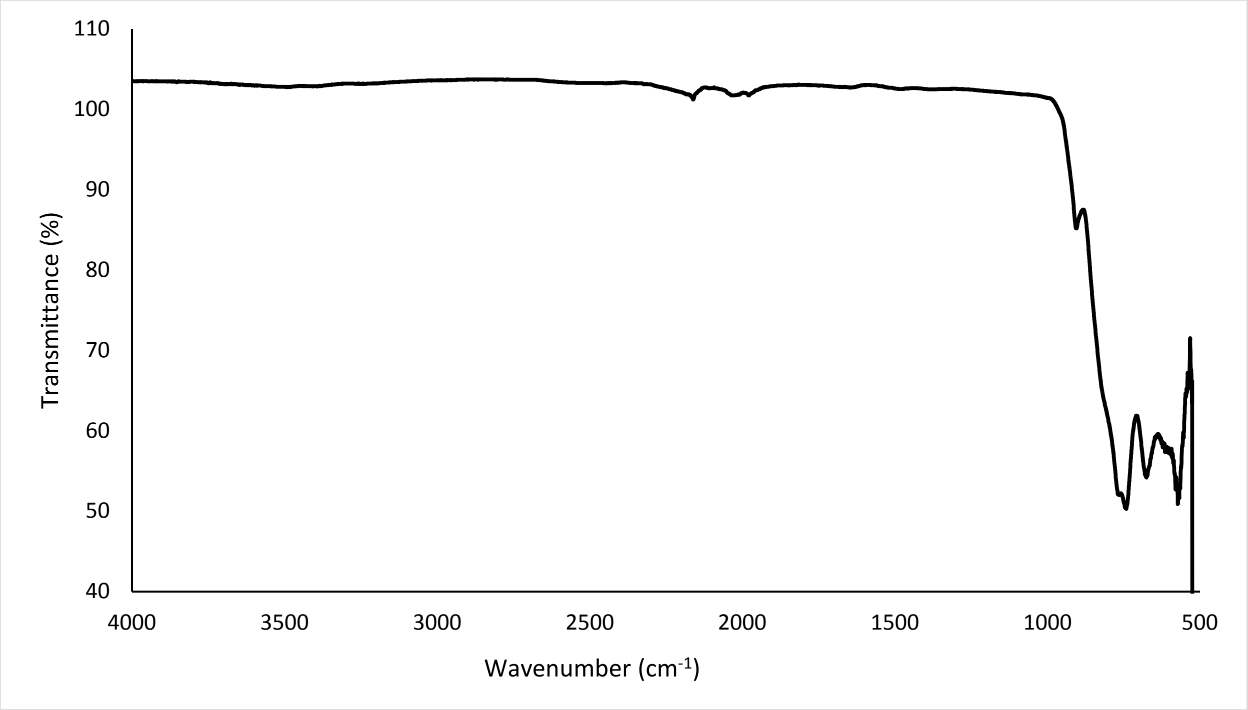

Figure 2-34. Infrared spectrum of α-$La_2W_2O_9$ produced from $La(O_2CCH_3)(WO_4)•0.95H_2O$

CONCLUSIONS

The reaction of lanthanum acetate with molybdenum trioxide and tungstic acid produce compounds that contain acetate and MO_4^{-2} (M=Mo or W) anions and approximately one water molecule per lanthanum ion. Despite the similarities in composition, the products are structurally very distinct from each other. The molybdenum product, $La(O_2CCH_3)(MoO_4)•1.05H_2O$, contains two distinct acetate groups that are chelating while $La(O_2CCH_3)(WO_4)•0.95H_2O$ contains bridging acetate groups. Further, the latter compound has an XRD pattern indicative of a layered structure. It would be useful to be able to perform single crystal X-ray structure determination, but the materials were only obtained as powders. It is possible that hydrothermal reactions might produce suitable crystals, so such reactions are worth pursuing.

Notably $La(O_2CCH_3)(MoO_4)\cdot 1.05H_2O$ and $La(O_2CCH_3)(WO_4)\cdot 0.95H_2O$ have the ideal stoichiometry of the metals for the preparation of $La_2Mo_2O_9$ and $La_2W_2O_9$. Crystallographic determination of stoichiometry provides much better control of composition than that achievable by weighing of reagents. These compounds can be converted to β-$La_2Mo_2O_9$ and α-$La_2W_2O_9$ at temperatures (650 to 750˚C) much lower than 1100˚C that is required for their synthesis via the ceramic method. The direct synthesis of the oxide conductor, β-$La_2Mo_2O_9$, that is stable at room temperature may result from its precise stoichiometry. This could revolutionize the preparation and use of this material in solid oxide fuel cells and sensors.

The process developed in this investigation could be applied to the synthesis of a myriad of other desired multi-metallic molybdenum oxide and tungsten oxide materials. Further, the reaction could also be performed with a mixture of metal acetates to produce doped materials for phosphors and lasers or novel phases that combine several metals. The development of the application of the Acetate/MO_X process to the preparation of tungsten oxide containing compound is particularly meritorious since it opens the avenue to the preparation of a large suite of industrially-important materials.

CHAPTER III

IRON MOLYBDATES VIA REACTIONS OF MOLYBDENUM(VI) OXIDE IN ACETATE BUFFER

Introduction

As discussed in the previous chapter, reaction of MoO_3 or H_2WO_4 with metal acetates (the MO_x/Acetate process) provides a convenient route for preparation of bimetallic oxides containing either molybdenum or tungsten. Unfortunately, the universal application of this process is hampered in several cases where water stable metal acetates are not water-stable. This is the case for iron since iron acetate, $Fe(O_2CCH_3)_3$, decomposes to $[Fe_3O(O_2CCH_3)_6(H_2O)_3](O_2CCH_3)$. This basic iron acetate contains a trinuclear iron cation with three equivalent Fe^{3+} octahedral centers and a central triply bridging oxide at the center of the equilateral triangle (Figure 3-1).[11] Each pair of iron centers around the triangle are connected by two bridging carboxylates.

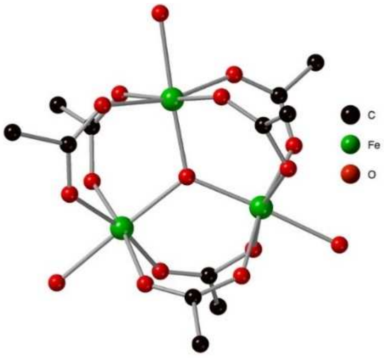

Figure 3-1. Structure of the $[Fe_3O(O_2CCH_3)_6(H_2O)_3]^+$ cation. Drawn with data from Reference [11].

In the investigation reported herein, the possibility of preparing iron molybdenum oxides using an acetate buffer and a soluble monomeric iron salt such as nitrate was investigated. The iron-molybdenum-oxygen phase diagram (Figure 3-2) only shows one stable iron(III) molybdenum oxide, namely the ortho molybdate, $Fe_2(MoO_4)_3$ or $Fe_2Mo_3O_{12}$.[12] The other oxides contain iron(II) i.e. $Fe^{II}_2Mo^{IV}_3O_8$, $Fe^{II}Mo^{VI}O_4$, and $Fe^{II}_2Mo^{IV}O_4$. In the investigation reported herein, only reactions in an air atmosphere were pursued so the compounds containing air-sensitive ferrous ions were not targeted. Therefore, the main target was $Fe_2(MoO_4)_3$.

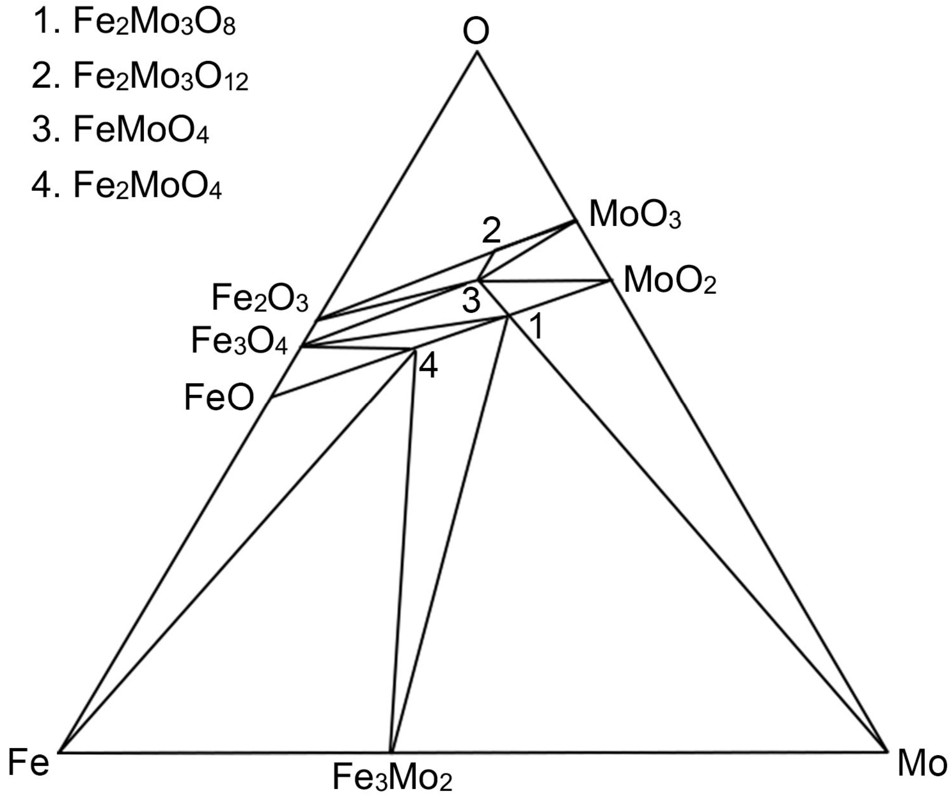

Figure 3-2. Phase diagram for the iron-molybdenum-oxygen system. Adapted from Reference [12].

Ferric molybdate finds considerable application as a catalyst for numerous organic transformations primarily as a selective oxidation catalyst but also as a photocatalyst for degradation of organic molecules, and as an esterification catalyst. Its catalytic applications include conversion of methanol to formaldehyde, oxidation of propylene to propylene oxide, oxidative dehydrogenation of ethane, esterification of oleic acid to form biodiesel, degradation of pesticides, photocatalytic degradation of 4-chlorophenol, photodegradation of dyes with visible light, propylene ammoxidation, oxidation of methane to methanol, oxidation of toluene to tolualdehyde, and other similar oxidations of aromatic methyl groups to aldehydes.[148-159] In industry, the production of formaldehyde from methanol and propylene oxide from propylene are the most significant catalytic applications.

Two views (down the b-axis and down the c-axis) of the monoclinic crystal structure of $Fe_2(MoO_4)_3$ at room temperature are shown in Figure 3-3.[13] It contains eight crystallographically-unique iron atoms that are coordinated by six oxygens from six-different corner-sharing MoO_4 tetrahedra (Figure 3-4). The Fe-O bond distances vary widely from 1.911Å to 2.087Å to with an average distance of 1.992 A. The MoO_4 tetrahedra of the twelve molybdenum atoms are in rather distorted oxygen tetrahedra with an overall average Mo-O distance of 1.756 Å. The Mo-O bond distances vary from 1.660 Å to 1.779 Å. When viewed down the c-axis it can be seen that molybdate layers are sandwiched between layers composed of FeO_6 octahedra. Notably, the MoO_4 tetrahedra have no contact with each other and the same is true for the FeO_6 octahedra. As a result, the structure is very open and contains channels over 5 Å in diameter down the b and a axes. This may have some influence on its small-molecule catalytic reactions. The windows down the c-axis are somewhat diamond shaped with a length of approximately 5.5 Å and a width of 5.5 Å

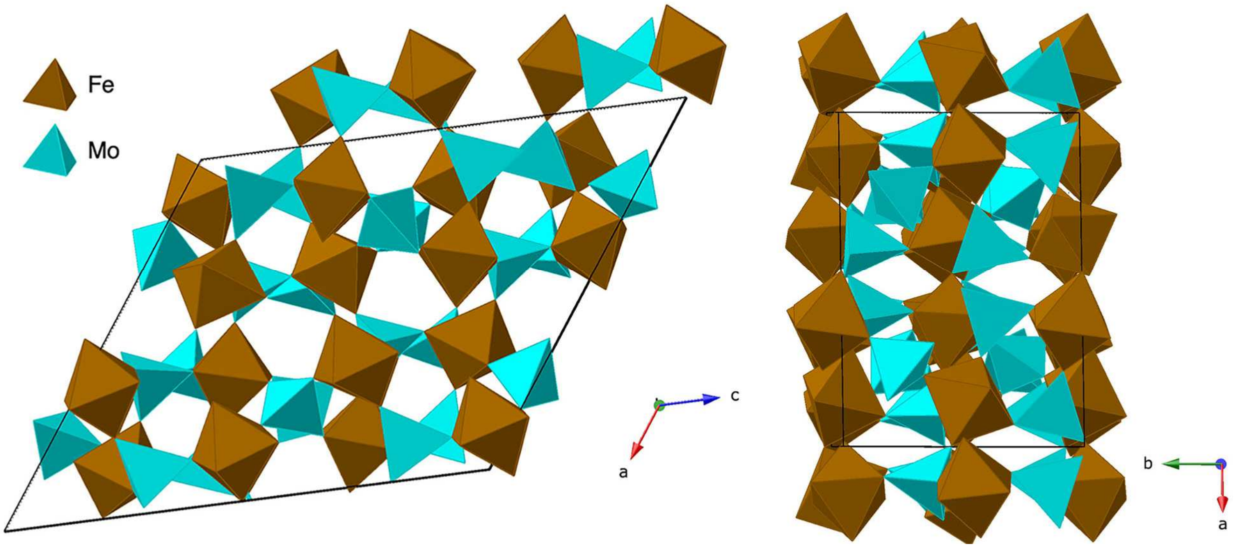

Figure 3-3 Two views of the crystal structure of α-$Fe_2(MoO_4)_3$. Drawn with data from Reference [13].

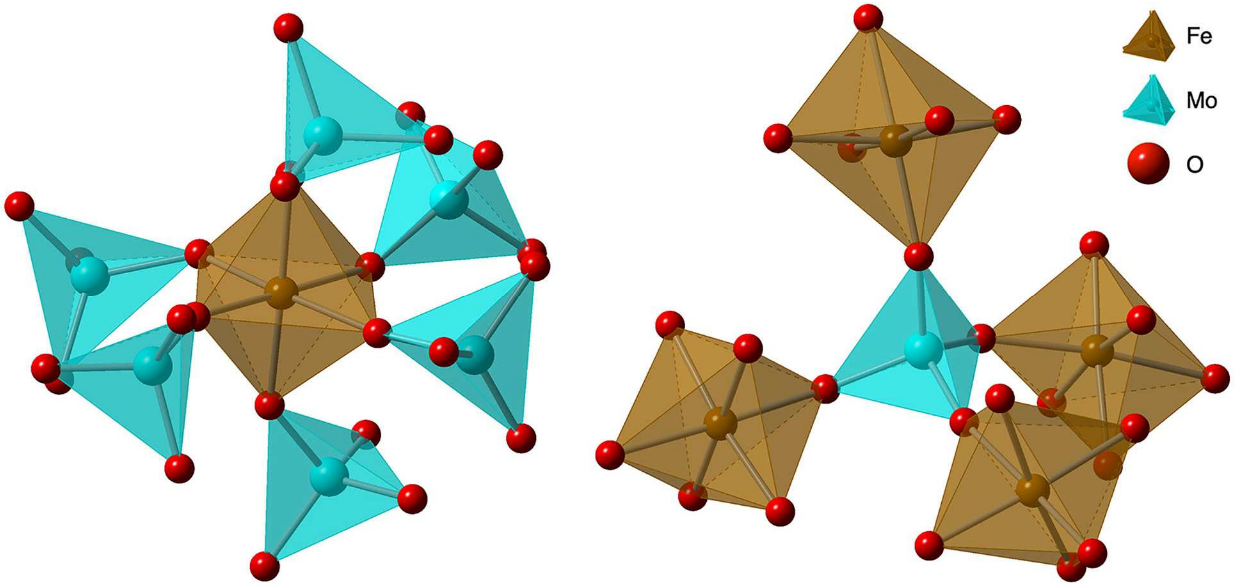

Figure 3-4 The coordination environment of iron and molybdenum in $Fe_2(MoO_4)_3$. Drawn with data from Reference [13].

At 507˚C the monoclinic structure transforms to an orthorhombic phase, β-$Fe_2(MoO_4)_3$, that exhibits low or even negative thermal expansion properties. The phase transition is accompanied by an expansion in volume per $Fe_2(MoO_4)_3$ unit and results in a material that is isostructural to $Sc_2(WO_4)_3$.[14] It is a three-dimensional framework built from MoO_4 tetrahedra that are corner-linked to FeO_6 octahedra (Figure 3.5). With the increased symmetry, the number of unique iron ions is reduced to one and the number of unique molybdenum ions has dropped to two The arrangement of molybdate ions around the iron ion is changed from that of as the molybdate tetrahedra have twisted and tilted into new orientations (Figure 3-5). The a-b plane changes significantly as the molybdate layers have opened up along the b-axis into two interdigitated molybdate layers that extend down the c plane. The ac plane now has separated alternating corrugated layers of FeO_6 octahedra and MoO_4 tetrahedra. There is still no Fe-O-Fe or Mo-O-Mo bonding in the high temperature structure.

The iron ions occupy slightly distorted octahedra, with average Fe–O=1.984±0.013 Å and Fe–O distances ranging from 1.974 to 2.005 Å. Two crystallographically independent Mo ions are surrounded by somewhat distorted tetrahedra: the Mo–O distances vary from 1.734 to 1.748 Å with the average being 1.740±0.010 Å.

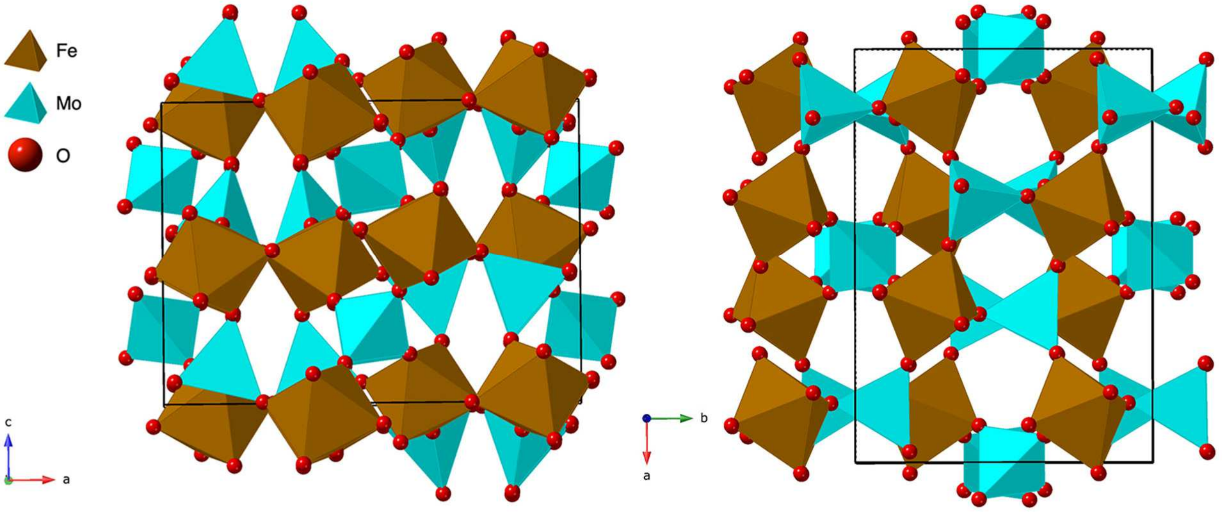

Figure 3-5 Two views of the crystal structure of β-$Fe_2(MoO_4)_3$. Drawn with data from Reference [14].

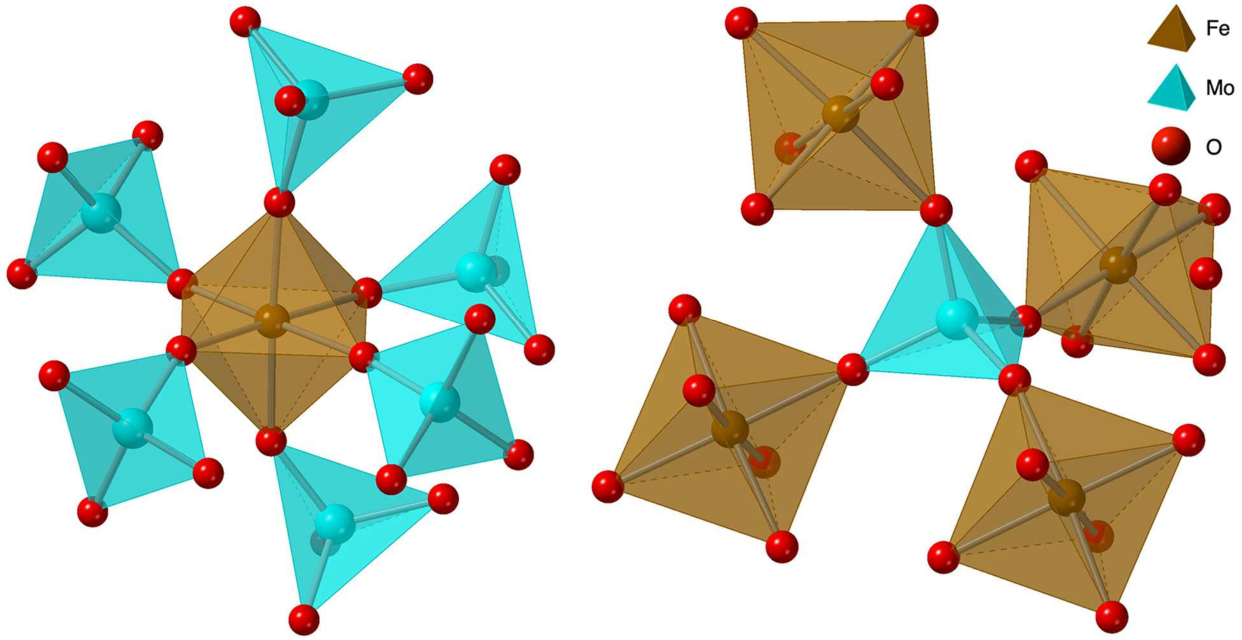

Figure 3-6 The coordination environment of iron and molybdenum in β-$Fe_2(MoO_4)_3$. Drawn with data from Reference [14].

The high temperature form of $Fe_2(MoO_4)_3$ is sometimes described as being paraelastic while the low temperature form is ferroelastic.[14-15] These terms refer to the change from the "normal" expansion of a material with increasing temperature (ferroelastic) to one where the expansion is close to zero (paraelastic). This is shown for $Fe_2(MoO_4)_3$ in Figure 3.7[15]. X-ray thermal expansion measurements showed that as temperature increases the b-axis and c-axis lattice constants of β-$Fe_2(MoO_4)_3$ while the a-axis constant decreases such that a constant value of the molecular volume is observed over a large temperature range. Note that, as shown in Figure 3.5, the a-axis has large empty window that likely accommodates the metal ions as that axis constricts. There is considerable interest in materials such as β-$Fe_2(MoO_4)_3$ that have near zero or negative coefficients of expansion for structural application where thermal expansion/contraction interferes with mechanical tolerances or causes fatigue and cracking. Unfortunately, the high transition temperature of 507˚C from monoclinic β-$Fe_2(MoO_4)_3$ to orthorhombic β-$Fe_2(MoO_4)_3$

restricts the application of this material. However, Song and co-workers were able to monoclinic-to-orthorhombic phase transition temperature to -170˚C by co-substitution of Zr^{4+} and Mg^{2+} (average 3+ charge) for Fe^{3+} in $Fe_2(MoO_4)_3$ to form $Fe_{2-x}(ZrMg)_{0.5x}(MoO_4)_3$ (x=0-1.8). For example, $Fe_{0.4}(ZrMg)_{0.8}(MoO_4)_3$ maintains the orthorhombic structure as low as -170˚C. Furthermore, the coefficient of thermal expansion could be tailored so that near-zero values were obtained around the composition of ($Fe_{0.3}(ZrMg)_{0.85}(MoO_4)_3$. These results definitely show promise for the development of low-cost near-zero thermal expansion materials that can be used over wide temperature ranges.

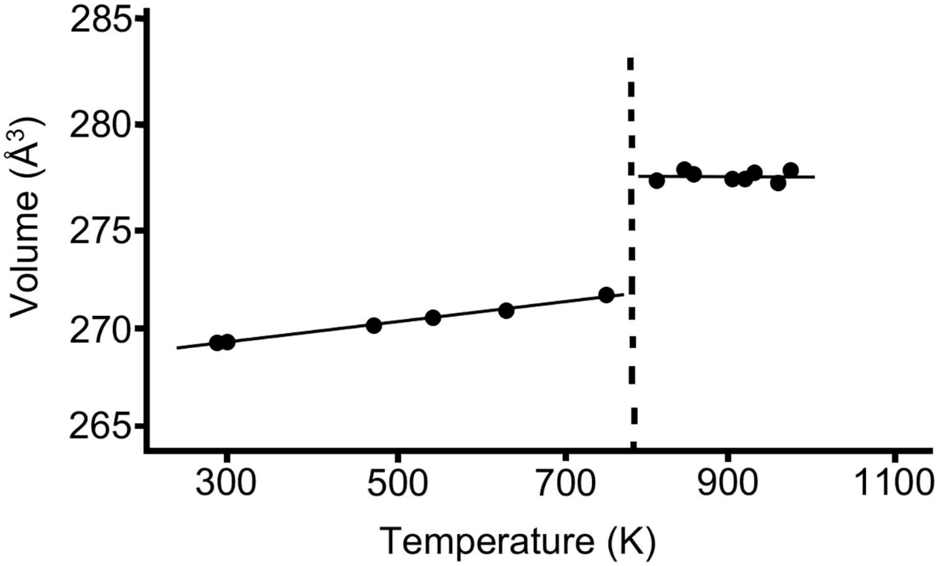

Figure 3-7 Molecular volume of $Fe_2(MoO_4)_3$ as a function of temperature. Figure adapted from Reference [15].

While the number of known phases containing ferric ions, molybdenum(VI) ions, and oxide ions is extremely limited, $Fe_2(MoO_4)_3$ is an extremely important target due to it extremely wide applications as a catalyst and potential applications as near zero or negative coefficient of expansion materials. Furthermore, a means of low-temperature synthesis could result in the isolation of metastable phases with useful properties. Therefore, an investigation of the reaction between ferric nitrate and molybdenum trioxide in acetate buffer was performed and the experiment and results are described below.

Experimental

Materials and Methods

Commercially available reagents of ACS grade purity or better were used without further purification. Water was purified by reverse osmosis followed by deionization. Metal concentrations were determined by microwave plasma–atomic emission spectrometry using an Agilent 4200 microwave plasma atomic emission spectrometry (MP-AES) instrument and NIST-traceable standards. Thermogravimetric analysis (TGA) was performed using a Mettler TGA instrument. Thermal decomposition experiments were performed in an alumina crucible under an air atmosphere with a ramp rate of 5 °C min^{-1}. Infrared spectra were recorded on a Nicolet iS50 FT-IR spectrometer in the range of 4000–500 cm^{-1} with 4 cm^{-1} resolution. X-ray powder diffraction (XRD) patterns were obtained using a Bruker AXS D-8 Advance X-ray powder diffractometer with Cu Kα radiation. Crystalline phases were identified using a search/match program and the PDF-2 database of the International Center for Diffraction Data. Surface areas were determined by nitrogen physisorption using the Brunauer–Emmett–Teller (BET) method on a Quanta Chrome Nova 1200 instrument. An ISFET pH meter (model IQ125) obtained from IQ Scientific, USA was used to measure pH. An acetate buffer solution was prepared by dissolving sufficient glacial acetic and sodium acetate in water to produce a solution that was 0.1 M in each reagent.

Reaction of iron nitrate with molybdenum trioxide in acetate buffer

The required amount of $Fe(NO_3)_3 \cdot 9H_2O$ was dissolved in 100 ml of sodium acetate buffer and then either 10 mmol or 20 mmol of molybdenum trioxide was added to the solution. The mixture was stirred magnetically and heated at reflux for 4 days. After cooling the solid products were isolated by filtration using a fine sintered glass filter, washed copiously with water, and dried in a vacuum oven at room temperature. A sample of the solid was calcined at 670˚C to determine the ceramic yield after removal of water and/or hydroxide groups. The pH of the reddish orange filtrate solution was measured. The experimental details for the four different ratios of iron to molybdenum are provided in Table 3.1

Table 3-1. Experimental details for reactions of ferric nitrate with molybdenum trioxide in acetate buffer.

Fe:Mo Ratio	Mass Iron Nitrate (g)	mmol Iron Nitrate	Mass MoO_3 (g)	mmol MoO_3	Actual Fe/Mo Ratio	Yield (g)	Color	Ceramic Yield (%)	pH of filtrate
1:2*	2.033	5.032	1.440	10.00	0.5032	1.549	Red	91.40	4.20
1:1	4.037	9.992	1.439	9.997	1.001	2.017	Reddish Brown	84.52	4.20
2:1	8.072	19.98	1.447	10.05	1.988	3.564	Red	92.35	3.51
3:1	12.116	29.99	1.435	9.969	3.008	4.233	Brown	85.53	2.92
1:2	4.066	10.06	2.879	20.00	1.987	3.097	Red	91.40	4.20

* This reaction was run with 20 mmol of MoO_3 instead of 10 mol like the rest of the reactions. Therefore, the amounts of reagents and yields are halved for comparative purposes. The actual values are provided in the last column.

Results and Discussion

The reactions of ferric nitrate with molybdenum trioxide in acetate buffer with varying ratios of iron to molybdenum produce solids with differing colors indicating that more than one product is forming. The filtrate from the reaction is colored reddish orange indicating that some iron remains in solution and it is likely that molybdenum is also present in solution. The yields increase almost linearly with a slope close to 1 with the increase in Fe:Mo ratio with a slight anomaly at the 2:1 reaction (Figure 3-8). On the other hand, the pH is identical at the end of the reactions for the 1:2 and 1:1 Fe-Mo reactions (4.20) but then drop by 0.69 and 0.59 for each increase in iron equivalents per MoO_3. The pH results suggest a change in reaction chemistry above the 1:1 ratio. Elemental analysis for carbon indicated that there was no significant incorporation of acetate into the solids. For the Fe:Mo ratios 1:2, 1:1, and 2:1 the percent carbon was 0.09 %, 0.26 %, 1.09 %, respectively. Considering that none of the other samples contained acetate and the yield was high for the 2Fe:1Mo product, it may be conjectured that the latter sample was contaminated with buffer and required further washing.

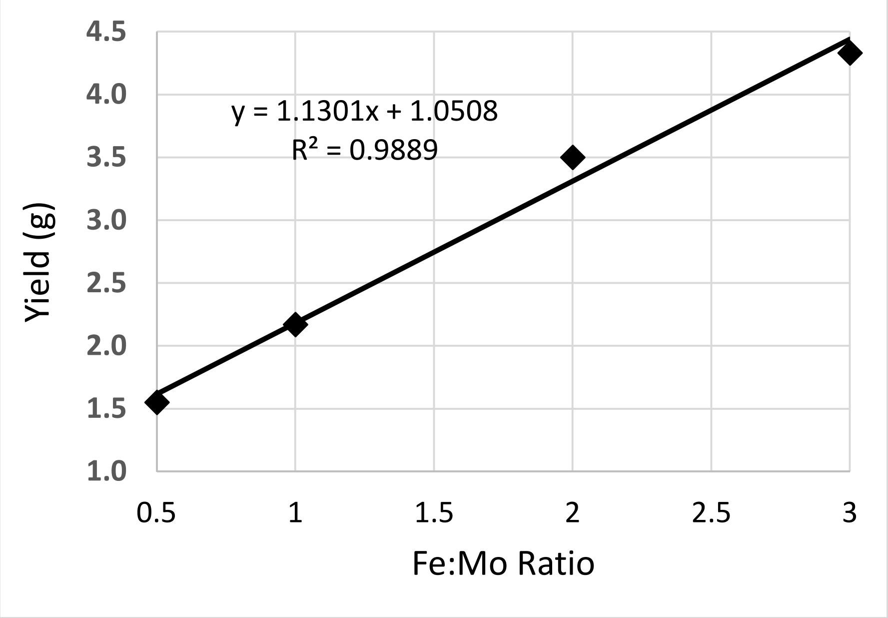

Figure 3-8. Yield as a function of the Fe:Mo ratio.

X-ray powder diffraction (XRD) analysis showed that all products were amorphous except for the 1:2 Fe:Mo reaction which showed a definite XRD pattern that did not match a known phase (Figure 3-9). The X-ray reflections were strong indicating that this material was reasonably crystalline.

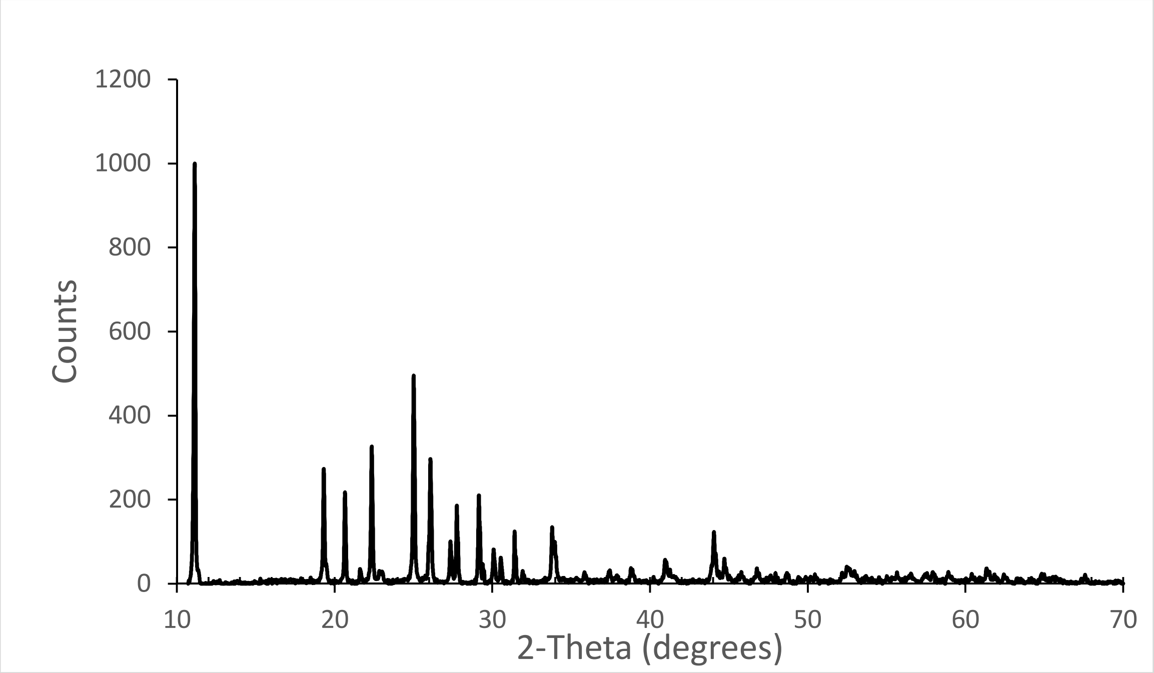

Figure 3-9 XRD pattern of the solid product from 1:2 Fe:Mo reaction in acetate buffer.

The thermal gravimetric analysis trace for this material (Figure 3-10) showed three unresolved weight loss steps: 1.00 weight% from room temperature to 110˚C, 4.40 % from 110 to 315˚C, and 1.93 % from 315 to 479˚C. These weight losses may be due to loss of lattice water at lower temperatures and metal bound water at higher temperatures. For example, TGA curves for the amorphous hydrated ferric sulfate samples show a gradual weight loss to approximately 150°C followed by a steeper loss to approximately 200°C. The slope of the TGA curves becomes gradual again by 250°C and there is a small slow sustained loss out to 450˚C thereafter.[160] On the other hand Fe(OH)SO_4 does not dehydroxylate until 536˚C.[161] Thus, if the hydrated ferric molybdenum oxide product behaves similarly to the ferric sulfate systems, than the presence of hydroxide groups is unnecessary to explain the higher temperature losses in its TGA curve. The infrared spectrum of the product (Figure 3-11) has peaks that support the presence of water including a broad peak at 3417 cm^{-1} due to O-H stretching in hydrogen-bonded water molecules, a peak at 1618 cm^{-1} due to H-O-H bending, and an absorption at 1394 cm^{-1} attributable to HOH rocking. There are also strong peaks at 930, 787, and 568 cm^{-1} that indicate the compound contains molybdenum-oxygen groups. The lack of absorption bands at 963 and 998 cm^{-1} indicate that $Fe_2(MoO_4)_3$ and MoO_3 are not present in the product.

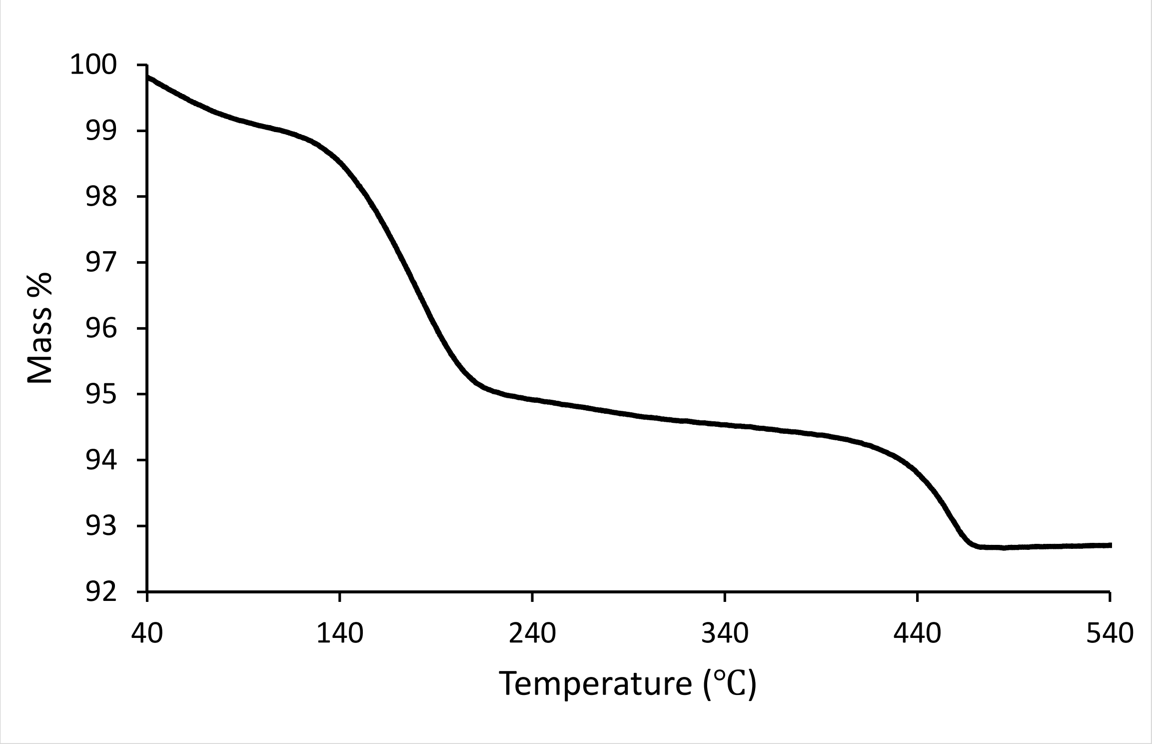

Figure 3-10 TGA trace of the solid product from 2:1 Fe:Mo reaction in acetate buffer.

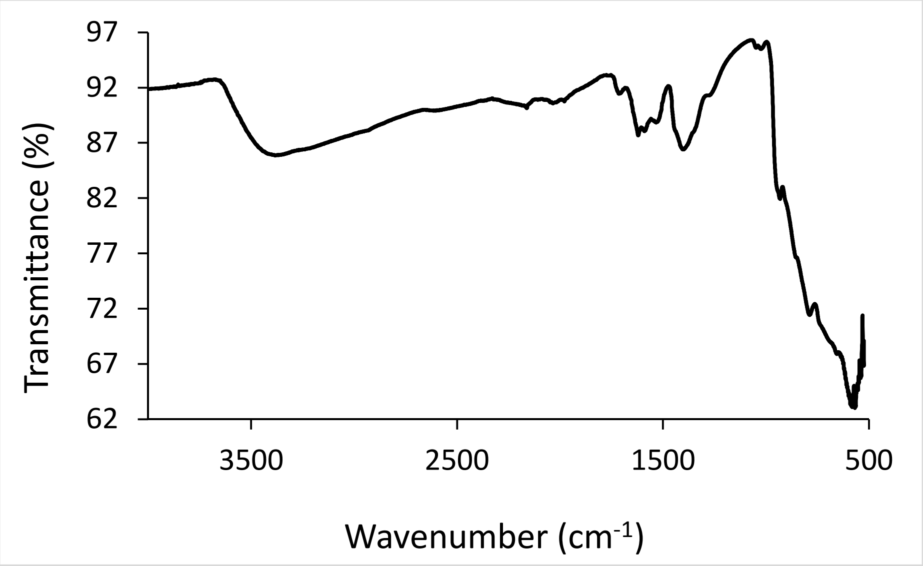

Figure 3-11. Infrared spectrum of the solid product from 1:2 Fe:Mo reaction in acetate buffer.

The XRD pattern of the 1:2 Fe:Mo reaction product calcined at 670˚C (Figure 3-12) gave the surprising result that the ceramic material was $NaFe(MoO_4)_2$. This is an excellent and surprising result since $NaFe(MoO_4)_2$ is a promising anode material for rechargeable lithium and sodium ion batteries.[16]

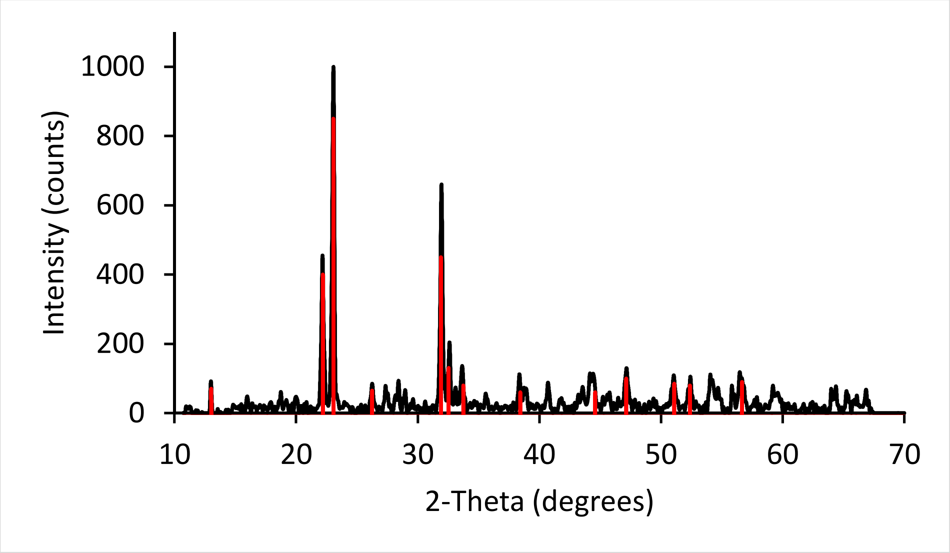

Figure 3-12. The XRD of the solid product from 1:2 Fe:Mo reaction in acetate buffer. The red lines are the pattern for $NaFe(MoO_4)_2$ (ICDD ID: 01-078-4819).

There are some small peaks present that are not due to $NaFe(MoO_4)_2$. It has been reported that the solid-state synthesis is accompanied by formation of 3% by weight of α-$NaFe_2(MoO_4)_3$.[16] The majority of small peaks match the calculated peaks for this impurity phase. A view of the crystal structure of $NaFe(MoO_4)_2$, provided in Figure 3-13, shows the channels that allow the intercalation/deintercalation of sodium ions.[16]

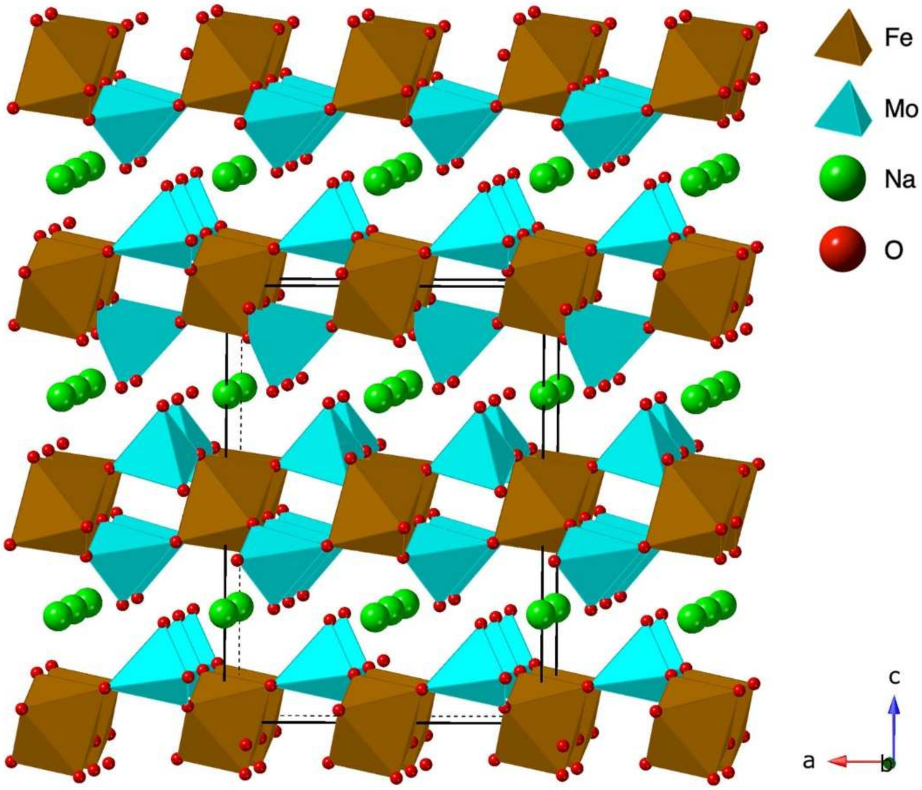

Figure 3-13. Crystal structure of $NaFe(MoO_4)_2$. Drawn with data from Reference [16].

Assuming pure $NaFe(MoO_4)_2$, the number of waters can be calculated to be 2 from the ceramic yield of 91.40%. $NaFe(MoO_4)_2{\bullet}2H_2O$ is not a known phase but, since $NaFe(MoO_4)_2$ and the mineral yavapaiite, $KFe(SO_4)_2$, are isostructural[16], hydrates of $KFe(SO_4)_2$ could be related to the product isolated from the 1Fe:2Mo reaction. The known hydrates are the monohydrate, $KFe(SO_4)_2{\bullet}H_2O$ that occurs as the mineral krausite, and the tetrahydrate, $KFe(SO_4)_2{\bullet}4H_2O$, found in nature as the mineral goldichite.[162] In the structure of goldichite,

Figure 3-14) two of the water molecules are coordinated solely to the potassium ion and two lie on one axis of the FeO_6 octahedra but also bridge to potassium (Figure 3-15).[17] Therefore, loss of the more easily removed water molecules, the two attached solely to potassium, (or sodium in the hypothetical analog $NaFe(MoO_4)_2{\bullet}4H_2O$) would produce a material with formula $KFe(SO_4)_2{\bullet}2H_2O$. It is therefore possible that the structure $NaFe(MoO_4)_2{\bullet}2H_2O$ may be related to a dehydrated goldichite structure. This is supported by a resemblance of the powder pattern of goldichite to that of $NaFe(MoO_4)_2{\bullet}2H_2O$.

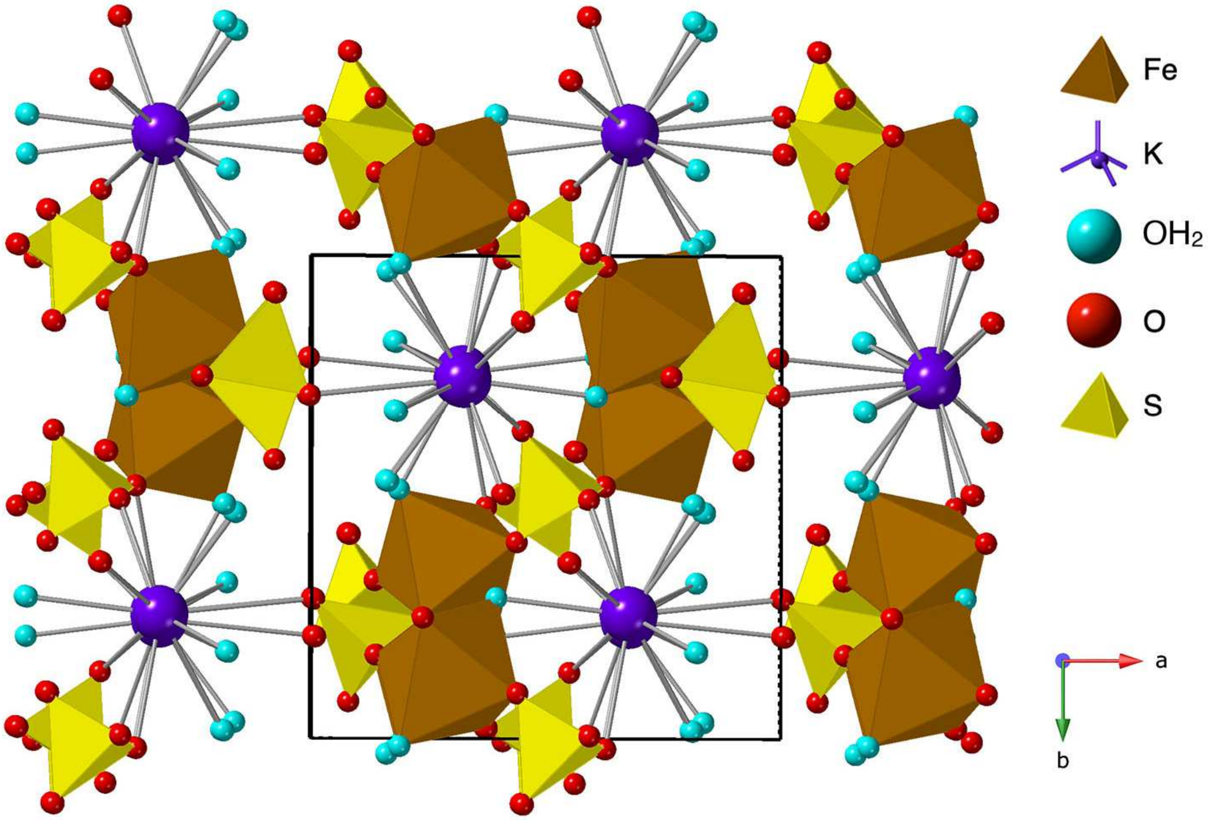

Figure 3-14. Crystal structure of goldichite, $KFe(SO_4)_2{\bullet}2H_2O$. Drawn using data from Reference [17].

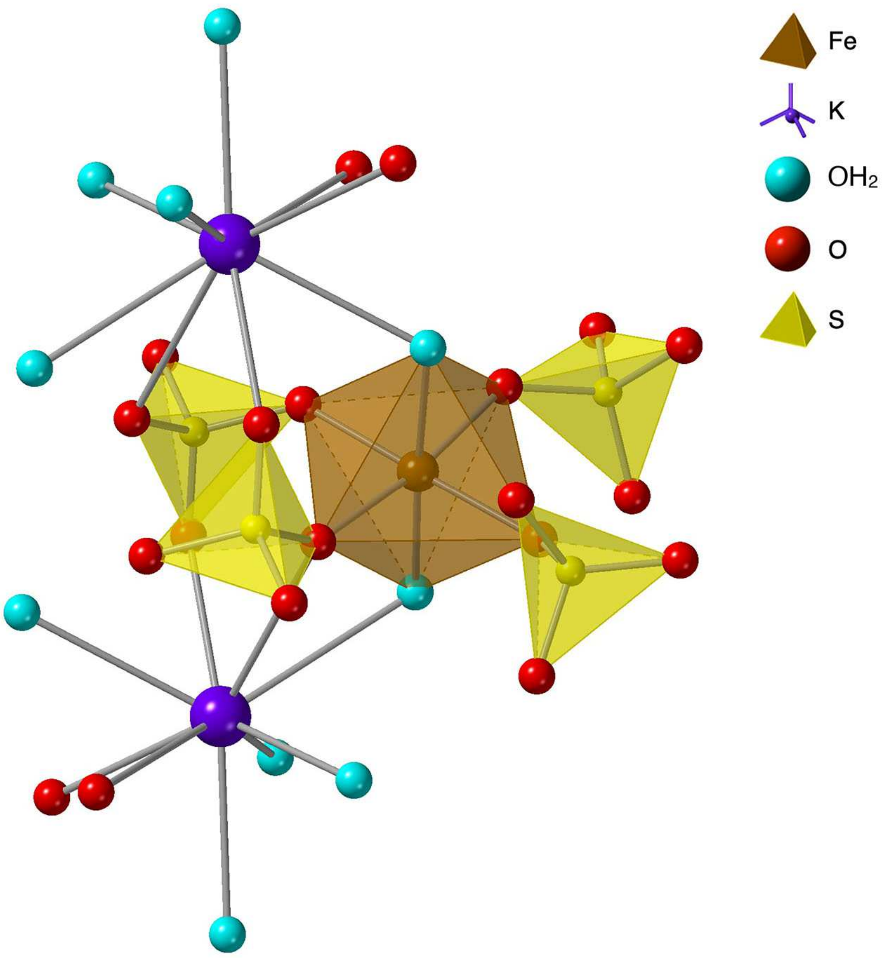

Figure 3-15. Ball and stick model of a portion of the crystal structure of Goldichite, $KFe(SO_4)_2{\bullet}2H_2O$. Drawn using data from Reference [17].

The reaction of equimolar amounts of ferric nitrate and molybdenum trioxide in acetate buffer produced a poorly crystalline product (Figure 3-16). The X-ray powder pattern contains a weak, broad reflection around 12.8˚ 2-theta. This corresponds to a d-spacing of 6.91 Å and occurs at a different position than the lowest angle peak observed for $NaFe(MoO_4)_2{\bullet}2H_2O$. Another weak broad reflection is barely resolved around 3 surface precipitation of ferric molybdate on ferrihydrite. The infrared spectrum of this product (Figure 3-17 also differs from that of $NaFe(MoO_4)_2{\bullet}2H_2O$. The broad peak for hydrogen-bonded O-H stretching occurs at higher energy (3441 vs 3417 cm^{-1}) and is accompanied by a sharp peak at 3597 cm^{-1} due to O-H non-hydrogen bonded water that is not present in $NaFe(MoO_4)_2•2H_2O$. The peak at 1619 cm^{-1} due to H-O-H bending occurs in the same position in both products but the absorption due to HOH rocking is shifted 38 cm^{-1} to lower energy (1356 cm^{-1}) There are numerous peaks for Mo-O stretching modes at 957, 930, 901, 853, 764 and 729 cm^{-1} indicating that several different coordination modes for molybdenum may be present. With the exception of the peak at 930 cm^{-1}, $NaFe(MoO_4)_2•2H_2O$ has completely different Mo-O absorption bands. Again, the lack of absorption bands at 963 and 998 cm^{-1} indicate that $Fe_2(MoO_4)_3$ and MoO_3 are not present in the product. It can be concluded from the infrared spectrum that the product contains water and molybdenum oxide species in two or more environments.

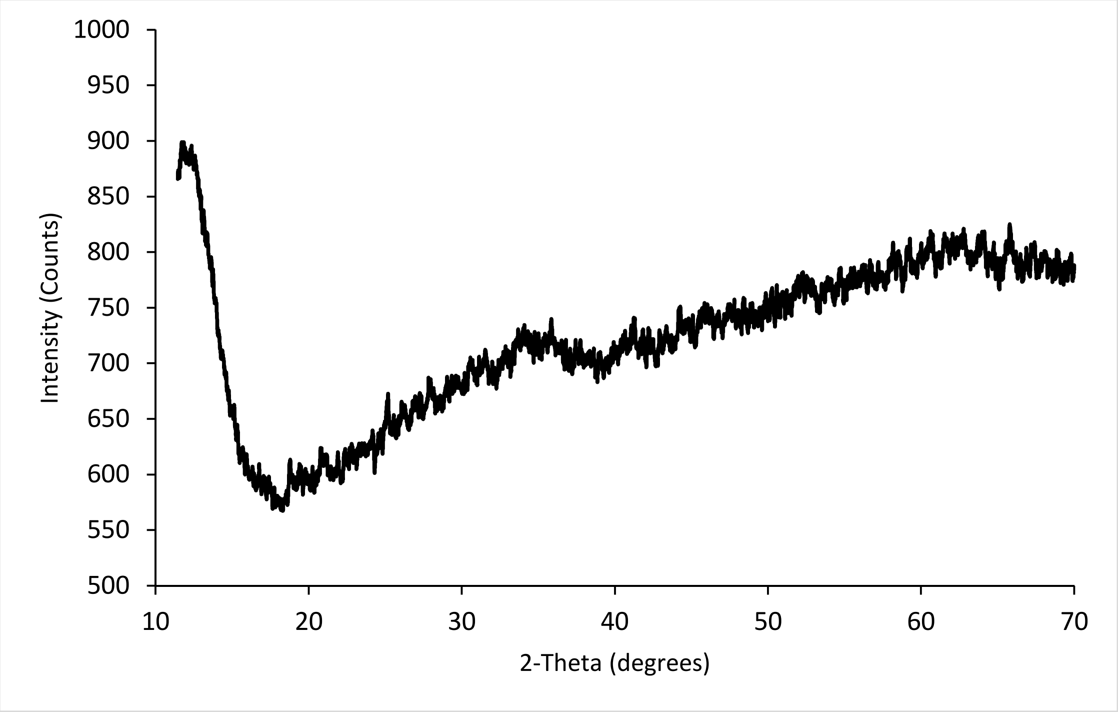

Figure 3-16. The X-ray powder diffraction pattern of the solid product from reaction of iron nitrate with MoO_3 with a 1:1 ratio in acetate buffer. The pattern was smoothed to reduce noise.

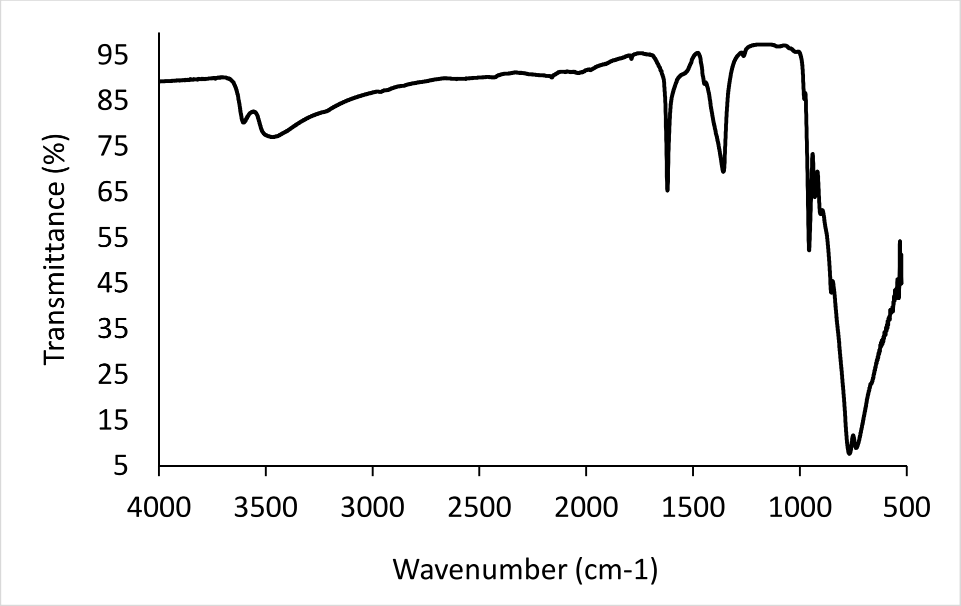

Figure 3-17. Infrared spectrum of the solid product from reaction of iron nitrate with MoO_3 with a 1:1 ratio in acetate buffer.

The thermal gravimetric analysis trace of the product (Figure 3-18) shows that water was evolved in two steps. The first from room temperature to 130˚C was 6.08 mass percent while the second step from 130˚C to 372˚C was 7.13 %. In keeping with the calcining of the other precursors, a sample of the product was heated to 670˚C and its XRD pattern is shown in Figure 3-20. It was found that the samples were primarily monoclinic α-$Fe_2(MoO_4)_3$ but there was also a considerable amount of $NaFe(MoO_4)_2$ present. Using peak intensities from the sample and the calculated XRD patterns, it was calculated that the sample was approximately 8% $NaFe(MoO_4)_2$. Thus, it can be concluded that even at a ratio of 1:1 $Fe(NO_3)_3$ to MoO_3 there is still insufficient iron available to completely form $Fe_2(MoO_4)_3$ because iron is tied up in some unknown compound in solution. $Fe_2(MoO_4)_3$ requires 0.67 molar equivalents of iron per molybdenum. The solution color is orange, so it definitely contains iron. Unfortunately, the nature of the species in solution was not investigated but this will be remedied in future work. One speculation is that the solution contains a Keggin ion such as $[FeO_4Fe_{12}(OH)_{24}(H_2O)_{12}]^{7+}$ or $[MoO_4Fe_{12}(OH)_{24}(H_2O)_{12}]^{10+}$ (Figure 3-19).

This ion composed of one central MoO_4 tetrahedron that is caged by 12 MO_6 octahedra linked to one another by bridging hydroxide groups. Notably a compound containing a trichloroacetate-complexed iron Keggin ion with the composition of $[FeO_4Fe_{12}O_{12}(OH)_{12}(O_2CCCl_3)_{12}]^{17-}$.[163] The ingredients for formation of a similar species are definitely present in the reaction mixture of iron nitrate/molybdenum trioxide/sodium acetate/acetic acid mixtures.

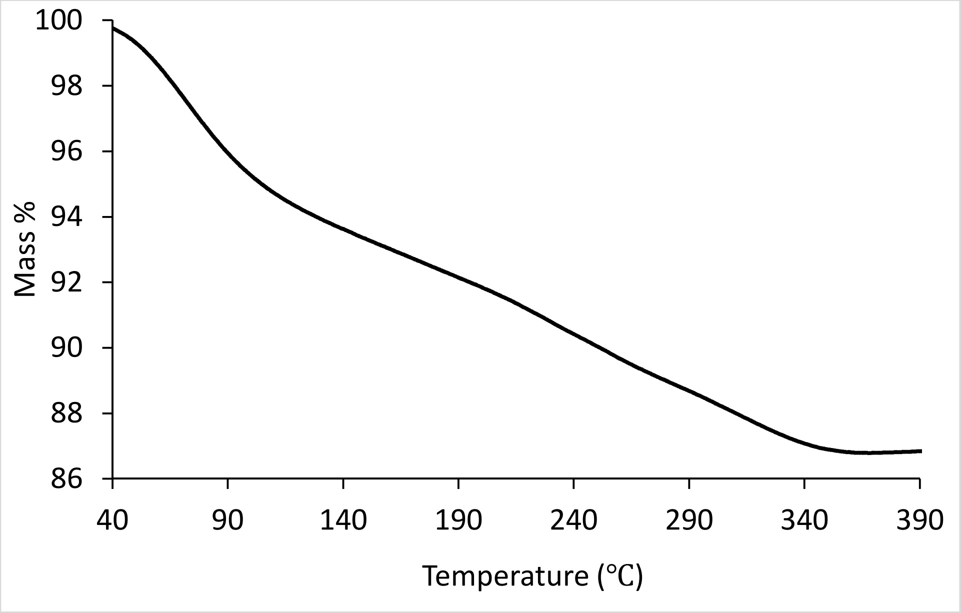

Figure 3-18. Thermal gravimetric trace of the solid product from reaction of iron nitrate with MoO_3 with a 1:1 ratio in acetate buffer.

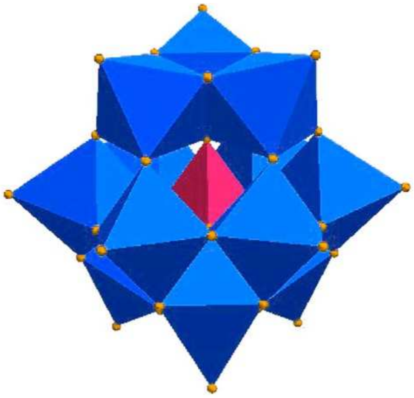

Figure 3-19. The Keggin structure with one octahedron removed to make the internal tetrahedron visible.

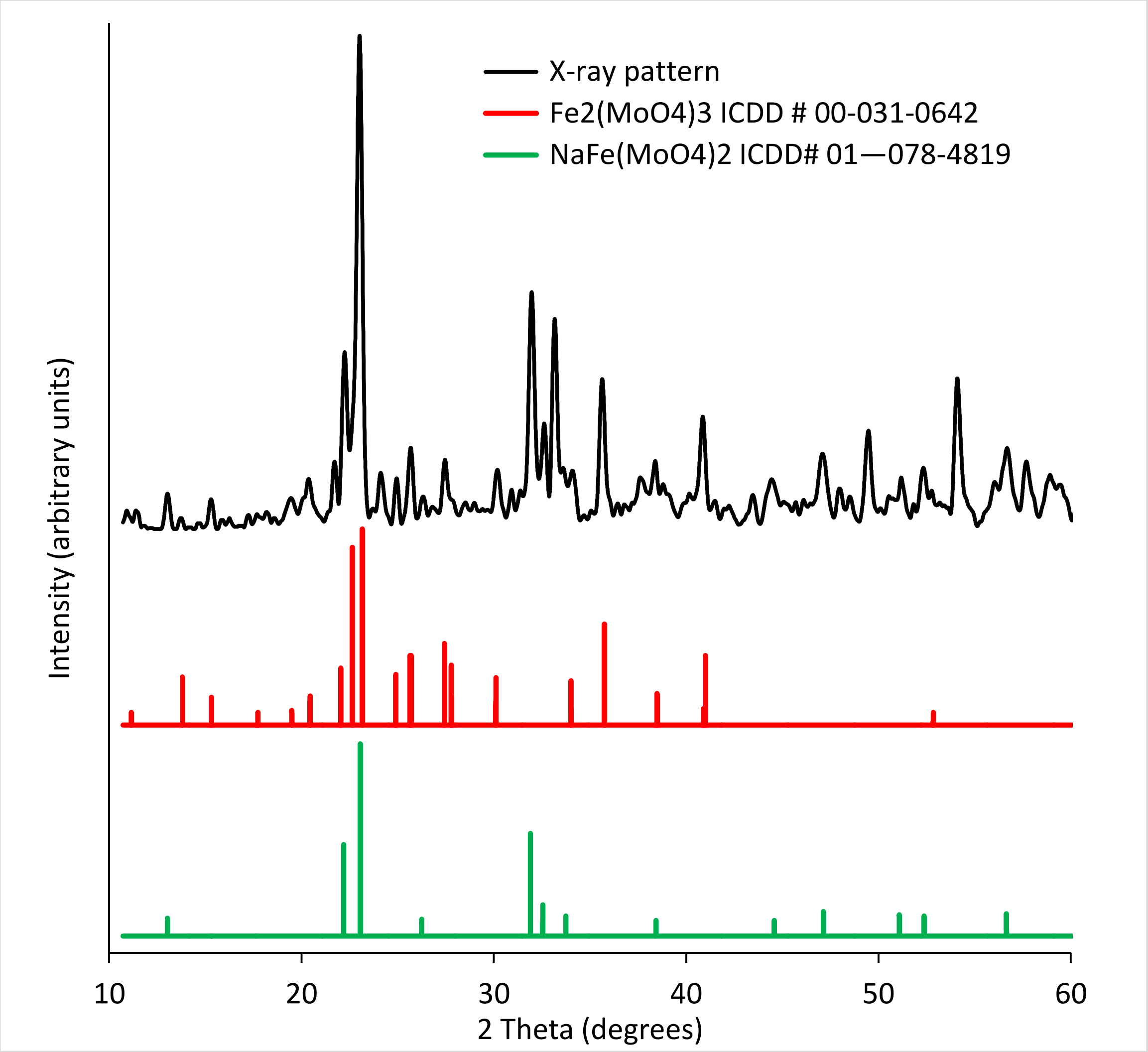

Figure 3-20. XRD pattern from reaction of iron nitrate with MoO_3 with a 1:1 ratio in acetate buffer.

The number of water molecules per formula unit in the isolated product was calculated to be 6.35. Allocating 0.725 water molecules to the 8% $NaFe(MoO_4)_2$ present, leaves 5.62 molar equivalents of water per $Fe_2(MoO_4)_3$ unit, i.e. the product was $Fe_2(MoO_4)_3(OH_2)_{5.62}$. There is a known hydrate of $Fe_2(MoO_4)_3$ called ferrimolybdite. Ferrimolybdite, $Fe_2(MoO_4)_3{\bullet}nH_2O$, is a relatively abundant mineral occurring as an oxidation product of molybdenum-bearing sulfide ores.[164] Typically the number of waters are between seven and eight. However, some of the water molecules are weakly held so dehydration at relatively mild conditions (78˚C) leads to $Fe_2(MoO_4)_3{\bullet}4H_2O$.[165] Therefore drying in vacuum can definitely form the hydrate obtained in this investigation. Unfortunately, the crystal structure of ferrimolybdite remains unsolved. A recent report of surface precipitation of ferric molybdate on ferrihydrite by Zhang and co-workers provides information that helps confirm the presence of ferrimolybdite in the isolated product from the 1:1 Fe:Mo reaction. A broad peak was observed in the XRD pattern 2-theta = 34° was attributed to ferrimolybdite and the same peak was observed in this investigation.[166] Also, a peak the peak in the isolated compound at 12.8° 2-theta, corresponds to one reported for ferrimolybdite [$Fe_2(MoO_4)_3 \cdot 6.8H_2O$] in the literature at 12.9°.[165]

Increasing the ratio of iron to molybdenum can be expected to prevent formation of $NaFe(MoO_4)_2$ and produce pure $Fe_2(MoO_4)_3$. Therefore, the amount of iron was doubled to achieve a 2:1 Fe:Mo ratio. The infrared spectrum of this material (Figure 3-21) changed dramatically from that of the 1:1 product (Figure 3-17). There were two overlapping peaks attributable to O-H stretching at 3418 and 3194 cm^{-1}. The latter peak suggests the formation of a hydrate not encountered so far in this investigation. Two peaks for H-O-H rocking at 1394 and 1336 cm^{-1} also support this hypothesis. There is a single peak for the H-O-H bend at 1621 cm^{-1}. The infrared region in which Mo-O vibrations is much simpler in the 2:1 Fe:Mo reaction product than it is for the 1:1 product indicating that a single molybdenum-containing phase had formed. Peaks were observed at 934, 810, 776 and 564 cm^{-1}. The peak at 810°C is particularly strong and corresponds to the strongest Mo-O peak in partially dehydrated ferrimolybdite (approximately $Fe_2(MoO_4)_3 \cdot 4H_2O$), that also has a peak at 810 cm^{-1}.[167]

The thermal gravimetric analysis trace for this material showed four unresolved weight loss steps: 3.07 weight% from room temperature to 146°C, 2.38 % from 146 to 273°C, 0.61% from 273 to 387°C and 0.08 % from 441 to 491°C (Figure 3-22).

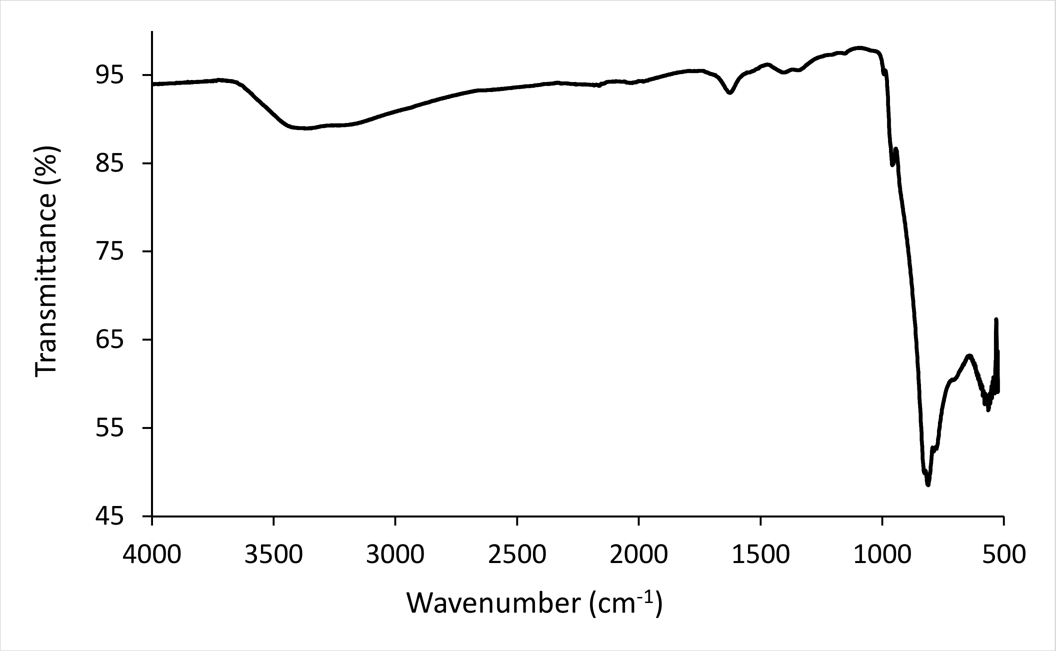

Figure 3-21. Infrared spectrum of the solid product from 2:1 Fe:Mo reaction in acetate buffer.

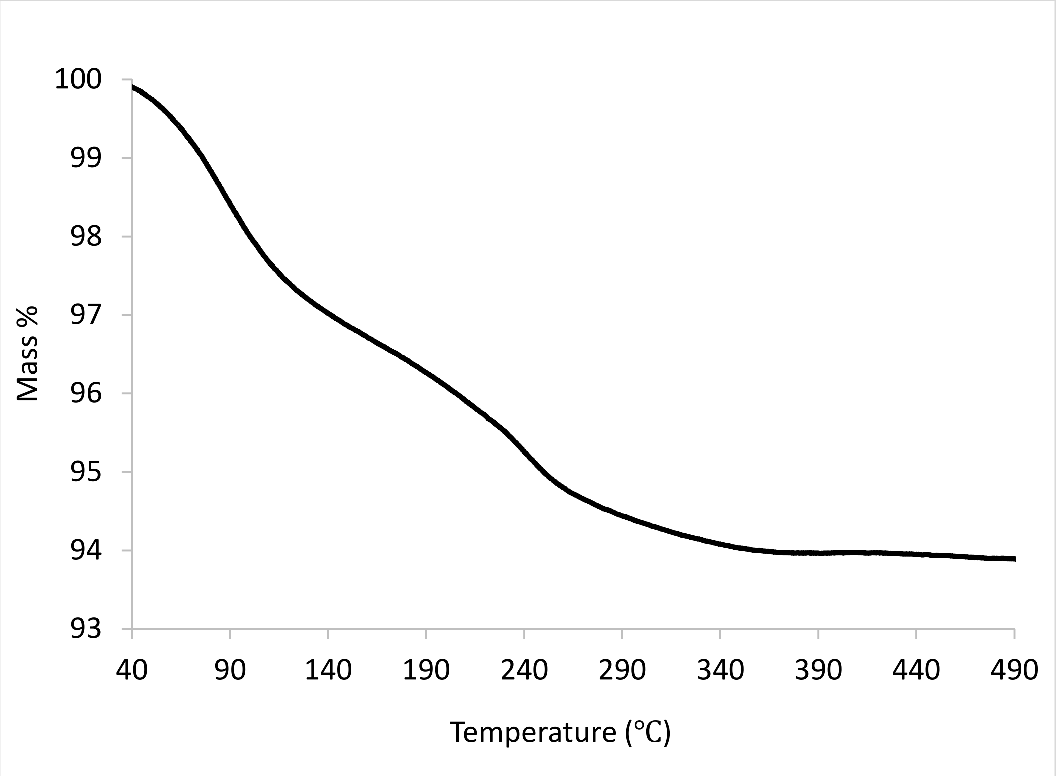

Figure 3-22 TGA trace of the solid product from 2:1 Fe:Mo reaction in acetate buffer.

The XRD pattern of the isolated product is shown in Figure 3-23. It appears that the material is mainly amorphous but there is a single sharp peak at 23.1° 2-Theta. It is uncertain what this is due to as no match was found in the ICDD database for it.

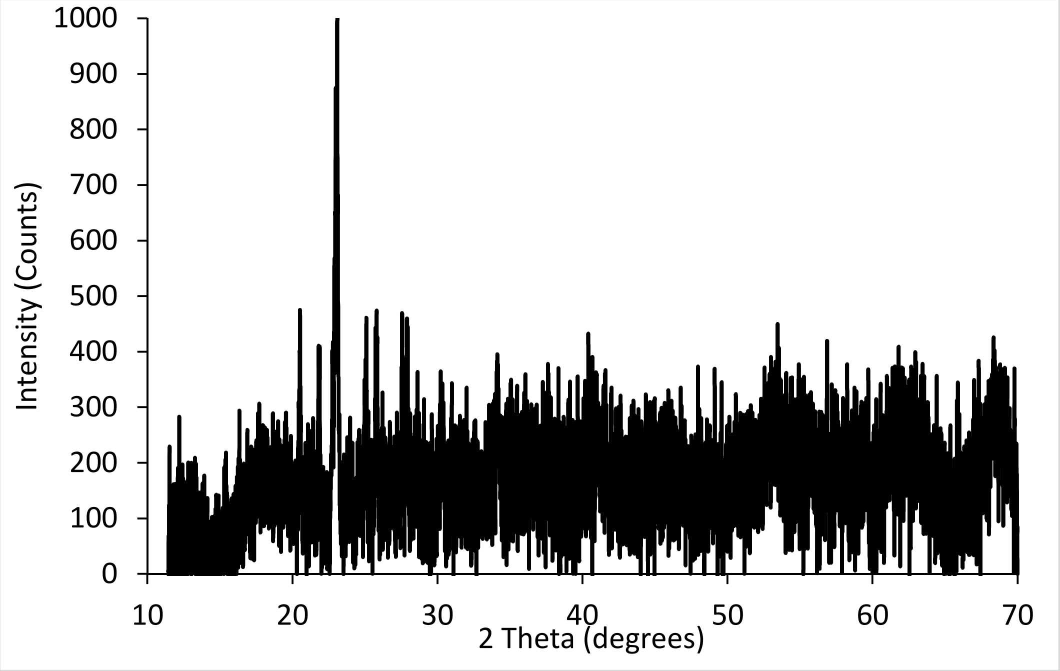

Figure 3-23. The X-ray powder diffraction pattern of the solid product from reaction of iron nitrate with MoO_3 with a 2:1 ratio in acetate buffer.

As shown in Figure 3-24 when the product was calcined at 670°C two phases were obtained: α-$Fe_2(MoO_4)_3$ and hematite (Fe_2O_3). Clearly, the 2:1 ferric nitrate to MoO_3 ratio exceeded that required for formation of pure α-$Fe_2(MoO_4)_3$ and it remains to test ratios between 1:1 and 2:1 to accomplish this. It can be surmised that the product isolated was a mixture of ferrihydrite and ferrimolybdite. Ferrihydrite is widely used in hydrometallurgical processes to remove Mo(VI) from waste acid and effluents via coprecipitation and/or adsorption.[168] The incorporation of molybdate into ferrihydrite produces ferrimolybdite when sufficient molybdate has been adsorbed. Thus, it is quite likely that the product isolated in this investigation is ferrihydrite containing non-stoichiometric amounts of molybdate. Therefore, when heated, phase separation occurs to produce α-$Fe_2(MoO_4)_3$ and hematite (Fe_2O_3). The Fe_2O_3 content was estimated to be 39% by weight using peak intensities.

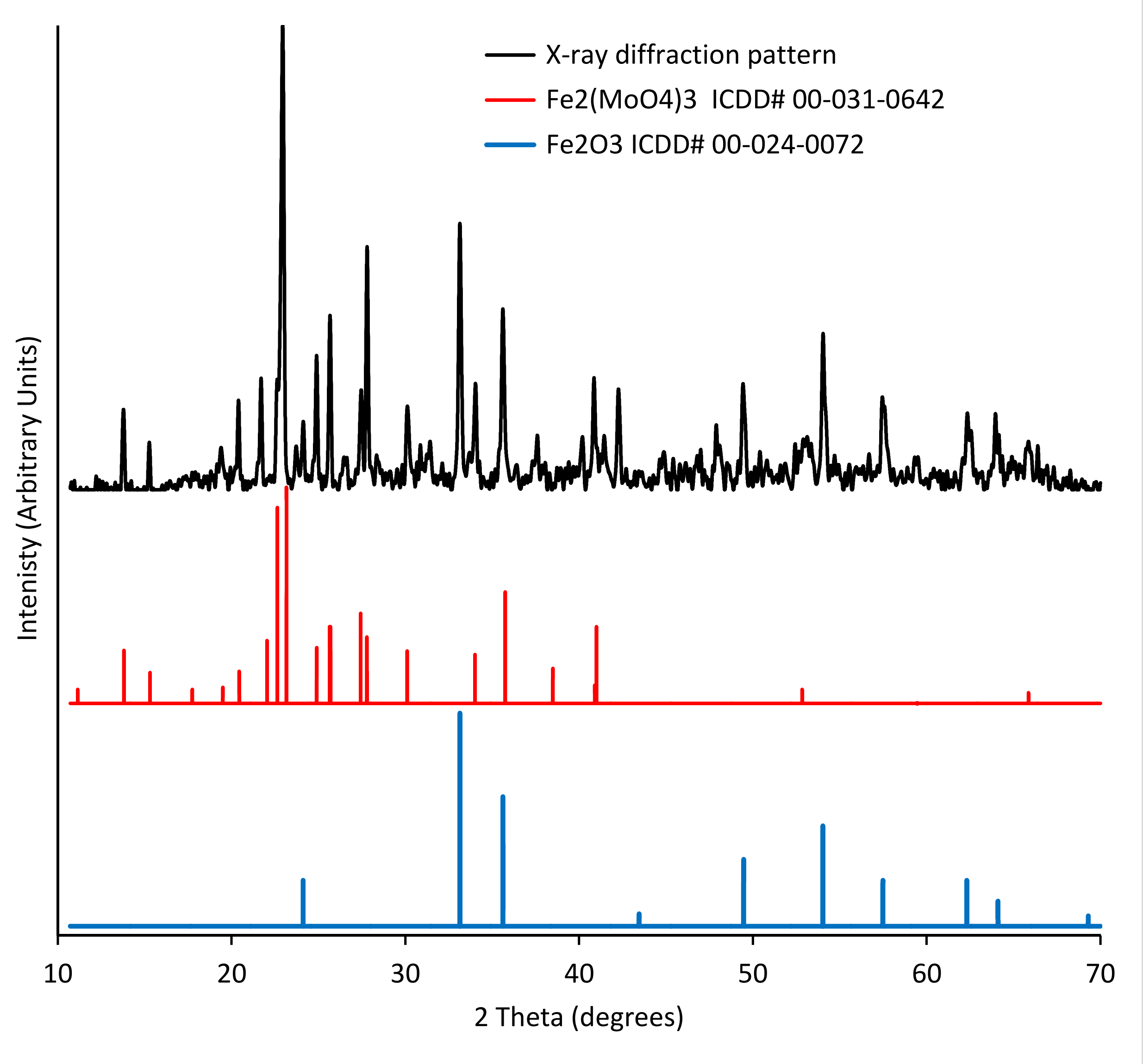

Figure 3-24. XRD pattern from reaction of iron nitrate with MoO_3 with a 2:1 ratio in acetate buffer.

The product produced using three molar equivalents of iron nitrate per molybdenum trioxide did not form a new phase. Instead, the reaction proceeded similar to the 2:1 reaction producing an amorphous molybdate-containing ferrite that when calcined at 670˚C produced a mixture of hematite and α-$Fe_2(MoO_4)_3$. The XRD pattern of the calcined product (Figure 3-25) had much more prominent peaks for Fe_2O_3 than the 2:1 product. The Fe_2O_3 content was estimated to be 55 % by weight using peak intensities.

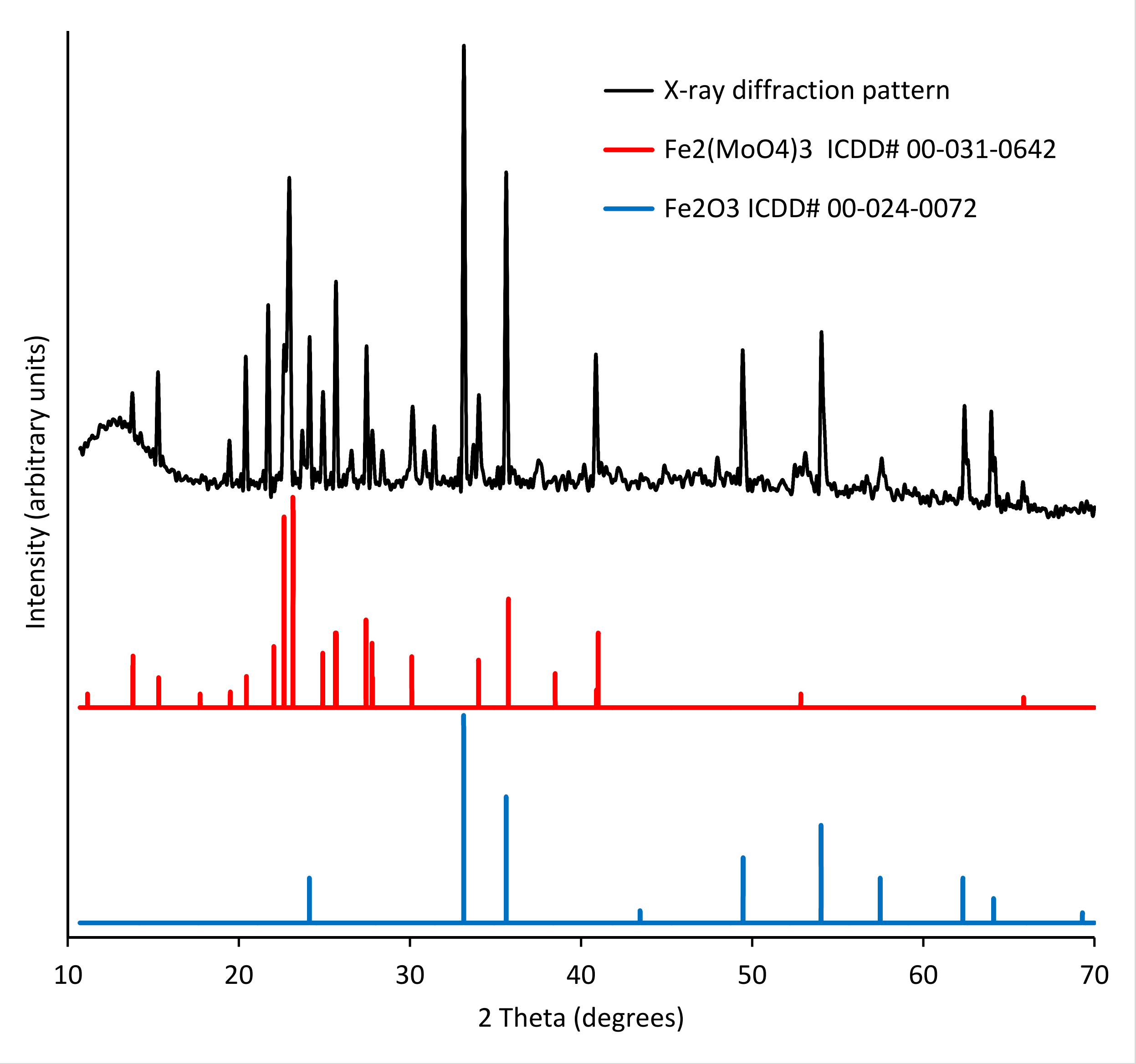

Figure 3-25. XRD pattern from reaction of iron nitrate with MoO_3 with a 3:1 ratio in acetate buffer.

Conclusions

The use of a sodium acetate/acetic acid buffer as the means to circumvent the unavailability of monomeric iron(III) acetate for the MO_x/Acetate process is effective in producing iron molybdenum oxides but the results are different from the conventional process. At the outset, it was thought that the reaction of iron nitrate with molybdenum trioxide in acetic acid buffer would behave similar to the reaction of the smaller radius lanthanide acetates with MoO_3. For example, this reaction using gadolinium acetate produced hydrated $Gd(MoO_4)OH$ that converted to $Gd_2Mo_2O_9$ upon heating.[169] The corresponding iron compound, $Fe_2Mo_2O_9$, is unknown but it may be possible to produce it as a metastable phase at low temperature. However, rather than forming molybdate/hydroxide phases, the reaction in buffer produced a variety of iron molybdate hydrate products that strongly depended on the reaction stoichiometry.

In a very surprising and extremely useful result, the reaction of iron nitrate with two molar equivalents of molybdenum trioxide produced a crystalline compound with the formula $NaFe_2(MoO_4)_2 \cdot 2H_2O$ that dehydrated to the battery anode material, $NaFe_2Mo_2O_9$. Thus, a procedure was developed for the facile, easily scaled synthesis of this useful material for fabrication of rechargeable lithium and sodium ion batteries. In the future, it would be interesting to produce the lithium analog by use of a lithium acetate/acetic acid buffer. Further, the iron to molybdenum ratio could be varied to produce other potential battery materials such as $Na_3Fe(MoO_4)_3$.

Unfortunately, when higher ratios of iron nitrate to molybdenum trioxide are reacted, amorphous or poorly crystalline materials are produced. This makes the product obtained extremely dependent on the Fe:Mo ratio so that isolation of a particular phase, e.g.

$Fe_2(MoO_4)_3 \cdot nH_2O$ becomes a matter of trial and error. Finding the correct stoichiometry is further complicated by the fact that the supernatant solution contains some of the iron and perhaps some molybdenum. It was established that the ratio to produce $Fe_2(MoO_4)_3 \cdot nH_2O$ lies between one and two molar equivalents of iron nitrate per molybdenum trioxide but the critical experiments to narrow this down to the correct ratio have not been performed. This will be addressed in future research. The 1:1 ratio reaction produced a mixture of $NaFe_2Mo_2O_9$ and $Fe_2(MoO_4)_3$ after calcination while the 2:1 and 3:1 reactions produced $Fe_2(MoO_4)_3$ and Fe_2O_3. Notably, the uncalcined product from the 1:1 reaction appears to contain amorphous ferrimolybdite, $Fe_2(MoO_4)_3(OH_2)_{5.6}$, in addition to $NaFe_2(MoO_4)_2 \cdot 2H_2O$.

The isolated uncalcined products from the reaction of molybdenum trioxide with two molar equivalents of iron nitrate in acetate buffer possess features that suggest they are ferrihydrite with incorporated molybdate groups. The iron to molybdenum ratio is above that required for $Fe_2(MoO_4)_3$. Thus, when they are calcined at 670°C, they produce a mixture of $Fe_2(MoO_4)_3$ and hematite (Fe_2O_3) in keeping with the fact that $Fe_2(MoO_4)_3$ is the only stable phase iron(III) iron molybdenum oxide. The amount of hematite can be increased by increasing the ratio of iron to molybdenum. It is expected that the products of these reactions could be promising catalysts since $Fe_2(MoO_4)_3$ supported on hematite is an excellent catalyst for oxidizing methanol to formaldehyde.[170]

The nature of the materials present in the supernatant solution of the reactions remains to be determined. These may include iron Keggin ions with FeO_4 or MoO_4 tetrahedral cores. Future research could characterize what is present in solution and attempt to isolate crystalline compounds using large no-coordinating organic cations or anions if necessary. Also, hydrothermal reactions could be used to possibly produce crystals of the reaction products suitable for crystallography.

While the formation of $NaFe_2(MoO_4)_2 \cdot 2H_2O$ was a serendipitous discovery, the results suggests that the MO_x/acetate process might benefit from a different buffer cation. Thus, sodium acetate could be replaced by ammonium acetate, tetramethylammonium acetate, tetrabutylammonium acetate, or triethylammonium acetate (among others). Further, variation of initial pH may influence the pathway of the reactions and the products produced.

CHAPTER IV

NOVEL EXTRACTION PROCESS FOR IRON ORE AND SYNTHESIS OF IRON NICKEL OXIDE

Introduction

According to the United States Geological Survey, the world's iron ore reserves are estimated to be at 170 billion tons, or 83 billion tons of metallic iron that may be extracted. The majority of this iron ore is split between Australia (29.4%), Russia (14.7%), Brazil (13.5%), and China (13.5%). (12.4 %)[171]. It was revealed that chemical agents frequently employed to create chelated iron for agricultural application can effectively extract iron from ores. Iron can be chelated with ligands such as ethylenediaminetetraacetic acid (EDTA), diethylenetriaminepentaacetic acid (DTPA), and ethylenediaminediaminedi-o-hydroxyphenylacetic acid (EDDHA), and ethylene glycol-bis(β-aminoethyl ether)-N,N,N′,N′-tetraacetic acid (EGTA) which is also known as egtazic acid[172], and notably iron-chelated can be usually used for fertilizer.[173] The chelating agents' job is to keep the iron soluble in water and so available to plants. Although both EDTA and DTPA were successful in extracting iron ore, EDTA's unique features make it the more practical extraction agent. Iron ore is beneficiated all over the world to suit the iron and steel industries' raw material needs. Because iron ore has its own unique mineralogical features, adjusting the metallurgical treatment and specific beneficiation method used at any given location is required for optimal product extraction. The type of beneficiation technology to use is determined by the gangue's nature and its relationship to the ore structure[174].

In this chapter, the Great Western Iron Ore or so-called GWIO will be studied. Firstly, iron extraction will be extracted from pure iron oxide (Fe_2O_3) by Ethylenediaminetetraacetic acid (H_4EDTA) and then with extraction iron from Great Western Iron Ore. Ethylenediaminetetraacetic acid (Figure 3.1) is world-wide used and it is a tetravalent molecule that is capable of forming a stable complex with divalent ions, trivalent ions , and so forth. It has a low solubility in water (0.50g/100 ml) and that makes its recovery from extraction processes easy. Finally, This will cover kinetics of the reaction from extracting iron from iron oxide and GWIO. Also, determination of the effect of the particle size on extraction process from ore will be studied as well as the acidity effect during the reaction of iron ore with Ethylenediaminetetraacetic acid (EDTA). At the end, synthesis of iron nickel oxide $NiFe_2O_4$ will also investigated.

Experimental

Reaction of iron oxide Fe_2O_3 with ethylenediaminetetraacetic acid (H_4EDTA)

The reaction was firstly performed with pure iron oxide (Fe_2O_3) with ethylenediaminetetraacetic acid (H_4EDTA). For further investigation, the reaction were studied to determine the suitable molar ratio for extracting iron from Great Western Ore. Iron oxide (Fe_2O_3) was purchased from Alfa Aesar. All organic and inorganic reagents commercially available were used without further purification. Note, four hydrogens are deliberately written before the acronym of ethylenediaminetetraacetic acid (H_4EDTA) to describe where the active functional groups dissociate in the chelating agent during the reaction (Figure 3-1).

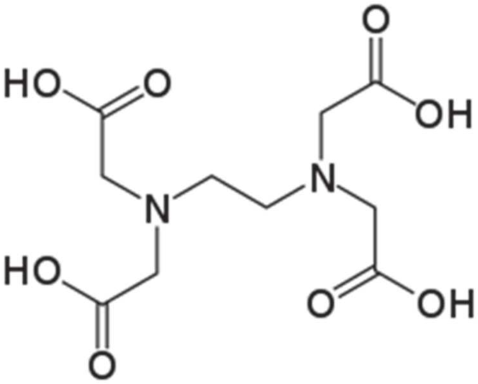

Figure 4-1. The chemical structure of ethylenediaminetetraacetic acid (H_4EDTA)

Fe_2O_3 (1.594 g, 0.01 mmol) was reacted with ethylenediaminetetraacetic acid (5.853 g, 0.02 mmol) in 100 ml of distilled water. Reaction was performed in refluxing water. In the meanwhile, samples were collected with time for hours . After that, samples were diluted and analyzed for iron by Microwave plasma atomic emission spectroscopy MP-AES (Figure 4-1).

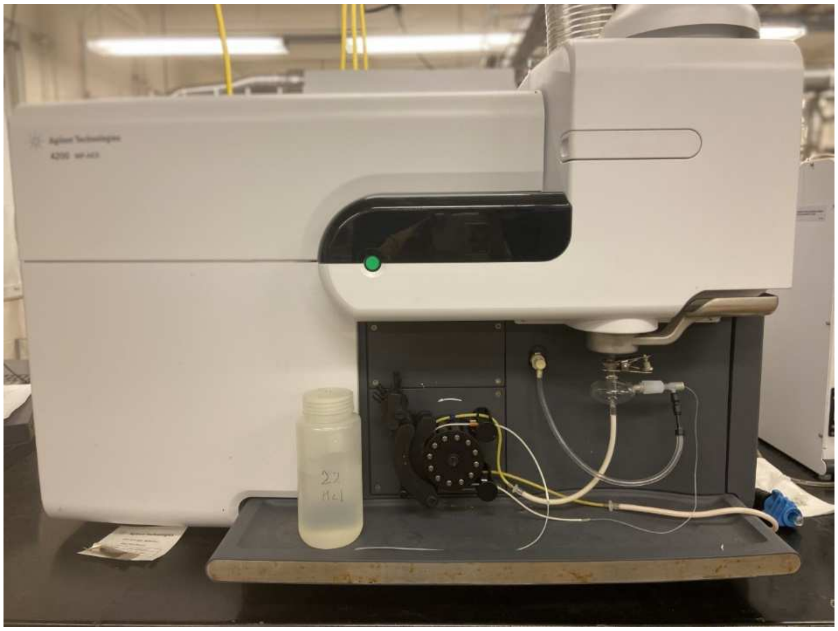

Figure 4-2 Instrument Of Microwave Plasma Atomic Emission Spectroscopy MP-AES

Result and discussion

Reaction of iron oxide Fe_2O_3 with ethylenediaminetetraacetic acid (H_4EDTA)

Reaction was performed in refluxing water and samples were collected with time and analyzed for iron contents by microwave plasma atomic emission spectroscopy MP-AES (Table 4-1). Consequently, microwave plasma-atomic emission spectroscopy (MP-AES) was used in order to follow the change of the concentration of Iron as oxide (Fe_2O_3) and reacted with ethylenediaminetetraacetic acid (H_4EDTA). As described above, reaction of Fe_2O_3 (1.594 g, 0.01 mmol) was not dissolved in 100 ml of distilled water because it is insoluble in water but it then dissolved well after adding a chelating agent of ethylenediaminetetraacetic acid (H_4EDTA) (5.853 g, 0.02 mmol) under reflux. After that, strongly dark brown reddish color was observed and took place after one hour of the reaction. Next, clear red solution was taken place after four hours. Seemingly, the reaction approach to the completion as iron complex with (H-EDTA-Fe) formed at certain time; three protons was possibly deprotonated in order to coordinate with iron Fe^{3+} with one proton left (scheme 1).[175-176] According to the microwave plasma-atomic emission spectroscopy (MP-AES), iron complex started extracting shortly when 7892 ppm of extracted iron was observed while at zero time, no concentration of iron was recorded (Table 4-1). Moreover, since an excess of iron was extracted, the reaction ended when the concentration of iron had almost remained the same after three hours (Figure 4-3).

Table 4-1. Concentration of Iron (ppm) Versus Time for a 4-hour reaction

Time (hours)	[Fe](ppm)
0.0	0.000
1.0	7892
1.5	8634
2.0	8791
3.0	9319
4.0	9145

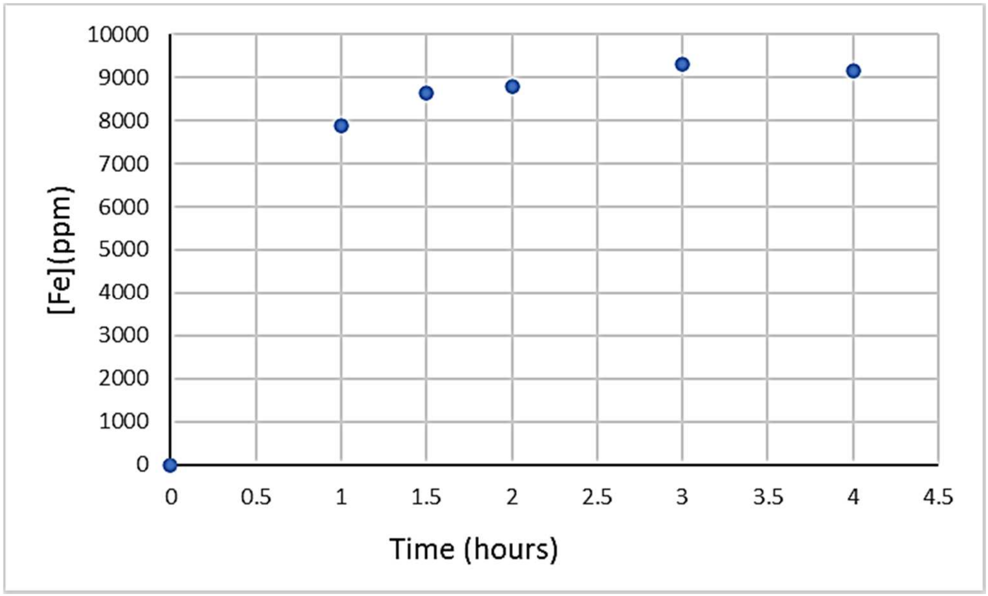

Figure 4-3. Concentration of Iron (ppm) Versus Time for a 4-hour reaction

$$Fe_2O_{3\,(aq)} + 2\ H_4EDTA_{(s)} \longrightarrow 2\ Fe(HEDTA)_{(aq)} + 3H_2O_{(l)}$$

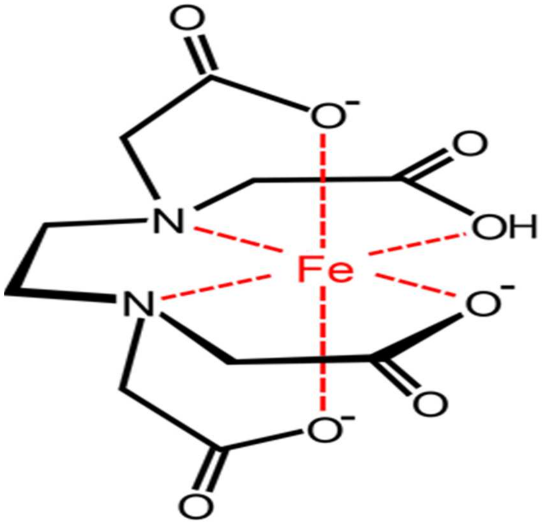

Scheme 1. Aqueous iron complex reaction of iron oxide Fe_2O_3 with ethylenediaminetetraacetic acid (H_4EDTA)

Experimental

Reaction of extracting iron from coarse ore by ethylenediaminetetraacetic acid (H_4EDTA) at three different periods

Reaction of coarse ore with H_4EDTA (11.783 g, 0.04 mmol) was taken place in refluxing water for 48 hours . The extracting process of the reaction was run approximately with 2 molar equivalents of H_4EDTA per mole of Fe_2O_3 (3.1913 g, 0.02 mmol, 200 ml). The stoichiometry of the reaction was based on the previous reaction of the pure iron oxide (Fe_2O_3) with ethylenediaminetetraacetic acid (H_4EDTA). Similarly, reaction of 2 molar equivalents of H_4EDTA (11.764 g, 0.04 mmol) with coarse ore (3.086 g, 0.02 mmol) (approximately 2 molar equivalents of Fe Figure 4-4) in refluxing water for 24 hours as well as another reaction was performed likely

2 molar equivalents of H_4EDTA (11.726 g, 0.04 mmol) with coarse ore (3.182 g, 0.02 mmol) with longer time to investigate and assure the completion of the reaction for 96 hours.

Figure 4-4. Coarse Sample From A Great Western Ore

Result and discussion

Reaction of extracting iron from coarse ore by ethylenediaminetetraacetic acid (H_4EDTA) at three different periods

While collecting samples with every 12 hours during running reaction, no color change of the samples were observed. Therefore, the concentration of iron was zero concentration at beginning of reaction. Later, the reaction dramatically changed with yellow color after 37 hours recording high concentration of extracted iron at 6267 ppm (Figure 4-6). The concentration of the iron was finally measured to be 6847 ppm of iron extraction after 48 hours (table 4-2).

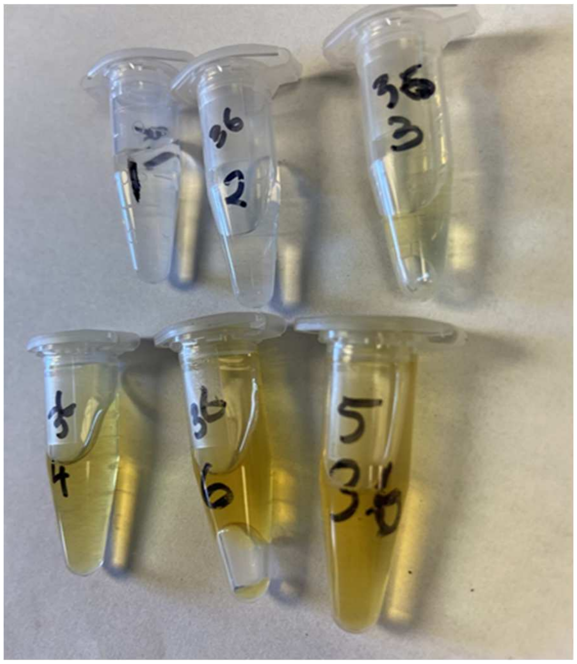

Figure 4-5 collected samples from reaction of extracting iron from coarse ore by ethylenediaminetetraacetic acid (H_4EDTA) for a 48-hour reaction

Interestingly, this could be an indicator that the reaction is behaving as a self-catalysed reaction. Notably, the graph of concentration of iron against its extraction process showed an induction period which could be another indicator of being a self- catalysed reaction.

Table 4-2. Concentration of extracted Iron (ppm) from coarse ore Versus Time for a 48-hour reaction

Time (hours)	[Fe](ppm)
0.0	0.000
0.5	1.020
13	5.490
24	401.7
37	6267
48	6847

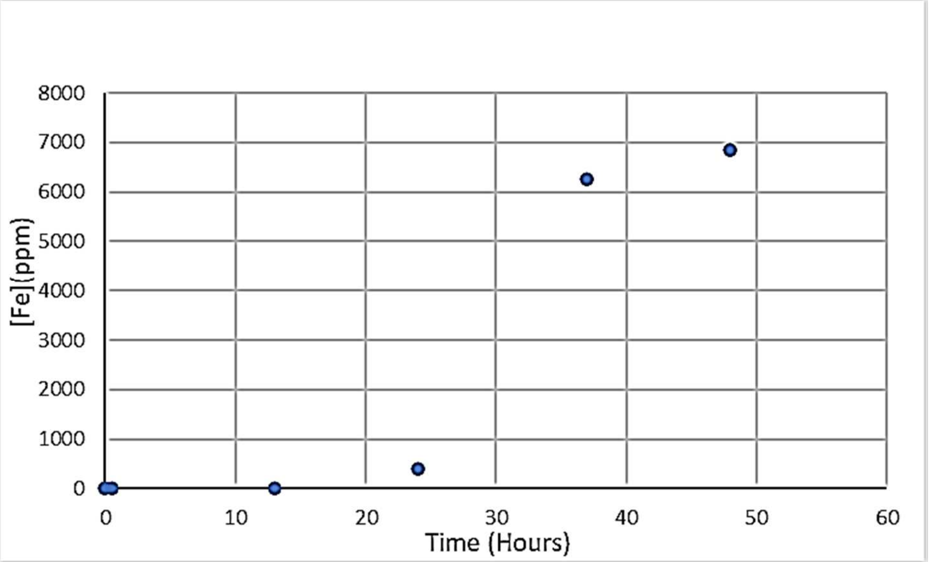

Figure 4-6 Concentration of Iron Versus Time During the Time of Extraction process of 48-hour reaction

Moreover**,** the reaction was performed similarly but with longer time for 96 hours in order to know the equilibrium plateau. Therefore, microwave plasma-atomic emission spectroscopy (MP-AES) was also used to follow the change of the concentration of iron as Fe_2O_3 reacted and chelated by ethylenediaminetetraacetic acid (H_4EDTA). This gave the data tabulated in (Table 4-3) and shown graphically in (Figure 4-7). Interestingly, the reaction reached completion in the first day of the reaction. Since a one-fold excess of iron oxide was chelated, the reaction ended when the concentration of iron had increased 80 %. This approaches to have occurred at some point in the first 30 hours. Experimentally, the reaction had reached its completion at certain point in the first 24 hours and 6803 ppm of iron concentration after 24.5 hours; this data was quite similar to those long-period reactions. Furthermore, the color was interestingly changing with every time collecting samples from clear and pale yellow color to dark yellow along with time Figure 4-9, this proves the reaction to be ended with short-run of time (Figure 4-8).

Table 4-3 Concentration of extracted Iron (ppm) from coarse ore Versus Time for a 96-hour reaction

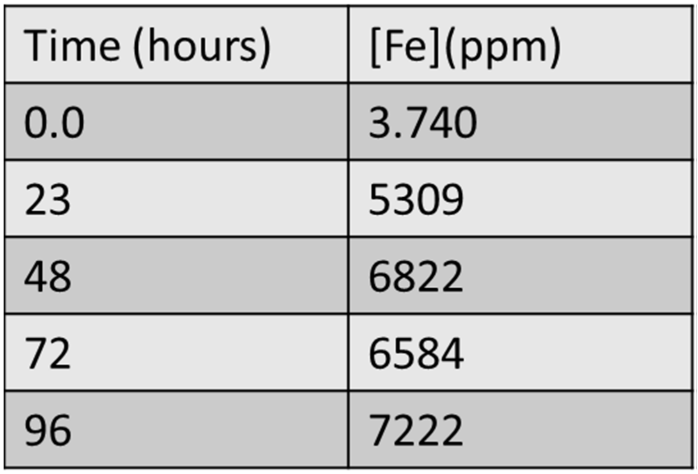

Time (hours)	[Fe](ppm)
0.0	3.740
23	5309
48	6822
72	6584
96	7222

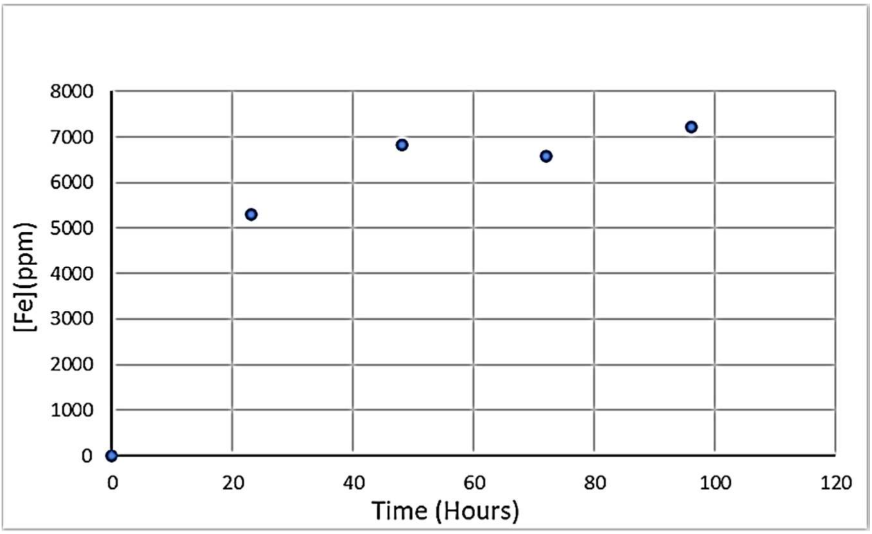

Figure 4-7 Concentration of Iron Versus Time During the Time of Extraction process of 96-hour reaction

Table 4-4 Concentration of extracted Iron (ppm) from coarse ore Versus Time for a 24-hour reaction

Time (hours)	[Fe](ppm)
0.00	0.000
1.00	158.0
1.50	369.0
4.50	2883
5.90	4791
8.30	5599
18.3	6715
24.5	6803

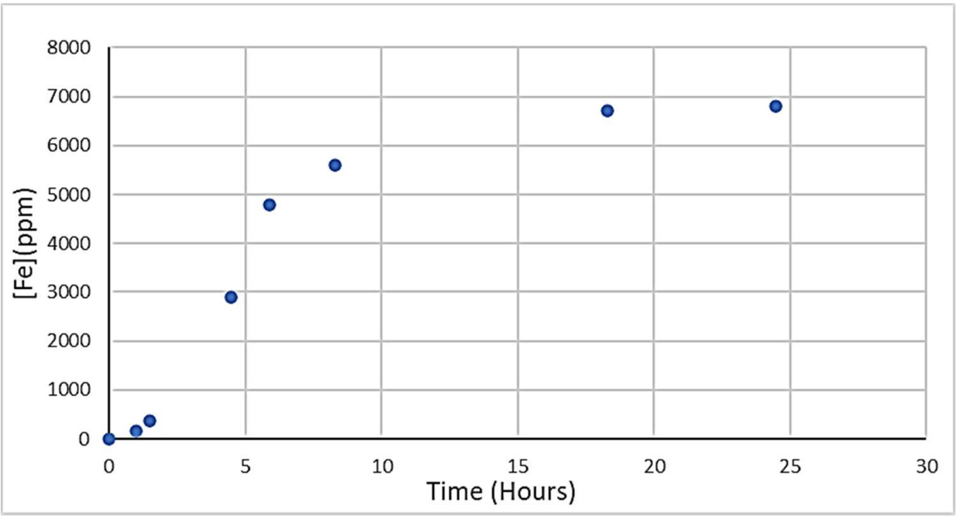

Figure 4-8 Concentration of Iron Versus Time During the Time of Extraction process of 24-hour reaction

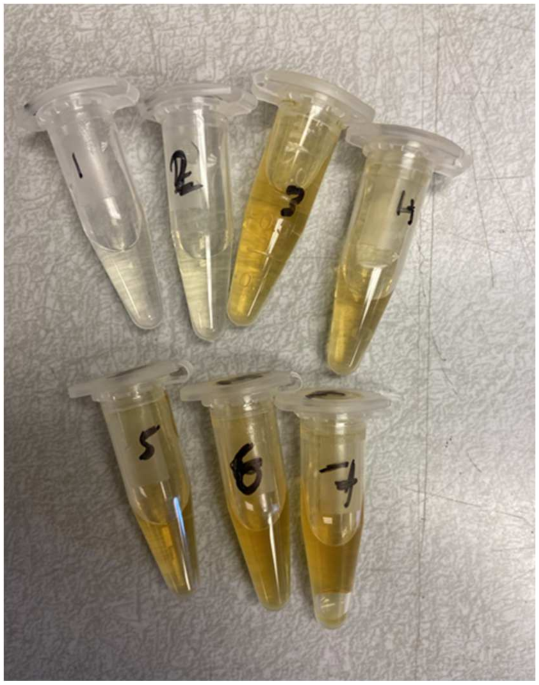

Figure 4-9 collected samples from reaction of extracting iron from coarse ore by ethylenediaminetetraacetic acid (H4EDTA) for a 24.5-hour reaction

Experiment of iron precipitation reaction from ore

When a mixture of EDTA (11.705 g) and great Western Iron ore (3.178 g) was heated to reflux in 200 ml of water a slow reaction took place over 12 hours with a small amount of iron dissolving. After a sufficient amount of iron dissolved a rapid reaction occurred causing the dark reddish color of the ore to completely disappear to yield an pale reddish solution and a pinkish solid. After that, the reaction mixture was cooled at room temperature and then filtered to remove the extraction residue. Next, The reddish orangish filtrate was treated with a solution of potassium hydroxide (9.771 g) in 42 ml of distilled water. This reaction caused the iron to precipitate slowly as iron hydroxide Figure 4-10. The precipitation reaction was allowed to continue for 22 hours. The precipitate was separated by centrifugation, washed with distilled water several times, and dried in a vacuum drier for 48 hours. This produced dark brownish black pellets of iron hydroxide that break upon calcination to 800 ˚C as iron oxide Figure 4-11.

Figure 4-10 product of precipitation reaction as iron hydroxide

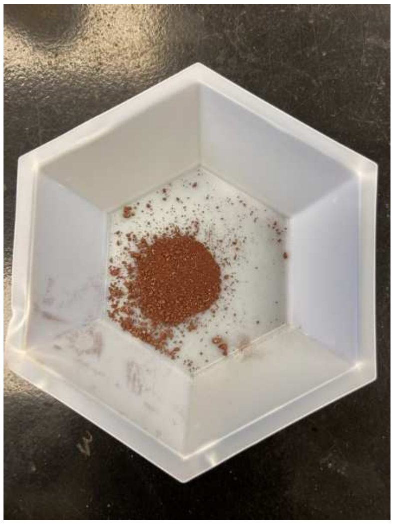

Figure 4-11 Ceramic product from iron precipitation reaction as iron oxide at 800 ˚C

The amount of iron hydroxide precipitated was 1.807 g and it was reduced and evolved to Hematite (Fe_2O_3) upon elevated calcination at 800 □ to be 0.473 g. This was confirmed by the XRD technique and showed almost identical large peaks of a hematite (Fe_2O_3) Figure 4-15. Notably, color of iron hydroxide occurred when calcinated from dark brownish black to red. Analytically, the infrared spectroscopy was run to analyze the O-H of H-bonded and Fe-O stretching modes before and after firing the precursor of precipitated iron hydroxide as well as the thermal gravimetric analysis (TGA) was also used to calculate the number of equivalent of hydroxide group Figure 4-14. The IR technique obviously show the hydroxide group vibration mood over the range from 3010 to 3663 cm^{-1} and iron oxide at the fingerprint region; the strong and intense band at 584 cm^{-1} is due to the stretching vibration of the Fe–O bond in iron oxide[177]. Moreover, there is a disappearance of O-H stretching group upon elevated temperature and that confirmed that the iron hydroxide was converted to a ceramic compound of iron oxide (Fe_2O_3) Figure 4-13. The weight loss of the dehydroxylation was 8.51 %. The equivalence of the hydroxide group was calculated based on the thermal gravimetric analysis (TGA) to be 8.96 Figure 4-14.

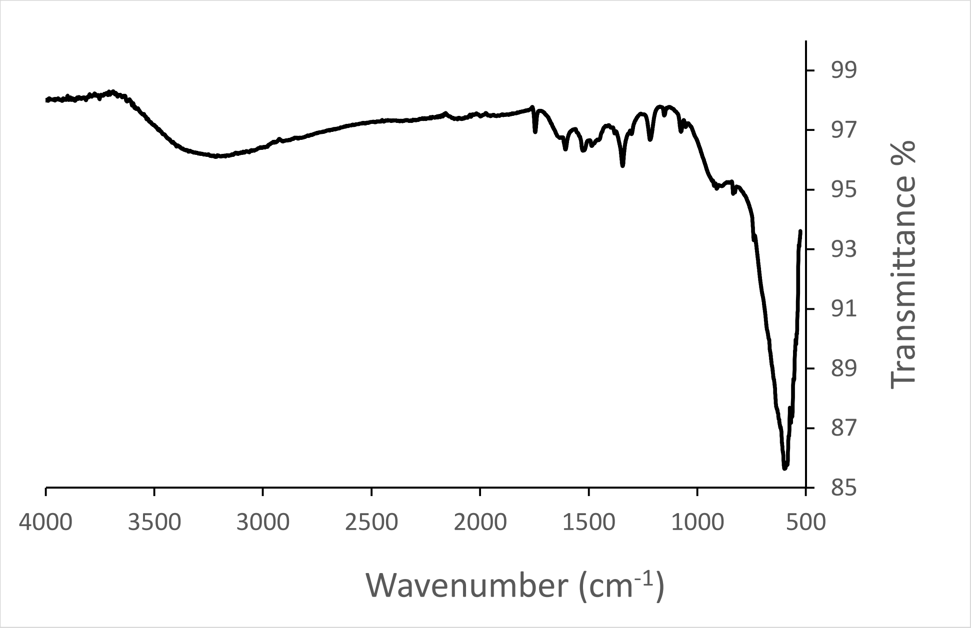

Figure 4-12 IR spectrum of precipitation reaction as iron hydroxide

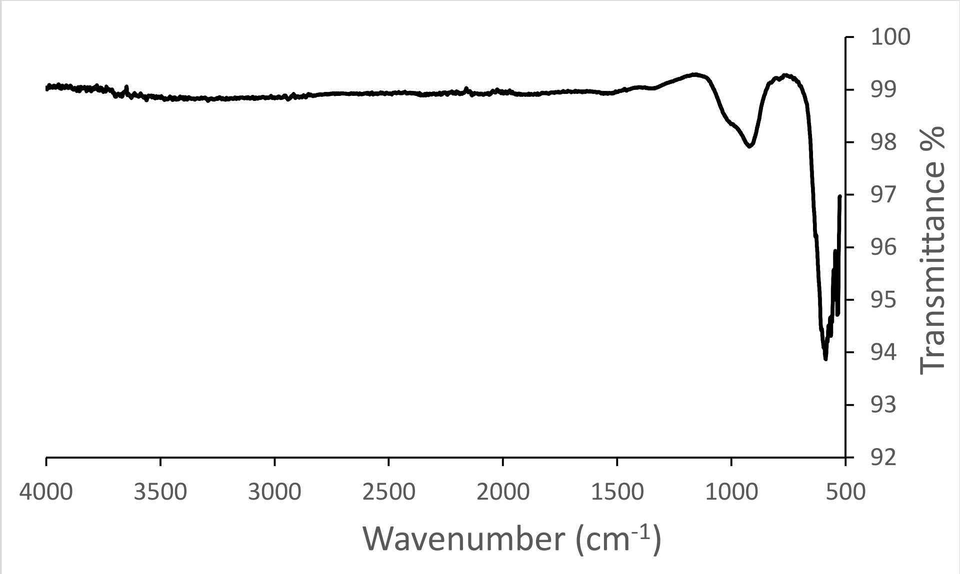

Figure 4-13 IR spectrum of iron oxide after calcinated iron hydroxide

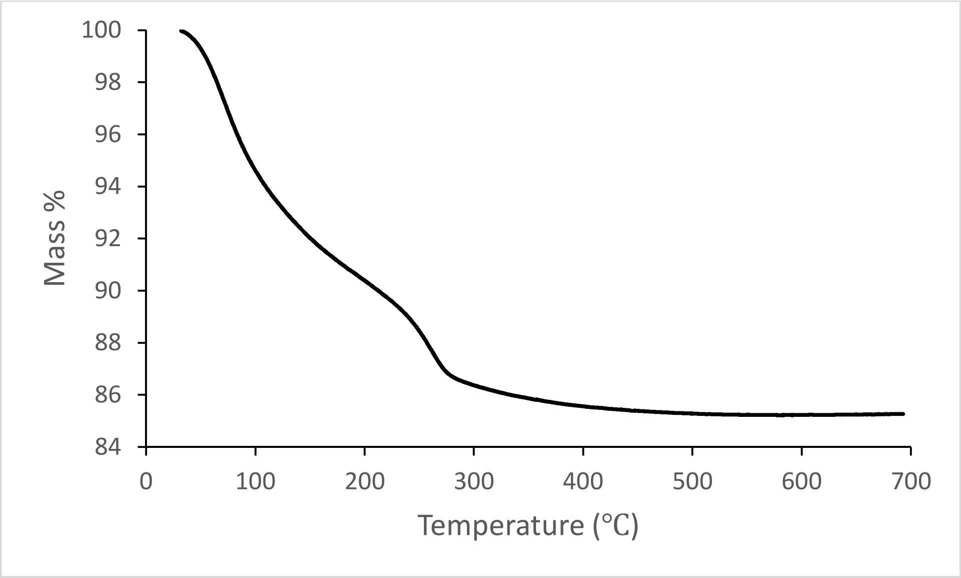

Figure 4-14 Thermal gravimetric analysis (TGA) of precipitation reaction as iron hydroxide

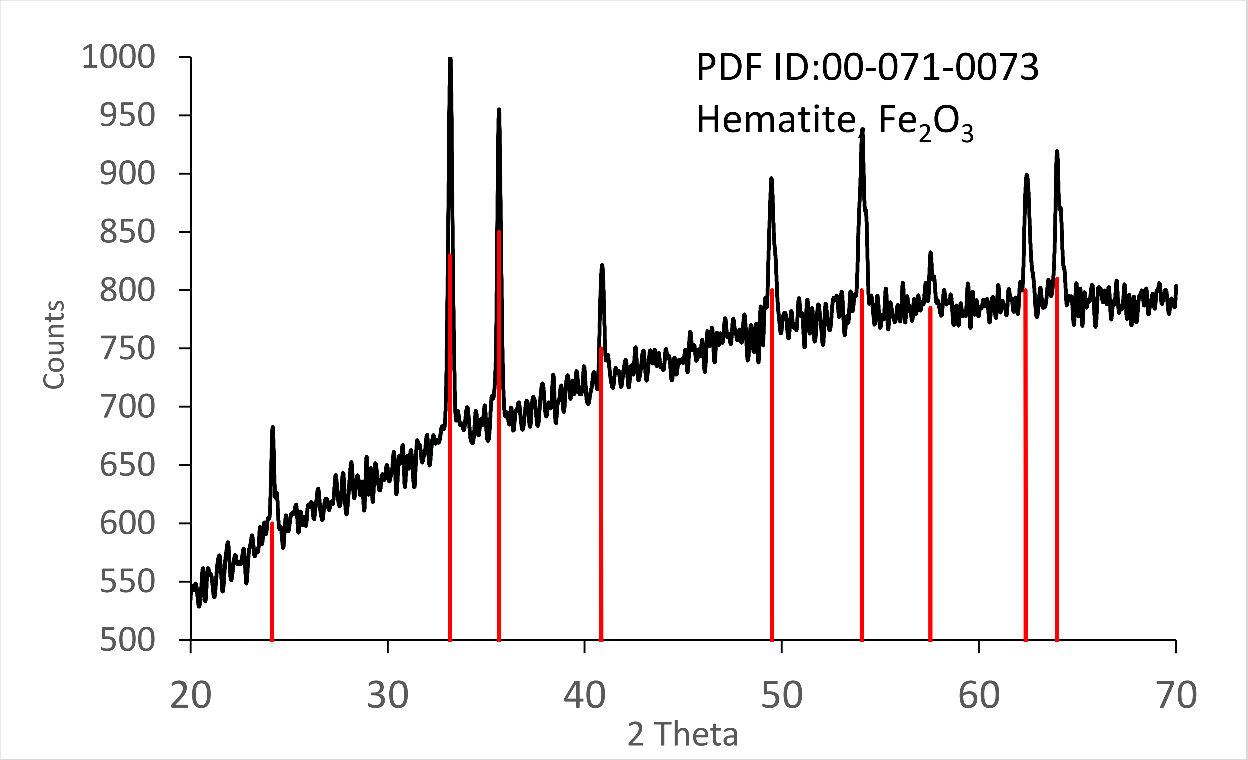

Figure 4-15 The XRD of the hematite from calcinating the iron hydroxide product.

Proof of Self-Catalysed Reaction

Experiment of Reaction of extracting iron from coarse ore by ethylenediaminetetraacetic acid (H_4EDTA) with Catalysis of Fe-EDTA-H

Reaction of coarse ore with H_4EDTA (11.726 g, 0.04 mmol) was performed in refluxing water. The extracting process of the reaction was run approximately with 2 molar equivalents of H_4EDTA per mole of Fe_2O_3 (3.182 g, 0.02 mmol, 200 ml). The stoichiometry of the reaction was running same as a regular reaction of iron extracting process for 118 hours. In order to test the hypothesis of self- catalysis claim, the pale red filtrate of Fe-EDTA-H complex was separated and contained in a bottle with 199 ml for further reaction after filtering off the extraction residue. Next, 10 %, 30 %, and 40 % of the filtrate (Fe-EDTA-H) were added to three different reactions and complete the volume of distilled water 180 ml, 140 ml, 120 ml respectively with same condition to be performed as a catalysis by accelerating the reaction. After that, samples were collected with every 24 hours. Finally, sample were diluted and measured by microwave plasma atomic emission spectroscopy MP-AES. Finally, all the data of three sets of the iron concentrations were plotted versus its certain time in order to be analyzed and interpreted.

Result and Discussion of Self-Catalysis Reaction

Experiment of Reaction of extracting iron from coarse ore by ethylenediaminetetraacetic acid (H_4EDTA) with Catalysis of Fe-EDTA-H

Microwave plasma-atomic emission spectroscopy (MP-AES) was analytically and quantitatively used to follow the change of the concentration of iron as iron oxide reacted with EDTA in presence of iron complex. So, addition of 10 %, 30%, and 40% (Fe-EDTA-H) by volume of a solution from a previous extraction solution were added to a new starting mixture. After that, all samples were diluted by 20 ml of distilled water in order to calculate concentrations of iron. The experiments were reported over an 118-hour period with sampling every 24 hours. These gave the data tabulated in (Table 4-5), (Table 4-6), and (Table 4-7) and shown graphically in (Figure 4-16), (Figure 4-17), and (Figure 4-18) respectively. Interestingly, induction period for reaction was eliminated and the reaction reached completion in the first 24 hours of the reaction in presence of the catalysis added of iron complex while the reaction took a little bit longer without adding the catalysis. However, the tabulated data at zero time clearly show that the more addition of iron complex from the previous reaction to the new mixture, the faster reaction and higher concentration of iron can be.

Table 4-5 Concentration of extracted Iron (ppm) from coarse ore Versus Time for a 118-hour reaction with 10 % addition of iron complex for long-run

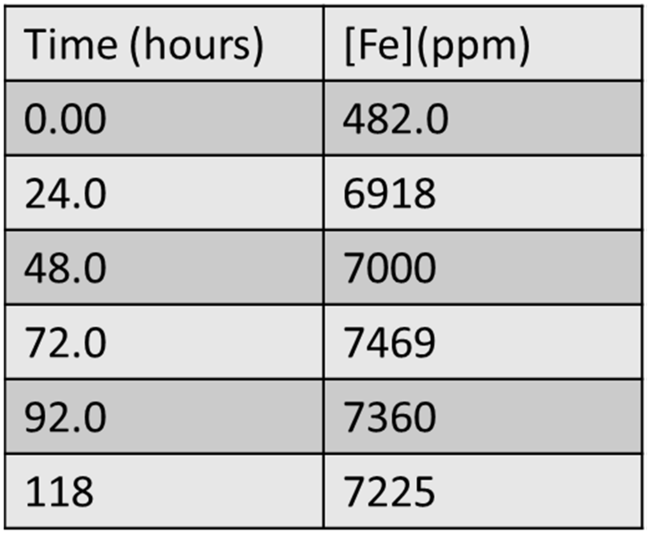

Time (hours)	[Fe](ppm)
0.00	482.0
24.0	6918
48.0	7000
72.0	7469
92.0	7360
118	7225

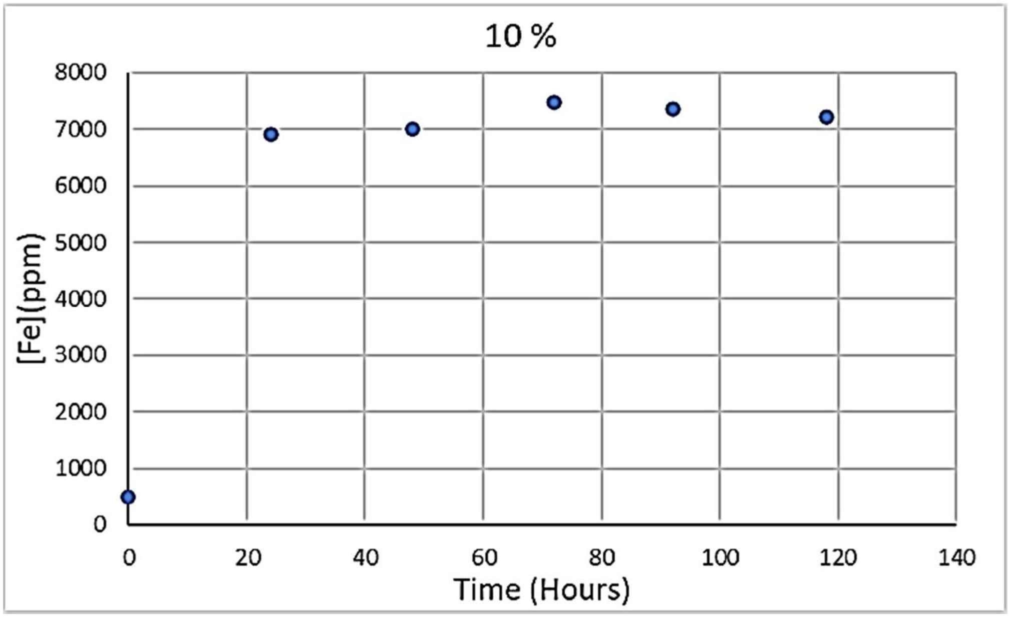

Figure 4-16 Concentration of extracted Iron (ppm) from coarse ore Versus Time for a 118-hour reaction with 10 % addition of iron complex

Table 4-6 Concentration of extracted Iron (ppm) from coarse ore Versus Time for a 118-hour reaction with 30 % addition of iron complex for long-run

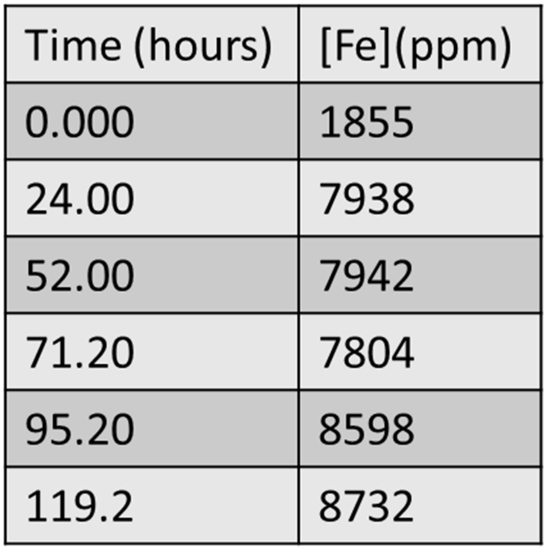

Time (hours)	[Fe](ppm)
0.000	1855
24.00	7938
52.00	7942
71.20	7804
95.20	8598
119.2	8732

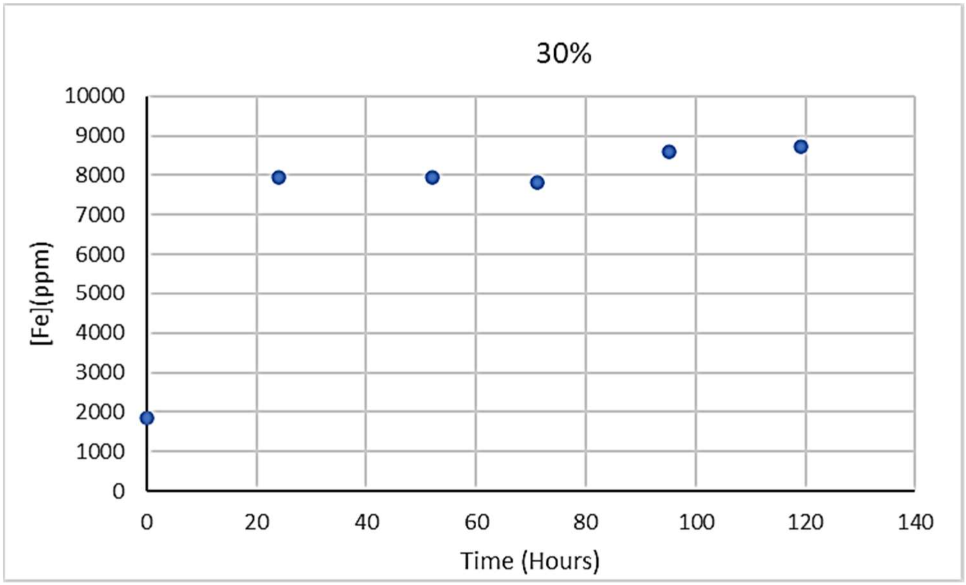

Figure 4-17 Concentration of extracted Iron (ppm) from coarse ore Versus Time for a 118-hour reaction with 30 % addition of iron complex

Table 4-7 Concentration of extracted Iron (ppm) from coarse ore Versus Time for a 118-hour reaction with 40 % addition of iron complex for long-run

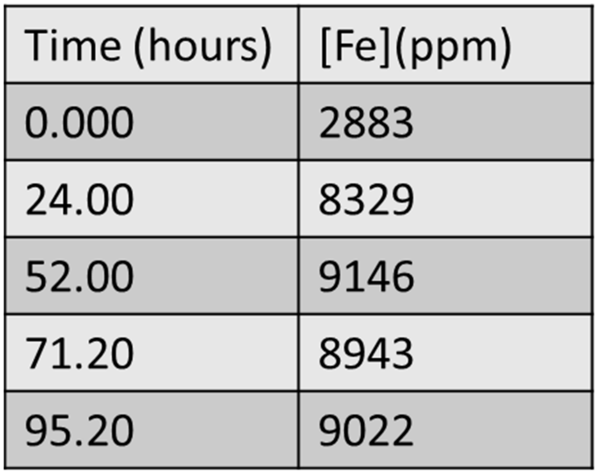

Time (hours)	[Fe](ppm)
0.000	2883
24.00	8329
52.00	9146
71.20	8943
95.20	9022

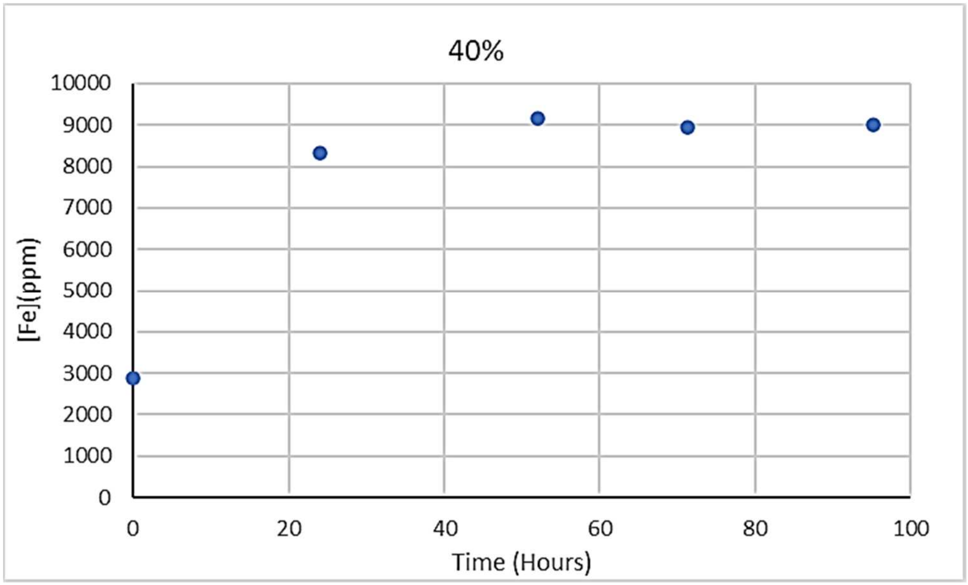

Figure 4-18 Concentration of extracted Iron (ppm) from coarse ore Versus Time for a 118-hour reaction with 40 % addition of iron complex

Furthermore, all reactions were repeated under same conditions but with short-period for four hours in order to calculate and show equation of rate reaction. While reacting, small amounts of samples were collected with every half an hour. Next, samples were then diluted with distilled water to be finally determined of iron contents by MP-AES. lastly, the results are tabulated in (Table 4-8), (Table 4-9), and (Table 4-10). According to data, the concentration of iron was doubled as the 30 % addition of iron complex were added, so it clearly show that the Initial rates increase as the initial concentration of Fe(HEDTA). From given data, order of reaction can be calculated to be first order reaction as followed equation:

$$\text{Rate} = k[\text{Fe-EDTA-H}]$$

Table 4-8 Concentration of extracted Iron (ppm) from coarse ore Versus Time with 10 % addition of iron complex for short-run

Time (hours)	[Fe](ppm)
0.0	5.100
0.5	7.190
1.0	10.99
1.5	14.60
2.0	18.27
2.5	22.90
3.0	27.33
3.5	35.33

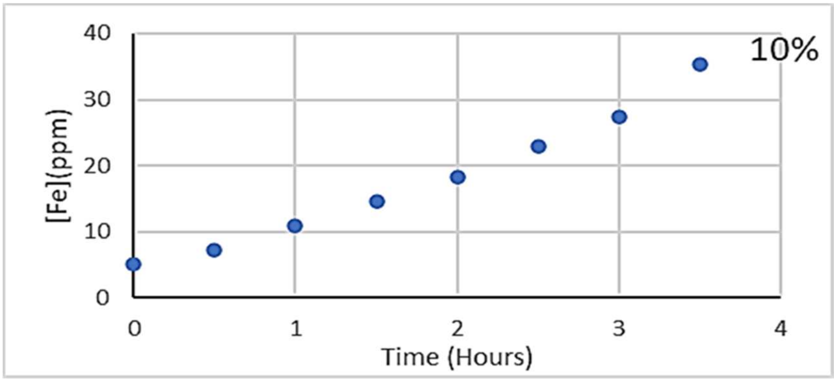

Figure 4-19 Concentration of extracted Iron (ppm) from coarse ore Versus Time for a 4-hour reaction with 10 % addition of iron complex

Table 4-9 Concentration of extracted Iron (ppm) from coarse ore Versus Time with 30 % addition of iron complex for short-run

Time (hours)	[Fe](ppm)
0.0	14.99
0.5	15.44
1.0	19.00
1.5	24.14
2.0	29.99
2.5	38.61
3.0	47.16
3.5	56.08

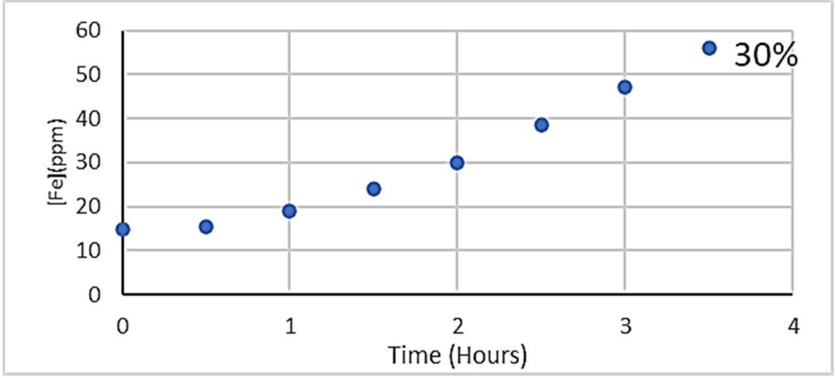

Figure 4-20 Concentration of extracted Iron (ppm) from coarse ore Versus Time for a 4-hour reaction with 30 % addition of iron complex

Table 4-10 Concentration of extracted Iron (ppm) from coarse ore Versus Time with 40 % addition of iron complex for short-run

Time (hours)	[Fe](ppm)
0.0	22.60
0.5	25.84
1.0	32.69
1.5	46.02
2.0	55.92
2.5	63.84
3.0	70.78
3.5	89.39

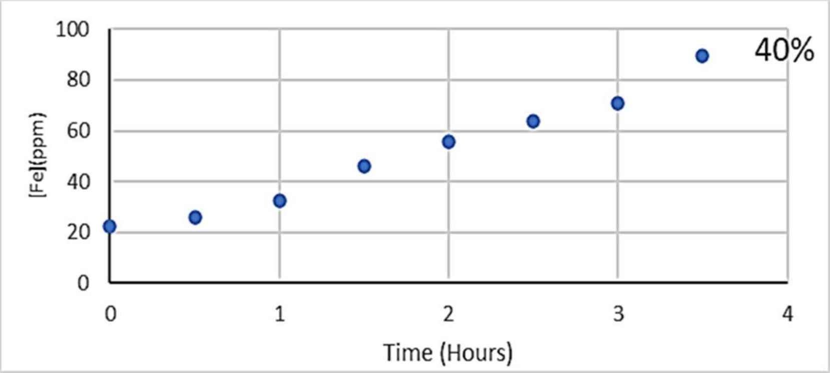

Figure 4-21 Concentration of extracted Iron (ppm) from coarse ore Versus Time for a 4-hour reaction with 40 % addition of iron complex

Also, the acidity of the reaction was studied to investigate changes in acidity as the reaction progresses. Thus, samples were collected while reacting 2 molar equivalents of H_4EDTA with one molar equivalent of Fe_2O_3 of coarse ore in refluxing water at 6 hours. According to data in (Figure 4-22) and (Table 4-11), reaction was fairly acidic at the very beginning of the performance with 2.85 based on pH meter at zero time. Also, there was a gradual decrease in acidity for the first two hours which may explain the presence of the induction period for reaction and elimination and therefore confirm the hypothesis of self-catalysis reaction. Acidity of the reaction vary over the range from 2.85 to 1.6 and that is due to the formation of iron complex and increasing (Fe-EDTA-H) in concentration by deprotonating and coordinating ethylenediaminetetraacetic acid to iron trivalent cation and coordinate through lone pair of electrons from nitrogen and ionic bonds from acetate. Possible Mechanism with FeHEDTA as an acidic catalyst is below:

$$6\ Fe(HEDTA)_{(aq} + Fe_2O_3 \longrightarrow 2\ Fe^{3+} + 6\ [Fe(EDTA)]^{-1}{}_{(aq)} + 3H_2O_{(l)}$$

$$6\ [Fe(EDTA)]^{-1}{}_{(aq)} + 2\ H_4EDTA_{(s)} \longrightarrow 6\ Fe(HEDTA)_{(aq)} + 2[HEDTA]^{3-}{}_{(aq)}$$

$$2\ Fe^{3+} + 2[HEDTA]^{3-} \longrightarrow 2\ Fe(HEDTA)_{(aq)}$$

Scheme 2. Possible Mechanism with FeHEDTA as an Acidic Catalyst:

Table 4-11 Changes in Acidity of extracting iron from coarse ore by ethylenediaminetetraacetic acid (H_4EDTA)

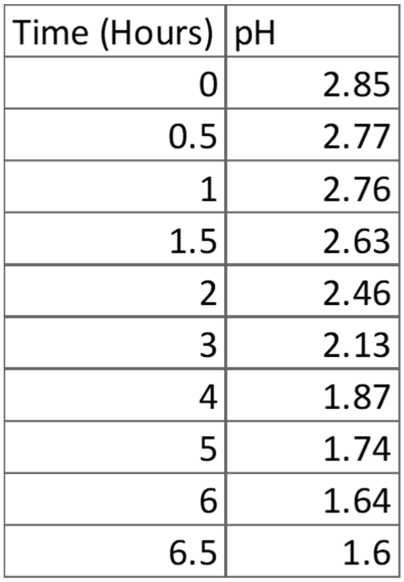

Time (Hours)	pH
0	2.85
0.5	2.77
1	2.76
1.5	2.63
2	2.46
3	2.13
4	1.87
5	1.74
6	1.64
6.5	1.6

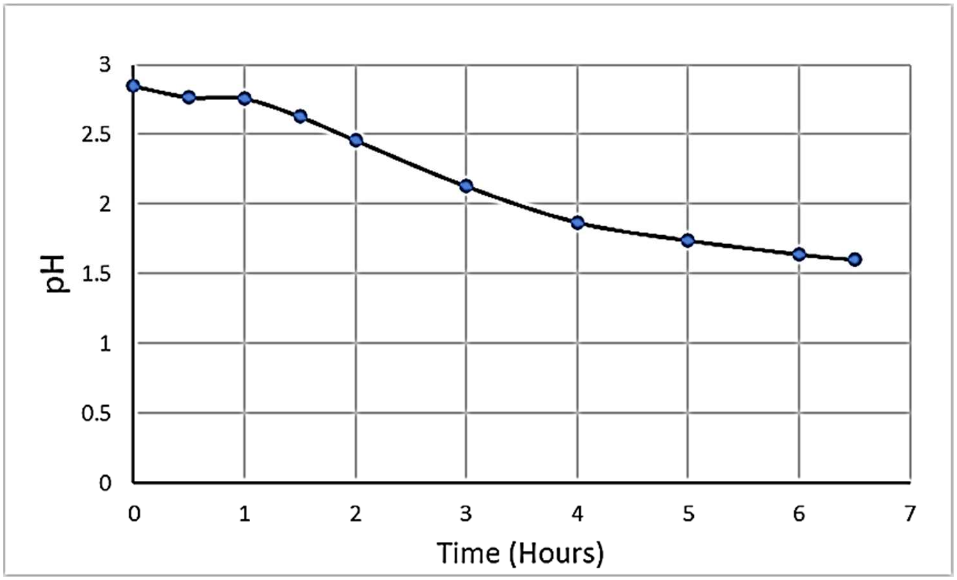

Figure 4-22 Changes in Acidity of extracting iron from coarse ore by ethylenediaminetetraacetic acid (H_4EDTA)

The particle size of the extremely fine ore (Figure 4-23) was studied to determine its effect on the reaction. So, the reaction of extracted iron from fine ore was performed by ethylenediaminetetraacetic acid (H_4EDTA) at similar conditions described earlier in this chapter. Samples were collected during the rection for six hours. Next, samples were diluted with distilled water to be quantitatively analyzed MP-AES. Remarkably, the color of the samples rapidly change with time and get more condense yellow due to the iron-chelated complex as shown below. The reaction is faster compared to coarse and give a linear plot as shown in Figure 4-24. In conclusion, the concentration of the iron extraction from different particle sizes is effective .

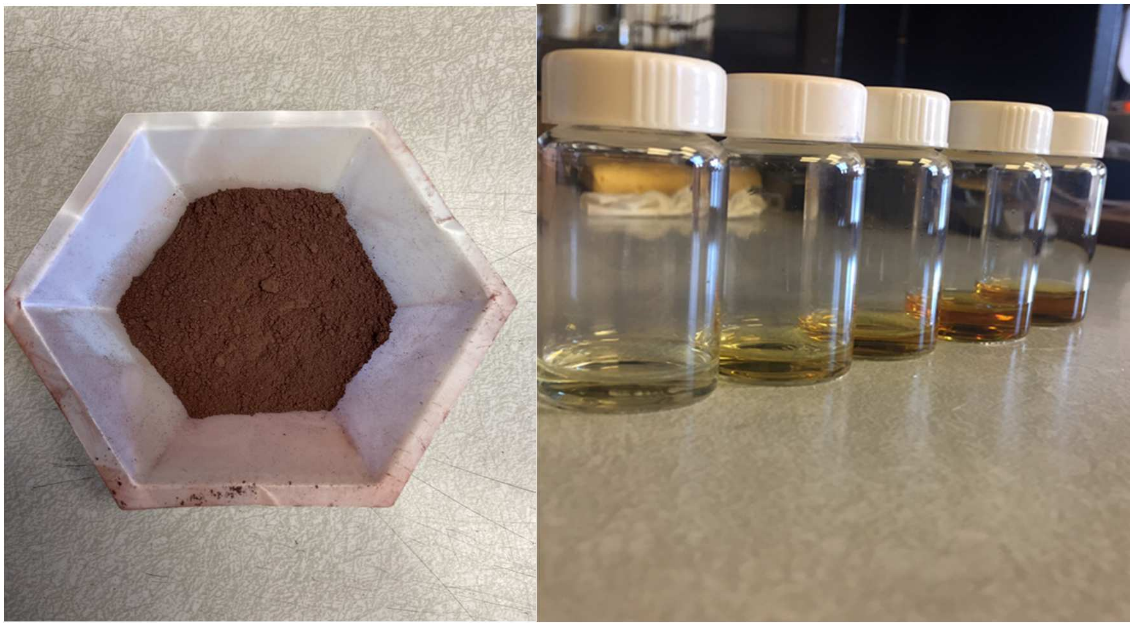

Figure 4-23 Fine sample of a great western ore (left) and collected samples (right)

Table 4-12 Concentration of extracted Iron (ppm) from fine ore Versus Time for a 6-hour reaction

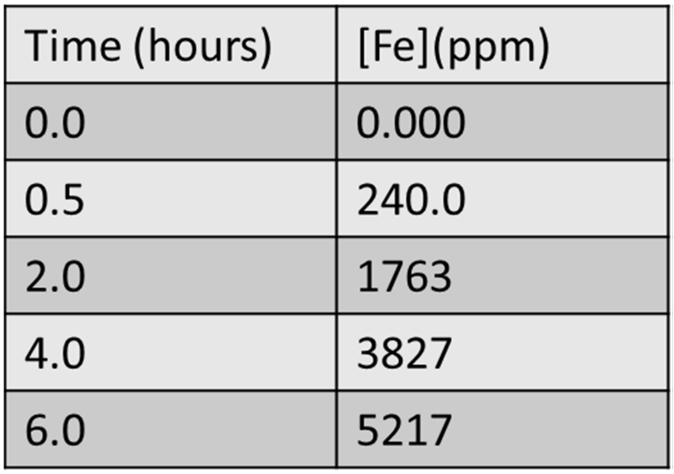

Time (hours)	[Fe](ppm)
0.0	0.000
0.5	240.0
2.0	1763
4.0	3827
6.0	5217

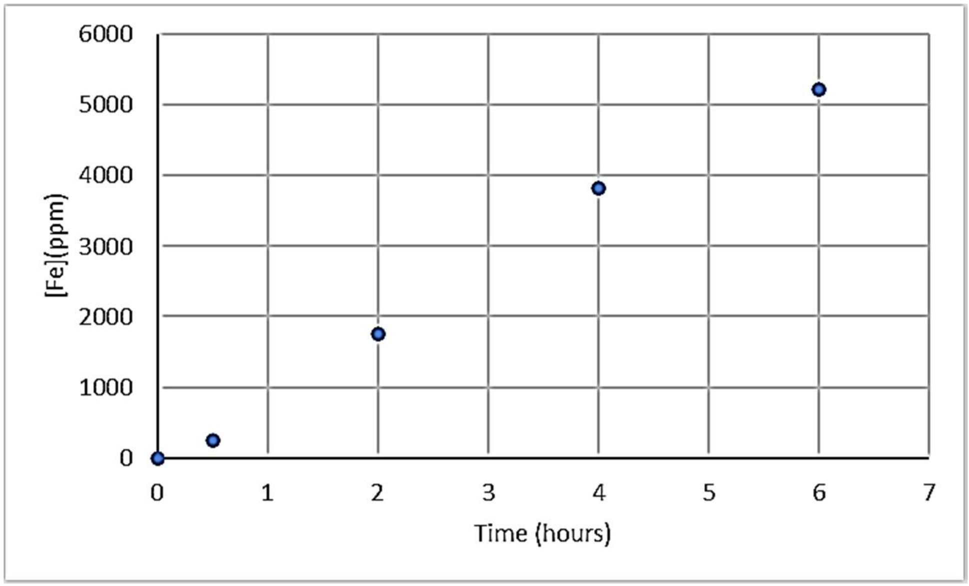

Figure 4-24 A linear plot of concentration of extracted Iron (ppm) from fine ore versus time for a 6-hour reaction

Experimental (Fe-Ni-EDTA)

Reaction of iron oxide Fe_2O_3 with ethylenediaminetetraacetic acid (H_4EDTA) and nickel hydroxide $Ni(OH)_2$

First of all, reaction of Fe_2O_3 (3.164 g, 0.02 mmol) was allowed to react with ethylenediaminetetraacetic acid (11.627 g, 0.04 mmol) in 200 ml of distilled water. Reaction was performed under refluxing. The pH was determined to be 2.98 immediately after the mixture. The reaction of the mixture became a red clear solution after fifteen hours. After that, the acidity of the reaction was measured before adding the next reagent to be 2.30. Next, nickel hydroxide (1.821 g, 0.02 mmol) was added to the reaction of iron oxide (Fe_2O_3) with ethylenediaminetetraacetic acid (-H_4EDTA), the pH was increased slightly to be 3.25 immediately after adding the reagent of the nickel hydroxide and a dark green color of the mixture was recorded. Afterward, the reaction was allowed to run for two more 48 hours. Finally, The mixture of the complex was transferred in a beaker to be evaporated at room temperature for two months. A dark green moisture was formed after evaporation. Later, the product was placed in a furnace at 90 □ overnight to dry off water. Dark grey blackish solid was collected with 8.654 g.

Result and Discussion

Reaction of iron oxide Fe_2O_3 with ethylenediaminetetraacetic acid (H_4EDTA) and nickel hydroxide $Ni(OH)_2$

A mixture of a stoichiometric amount of iron oxide and ethylenediaminetetraacetic acid (H_4EDTA) in 200 ml of water was heated at reflux for 48 hours. During that time, iron was absorbed from the solution to produce clear dark red. The composition of the reaction was iron complex of H-Fe-EDTA. Next, nickel hydroxide (1.821 g, 0.02 mmol) was in order to form iron nickel complex. Finally, a ternary compound of $NiFe_2O_4$ with a cubic phase was formed upon calcination and this was confirmed by XRD Figure 4-27. After evaporation, and drying the solid, the thermogravimetric analysis was used to get to know the complex compound. The TGA trace, shown in (Figure 4-26), had two weight loss steps with 69.55 % of total loss. The step occurred over the temperature range of 76 □ to 245.35 □ can be attributed to loss of water with 28.54 equivalents. The second step was a decomposition at the temperature 367 □ to 803 □ which can be attributed to ethylenediaminetetraacetic acid (-H_4EDTA) with half of the total loss of the precursor with 142.88 equivalents. This was confirmed by FTIR spectroscopy as discussed below. There was also a gradual loss over the range from 641 □ to 803 □ due the conversion of $Ni(Fe\text{-}EDTA)_2$ to bimetallic oxide of $NiFe_2O_4$. According to (Figure 4-25), spectrum show band attributable to acetate groups at 1567 cm^{-1} that are due to the symmetric stretching vibrations of the CO2 group of ethylenediaminetetraacetate confirming the presence of EDTA in the product from the reaction with Fe_2O_3. It also has strong bands at 659 and 910 cm^{-1}, these are stretching vibration of a metal oxide of Fe-O. There is also a broad peak over the range from 3630 cm^{-1} to 3063 cm^{-1} that can be attributed to the stretching vibration of a H-O-H molecule attached to a metal ion.

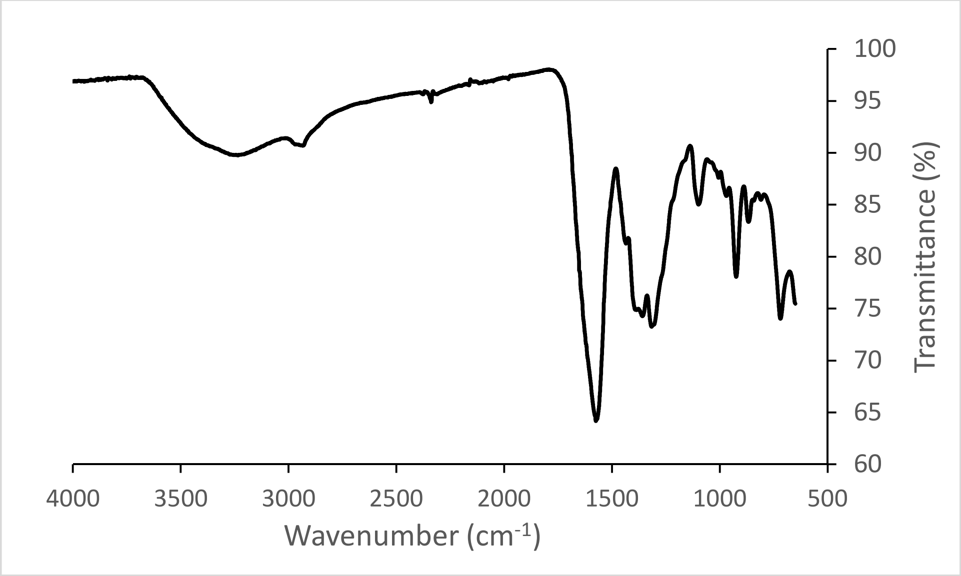

Figure 4-25 Infrared spectroscopy of Reaction of iron oxide Fe_2O_3 with ethylenediaminetetraacetic acid (H4EDTA) and nickel hydroxide $Ni(OH)_2$

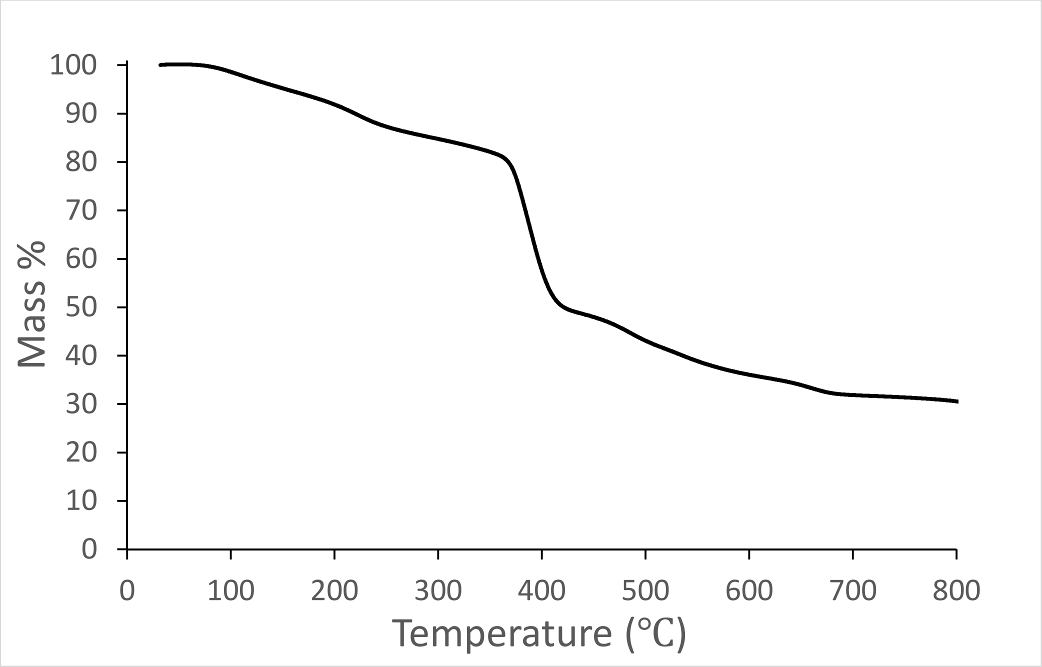

Figure 4-26 Thermal Gravimetric Analysis of Reaction of iron oxide Fe_2O_3 with ethylenediaminetetraacetic acid (H4EDTA) and nickel hydroxide $Ni(OH)_2$

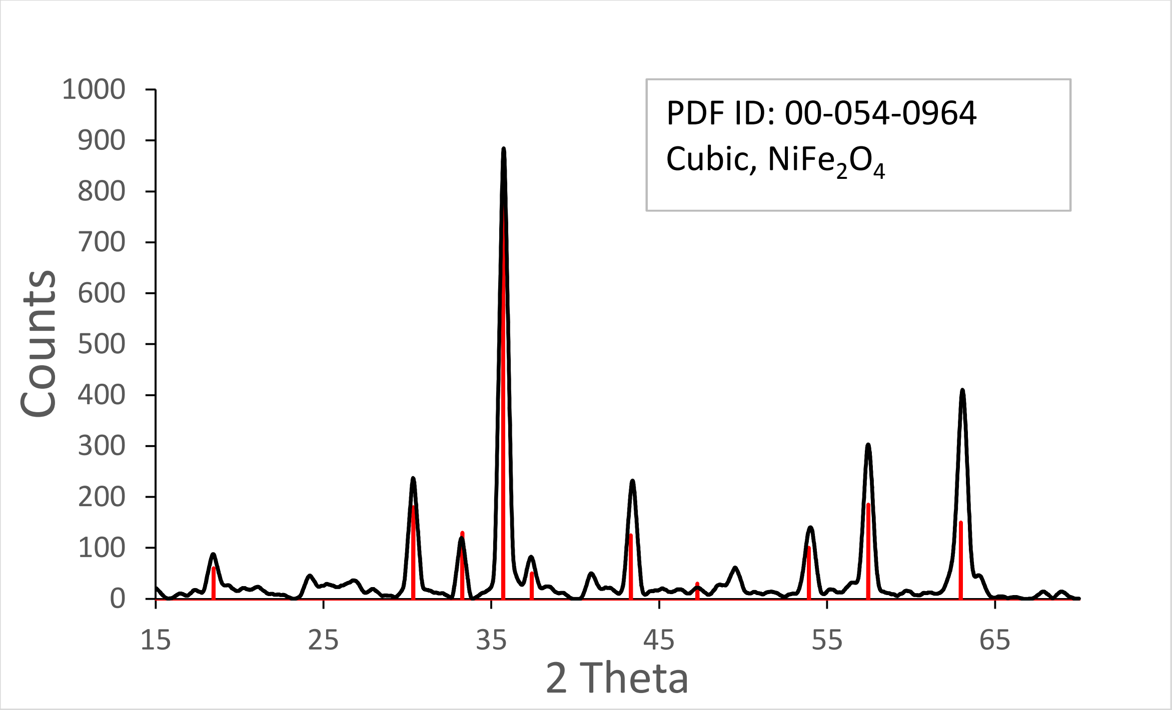

Figure 4-27 XRD of calcined product from Reaction of iron oxide Fe_2O_3 with ethylenediaminetetraacetic acid (H4EDTA) and nickel hydroxide $Ni(OH)_2$

CHAPTER V

CONCLUSIONS AND FUTURE WORK

Introduction

During an assessment of the utility of molybdenum trioxide and tungsten trioxide for the removal of metal ions from simulated radioactive waste, the Apblett group identified an alternative for the production of lanthanum molybdenum oxide phases in aqueous media[178]. The research suggests that insoluble molybdenum trioxide, tungsten trioxide, and tungstic acid have a strong ability to remove uranium, lead, cadmium, and other heavy metals from aqueous solutions using a chemical reaction with molybdenum trioxide and tungsten trioxide/tungstic acid to yield tungstate or molybdate. This capability can be applied to the refining of metal-bearing ores, the remediation of contaminated water, and even the extraction of metals from natural waterways, such as the seas. These reactions, on the other hand, give a green path to metal tungstate or metal molybdate, which have a wide range of applications[179-181].

In comparison to lanthanide molybdate acetates and lanthanide tungstate acetates, the purpose of this study was to see what factors influence the formation of lanthanide molybdate hydroxides. It was hypothesized that the ionic radii of lanthanide(III) ions influenced the molybdenum trioxide or tungsten trioxide reactions with lanthanide acetates. As a result, varied ionic radii of yttrium, lanthanum, cerium, and praseodymium were used in reactions. The purpose of this study was to make new lanthanide phases with the formula $Ln_2Mo_2O_9$ that could be employed as catalysts or oxide conductors. The lanthanide ions have no effect on the molybdate ion's vibrational activity. Finally, knowledge obtained from the synthesis of lanthanide molybdate acetates and lanthanide tungstate acetates was used to synthesize phosphors based on praseodymium-doped La2Mo2O9..[124] Moreover, $La_2W_2O_9$ and other lanthanide tungsten oxide may be applied for better efficiency due to its dependency of metal radius of tungsten used instead of molybdenum. In conclusion, there is a similar approach for producing $M_2W_2O_9$ as a bimetallic oxide where M can be either transition or lanthanide metals. Reaction of tungstic acid, H_2WO_4, with aqueous solutions of lanthanum acetates produces lanthanum tungstate acetate, $Ln(O_2CCH_3)(WO_4)$. Moreover, reacting iron(III) nitrate with molybdenum(VI) oxide (MoO_3) in acetate buffer solution produce different colored solids that result from reactions, suggesting that more than one product is being formed. With excess stoichiometry of Fe:Mo, reactions produced 2 phases of hematite and $Fe_2(MoO_4)$ at elevated temperatures. As a result, that the reaction of iron nitrate to molybdenum trioxide is very dependent, so a suitable ratio of iron(III) nitrate with molybdenum(VI) for producing one phase of $Fe_2(MoO_4)$ is possible which will remain as a future work.

In the last project, a process of extraction of iron from both pure iron oxide (Fe_2O_3) and Great Western Iron ore were investigated using ethylenediaminetetraacetic acid (H_4EDTA) This produces Fe(HEDTA), a chelated iron that is used in fertilizers as well as a conversion to red iron oxide or a possible ferrite oxide. Notably, two equivalents of Fe(HEDTA react with nickel(II) hydroxide to produce a stoichiometric precursor for nickel ferrite, $NiFe_2O$. Iron is readily extracted from even small chunks of ore by reaction of hematite with ethylenediaminetetraacetic acid (H_4EDTA). This can produce Fe_2O_3 upon high temperatures. The novel extraction discussed earlier in this thesis may be very useful for other different ores that contain different vital metals such as gold, silver. Moreover, the process produces the useful compound Fe(HEDTA) that can be used again for further iron extraction processes due to its catalytic advantage that can catalyze the dissolution of iron so the reaction is so-called self-catalytic. Fe(HEDTA) may be used to produce a stoichiometric single source precursor for nickel ferrite ($NiFe_2O_4$) or copper ferrite ($CuFe_2O_4$) for a future research.

REFERENCES

1. Kihlborg, L., Least-squares refinement of the crystal structure of Mo trioxide. *Ark. Kemi* **1963,** *21* (34), 357.

2. Loopstra, B. O.; Rietveld, H. M., Further refinement of the structure of WO3. *Acta Crystallographica Section B* **1969,** *25* (7), 1420-1421.

3. Szymanski, J. T.; Roberts, A. C., The crystal structure of tungstite, WO 3 .H 2 O. *The Canadian Mineralogist* **1984,** *22* (4), 681-688.

4. Evans, I. R.; Howard, J. A. K.; Evans, J. S. O., The Crystal Structure of α-La2Mo2O9 and the Structural Origin of the Oxide Ion Migration Pathway. *Chemistry of Materials* **2005,** *17* (16), 4074-4077.

5. Jeitschko, W.; Sleight, A. W., Synthesis, properties and crystal structure of β-SnWO4. *Acta Crystallographica Section B* **1972,** *28* (11), 3174-3178.

6. Goutenoire, F.; Isnard, O.; Retoux, R., Crystal Structure of La2Mo2O9, a New Fast Oxide−Ion Conductor. *Chemistry of Materials* **2000,** *12* (9), 2575-2580.

7. He, X.; Guan, M.; Zhang, C.; Shang, T.; Lian, N.; Zhou, Q., Luminescence enhancement of Eu3+-activated La2Mo2O9 red-emitting phosphor through chemical substitution. *Journal of Materials Research* **2011,** *26* (18), 2379-2383.

8. Collado, J. A.; Aranda, M. A. G.; Cabeza, A.; Olivera-Pastor, P.; Bruque, S., Synthesis, Structures, and Thermal Expansion of the La2W2−xMoxO9 Series. *Journal of Solid State Chemistry* **2002,** *167* (1), 80-85.

9. Švarcová, S.; Klementová, M.; Bezdička, P.; Łasocha, W.; Dušek, M.; Hradil, D., Synthesis and characterization of single crystals of the layered copper hydroxide acetate Cu2(OH)3(CH3COO)·H2O. *Crystal Research and Technology* **2011,** *46* (10), 1051-1057.

10. Nicholls, J. L.; Hulse, S. E.; Callear, S. K.; Tizzard, G. J.; Stephenson, R. A.; Hursthouse, M. B.; Clegg, W.; Harrington, R. W.; Fogg, A. M., Synthesis and Structure of Pillared Molybdates and Tungstates with Framework Layers. *Inorganic Chemistry* **2010,** *49* (18), 8545-8551.

11. Figgis, B. N.; Robertson, G. B., Crystal-Molecular Structure and Magnetic Properties of Cr3 (CH3.COO)6 O Cl.5H2O. *Nature* **1965,** *205* (4972), 694-695.

12. König, U.; Morgenstern, T.; Försterling, G. In *A study of structural crystallography on ternary metal oxides in the system Fe-Mo-O*, 1993; Trans Tech Publ: pp 687-692.

13. Rapposch, M. H.; Anderson, J. B.; Kostiner, E., Crystal structure of ferric molybdate, Fe2(MoO4)3. *Inorg. Chem.* **1980,** *19* (11), 3531-9.

14. Harrison, W. T. A., Crystal structures of paraelastic aluminum molybdate and ferric molybdate, β-Al2(MoO4)3 and β-Fe2(MoO4)3. *Materials Research Bulletin* **1995,** *30* (11), 1325-1331.

15. Gur'ev, A. V.; Flor, G.; Marini, A.; Massarotti, V.; Riccardi, R., Characterization of the high-temperature form of ferric molybdate (Fe2(MoO4)3). *Z. Naturforsch., A* **1981,** *36A* (3), 280-2.

16. Ehrenberg, H.; Muessig, E.; Bramnik, K. G.; Kampe, P.; Hansen, T., Preparation and properties of sodium iron orthooxomolybdates, NaxFey(MoO4)z. *Solid State Sciences* **2006,** *8* (7), 813-820.

17. Yang, Z.; Giester, G., Hydrogen bonding in goldichite, KFe(SO4)2·4H2O: structure refinement. *Mineralogy and Petrology* **2018,** *112* (1), 135-142.

18. Braithwaite, E. R.; Haber, J., *Molybdenum: an outline of its chemistry and uses*. Elsevier: 2013; Vol. 19.

19. Alves de Castro, I.; Datta, R. S.; Ou, J. Z.; Castellanos-Gomez, A.; Sriram, S.; Daeneke, T.; Kalantar-zadeh, K., Molybdenum Oxides - From Fundamentals to Functionality. *Adv. Mater. (Weinheim, Ger.)* **2017,** *29* (40), n/a.

20. Bagheri, S.; Muhd Julkapli, N., Mo3VOx catalyst in biomass conversion: A review in structural evolution and reaction pathways. *Int. J. Hydrogen Energy* **2017,** *42* (4), 2116-2126.

21. Cronin, L.; Kogerler, P.; Muller, A., Controlling growth of novel solid-state materials via discrete molybdenum-oxide-based building blocks as synthons. *J. Solid State Chem.* **2000,** *152* (1), 57-67.

22. de, C. I. A.; Datta, R. S.; Ou, J. Z.; Sriram, S.; Daeneke, T.; Kalantar-Zadeh, K.; Castellanos-Gomez, A., Molybdenum Oxides - From Fundamentals to Functionality. *Adv Mater* **2017,** *29* (40).

23. Ellefson, C. A.; Marin-Flores, O.; Ha, S.; Norton, M. G., Synthesis and applications of molybdenum (IV) oxide. *J. Mater. Sci.* **2012,** *47* (5), 2057-2071.

24. Proust, A.; Thouvenot, R.; Gouzerh, P., Functionalization of polyoxometalates: towards advanced applications in catalysis and materials science. *Chem. Commun. (Cambridge, U. K.)* **2008,** (16), 1837-1852.

25. Ren, H.; Sun, S.; Cui, J.; Li, X., Synthesis, Functional Modifications, and Diversified Applications of Molybdenum Oxides Micro-/Nanocrystals: A Review. *Cryst. Growth Des.* **2018,** *18* (10), 6326-6369.

26. Saji, V. S.; Lee, C.-W., Molybdenum, Molybdenum Oxides, and their Electrochemistry. *ChemSusChem* **2012,** *5* (7), 1146-1161.

27. Zharikov, E. V.; Zaldo, C.; Diaz, F., Double tungstate and molybdate crystals for laser and nonlinear optical applications. *MRS Bull.* **2009,** *34* (4), 271-276.

28. Stamenkovic, V. R.; Strmcnik, D.; Lopes, P. P.; Markovic, N. M., Energy and fuels from electrochemical interfaces. *Nature Materials* **2016,** *16* (1), 57-69.

29. Jiao, Y.; Zheng, Y.; Jaroniec, M.; Qiao, S. Z., Design of electrocatalysts for oxygen- and hydrogen-involving energy conversion reactions. *Chemical Society Reviews* **2015,** *44* (8), 2060-2086.

30. Shi, Y.; Zhang, B., Erratum: Recent advances in transition metal phosphide nanomaterials: Synthesis and applications in hydrogen evolution reaction (Chemical Society Reviews (2016) DOI: 10.1039/c5cs00434a). *Chemical Society Reviews* **2016,** *45* (6), 1781.

31. Wang, Y.; Qian, G.; Xu, Q.; Zhang, H.; Shen, F.; Luo, L.; Yin, S., Industrially promising IrNi-FeNi3 hybrid nanosheets for overall water splitting catalysis at large current density. *Applied Catalysis B: Environmental* **2021,** *286*.

32. Bruce, P. G.; Freunberger, S. A.; Hardwick, L. J.; Tarascon, J. M., LigO2 and LigS batteries with high energy storage. *Nature Materials* **2012,** *11* (1), 19-29.

33. Stoerzinger, K. A.; Diaz-Morales, O.; Kolb, M.; Rao, R. R.; Frydendal, R.; Qiao, L.; Wang, X. R.; Halck, N. B.; Rossmeisl, J.; Hansen, H. A.; Vegge, T.; Stephens, I. E. L.; Koper, M. T. M.; Shao-Horn, Y., Orientation-Dependent Oxygen Evolution on RuO2 without Lattice Exchange. *ACS Energy Letters* **2017,** *2* (4), 876-881.

34. Zhang, Y.; Fu, J.; Zhao, H.; Jiang, R.; Tian, F.; Zhang, R., Tremella-like Ni3S2/MnS with ultrathin nanosheets and abundant oxygen vacancies directly used for high speed overall water splitting. *Applied Catalysis B: Environmental* **2019,** *257*.

35. Li, Z.; Zheng, M.; Zhao, X.; Yang, J.; Fan, W., Synergistic engineering of architecture and composition in Ni:XCo1-xMoO4@CoMoO4 nanobrush arrays towards efficient overall water splitting electrocatalysis. *Nanoscale* **2019,** *11* (47), 22820-22831.

36. Ding, Y.; Miao, B. Q.; Jiang, Y. C.; Yao, H. C.; Li, X. F.; Chen, Y., Polyethylenimine-modified nickel phosphide nanosheets: Interfacial protons boost the hydrogen evolution reaction. *Journal of Materials Chemistry A* **2019,** *7* (22), 13770-13776.

37. Yin, Z.; Zhang, S.; Chen, W.; Xinzhi, M.; Zhou, Y.; Zhang, Z.; Wang, X.; Li, J., Hybrid-atom-doped NiMoO4nanotubes for oxygen evolution reaction. *New Journal of Chemistry* **2020,** *44* (40), 17477-17482.

38. Li, R.; Guo, Y.; Chen, H.; Wang, K.; Tan, R.; Long, B.; Tong, Y.; Tsiakaras, P.; Song, S.; Wang, Y., Anion-Cation Double Doped Co3O4 Microtube Architecture to Promote High-Valence Co Species Formation for Enhanced Oxygen Evolution Reaction. *ACS Sustainable Chemistry and Engineering* **2019,** *7* (13), 11901-11910.

39. Liang, Y.; Wang, H.; Zhou, J.; Li, Y.; Wang, J.; Regier, T.; Dai, H., Covalent hybrid of spinel manganese-cobalt oxide and graphene as advanced oxygen reduction electrocatalysts. *Journal of the American Chemical Society* **2012,** *134* (7), 3517-3523.

40. Ma, T. Y.; Dai, S.; Jaroniec, M.; Qiao, S. Z., Metal-organic framework derived hybrid Co3O4-carbon porous nanowire arrays as reversible oxygen evolution electrodes. *Journal of the American Chemical Society* **2014,** *136* (39), 13925-13931.

41. An, L.; Feng, J.; Zhang, Y.; Wang, R.; Liu, H.; Wang, G. C.; Cheng, F.; Xi, P., Epitaxial Heterogeneous Interfaces on N-NiMoO4/NiS2 Nanowires/Nanosheets to Boost Hydrogen and Oxygen Production for Overall Water Splitting. *Advanced Functional Materials* **2019,** *29* (1).

42. Liu, Z.; Yuan, C.; Teng, F., Crystal facets-predominated oxygen evolution reaction activity of earth abundant CoMoO4 electrocatalyst. *Journal of Alloys and Compounds* **2019,** *781*, 460-466.

43. Jiang, H.; Cui, Z.; Xu, C.; Li, W., Humid atmospheric pressure plasma jets exposed micro-defects on CoMoO4 nanosheets with enhanced OER performance. *Chemical Communications* **2019,** *55* (64), 9432-9435.

44. Fei, B.; Chen, Z.; Ha, Y.; Wang, R.; Yang, H.; Xu, H.; Wu, R., Anion-cation co-substitution activation of spinel CoMoO4 for efficient oxygen evolution reaction. *Chemical Engineering Journal* **2020,** *394*.

45. Lai, F.; Feng, J.; Ye, X.; Zong, W.; He, G.; Miao, Y. E.; Han, X.; Ling, X. Y.; Parkin, I. P.; Pan, B.; Sun, Y.; Liu, T., Energy level engineering in transition-metal doped spinel-structured nanosheets for efficient overall water splitting. *Journal of Materials Chemistry A* **2019,** *7* (2), 827-833.

46. Chi, K.; Tian, X.; Wang, Q.; Zhang, Z.; Zhang, X.; Zhang, Y.; Jing, F.; Lv, Q.; Yao, W.; Xiao, F.; Wang, S., Oxygen vacancies engineered CoMoO4 nanosheet arrays as efficient bifunctional electrocatalysts for overall water splitting. *Journal of Catalysis* **2020,** *381*, 44-52.

47. Gong, Y.; Yang, Z.; Lin, Y.; Wang, J.; Pan, H.; Xu, Z., Hierarchical heterostructure NiCo2O4@CoMoO4/NF as an efficient bifunctional electrocatalyst for overall water splitting. *Journal of Materials Chemistry A* **2018,** *6* (35), 16950-16958.

48. Xiao, Z.; Xie, C.; Wang, Y.; Chen, R.; Wang, S., Recent advances in defect electrocatalysts: Preparation and characterization. *Journal of Energy Chemistry* **2020,** *53*, 208-225.

49. Wang, Z.; Liu, H.; Ge, R.; Ren, X.; Ren, J.; Yang, D.; Zhang, L.; Sun, X., Phosphorus-Doped Co3O4 Nanowire Array: A Highly Efficient Bifunctional Electrocatalyst for Overall Water Splitting. *ACS Catalysis* **2018,** *8* (3), 2236-2241.

50. Xu, L.; Wang, Z.; Wang, J.; Xiao, Z.; Huang, X.; Liu, Z.; Wang, S., N-doped nanoporous Co3O4 nanosheets with oxygen vacancies as oxygen evolving electrocatalysts. *Nanotechnology* **2017,** *28* (16).

51. Liu, Y.; Hua, X.; Xiao, C.; Zhou, T.; Huang, P.; Guo, Z.; Pan, B.; Xie, Y., Heterogeneous Spin States in Ultrathin Nanosheets Induce Subtle Lattice Distortion to Trigger Efficient Hydrogen Evolution. *Journal of the American Chemical Society* **2016,** *138* (15), 5087-5092.

52. Wang, Y.; Zhou, T.; Jiang, K.; Da, P.; Peng, Z.; Tang, J.; Kong, B.; Cai, W. B.; Yang, Z.; Zheng, G., Reduced mesoporous Co3O4 nanowires as efficient water oxidation electrocatalysts and supercapacitor electrodes. *Advanced Energy Materials* **2014,** *4* (16).

53. He, W.; Han, L.; Hao, Q.; Zheng, X.; Li, Y.; Zhang, J.; Liu, C.; Liu, H.; Xin, H. L., Fluorine-Anion-Modulated Electron Structure of Nickel Sulfide Nanosheet Arrays for Alkaline Hydrogen Evolution. *ACS Energy Letters* **2019,** *4* (12), 2905-2912.

54. Xu, K.; Sun, Y.; Li, X.; Zhao, Z.; Zhang, Y.; Li, C.; Fan, H. J., Fluorine-Induced Dual Defects in Cobalt Phosphide Nanosheets Enhance Hydrogen Evolution Reaction Activity. *ACS Materials Letters* **2020,** *2* (7), 736-743.

55. Liu, S.; Yin, Y.; Ni, D.; Hui, K. S.; Hui, K. N.; Lee, S.; Ouyang, C. Y.; Jun, S. C., Phosphorous-containing oxygen-deficient cobalt molybdate as an advanced electrode material for supercapacitors. *Energy Storage Materials* **2019,** *19*, 186-196.

56. Pan, Y.; Lin, Y.; Chen, Y.; Liu, Y.; Liu, C., Cobalt phosphide-based electrocatalysts: Synthesis and phase catalytic activity comparison for hydrogen evolution. *Journal of Materials Chemistry A* **2016,** *4* (13), 4745-4754.

57. Li, R.; Hu, B.; Yu, T.; Chen, H.; Wang, Y.; Song, S., Insights into Correlation among Surface-Structure-Activity of Cobalt-Derived Pre-Catalyst for Oxygen Evolution Reaction. *Advanced Science* **2020,** *7* (5).

58. Zhao, J.; Li, H.; Li, C.; Zhang, Q.; Sun, J.; Wang, X.; Guo, J.; Xie, L.; Xie, J.; He, B.; Zhou, Z.; Lu, C.; Lu, W.; Zhu, G.; Yao, Y., MOF for template-directed growth of well-oriented nanowire hybrid arrays on carbon nanotube fibers for wearable electronics integrated with triboelectric nanogenerators. *Nano Energy* **2018,** *45*, 420-431.

59. Zhang, X.; Meng, F.; Mao, S.; Ding, Q.; Shearer, M. J.; Faber, M. S.; Chen, J.; Hamers, R. J.; Jin, S., Amorphous MoSxCly electrocatalyst supported by vertical graphene for efficient electrochemical and photoelectrochemical hydrogen generation. *Energy and Environmental Science* **2015,** *8* (3), 862-868.

60. Meng, J.; Fu, J.; Yang, X.; Wei, M.; Liang, S.; Zang, H. Y.; Tan, H.; Wang, Y.; Li, Y., Efficient MMoO4 (M = Co, Ni) carbon cloth electrodes for water oxidation. *Inorganic Chemistry Frontiers* **2017,** *4* (11), 1791-1797.

61. Vasilopoulou, M.; Douvas, A. M.; Georgiadou, D. G.; Palilis, L. C.; Kennou, S.; Sygellou, L.; Soultati, A.; Kostis, I.; Papadimitropoulos, G.; Davazoglou, D.; Argitis, P., The influence of hydrogenation and oxygen vacancies on molybdenum oxides work function and gap states for application in organic optoelectronics. *Journal of the American Chemical Society* **2012,** *134* (39), 16178-16187.

62. Tan, J.; Liu, L.; Guo, S.; Hu, H.; Yan, Z.; Zhou, Q.; Huang, Z.; Shu, H.; Yang, X.; Wang, X., The electrochemical performance and mechanism of cobalt (II) fluoride as anode material for lithium and sodium ion batteries. *Electrochimica Acta* **2015,** *168*, 225-233.

63. Wu, F.; Liao, Q.; Cao, F.; Li, L.; Zhang, Y., Non-noble bimetallic NiMoO4 nanosheets integrated Si photoanodes for highly efficient and stable solar water splitting. *Nano Energy* **2017,** *34*, 8-14.

64. Xu, L.; Jiang, Q.; Xiao, Z.; Li, X.; Huo, J.; Wang, S.; Dai, L., Plasma-Engraved Co3O4 Nanosheets with Oxygen Vacancies and High Surface Area for the Oxygen Evolution Reaction. *Angewandte Chemie - International Edition* **2016,** *55* (17), 5277-5281.

65. Yang, R.; Lu, X.; Huang, X.; Chen, Z.; Zhang, X.; Xu, M.; Song, Q.; Zhu, L., Bi-component Cu2O-CuCl composites with tunable oxygen vacancies and enhanced photocatalytic properties. *Applied Catalysis B: Environmental* **2015,** *170-171*, 225-232.

66. Wang, K.; Huang, J.; Chen, H.; Wang, Y.; Song, S., Recent advances in electrochemical 2e oxygen reduction reaction for on-site hydrogen peroxide production and beyond. *Chemical Communications* **2020,** *56* (81), 12109-12121.

67. Suen, N. T.; Hung, S. F.; Quan, Q.; Zhang, N.; Xu, Y. J.; Chen, H. M., Electrocatalysis for the oxygen evolution reaction: Recent development and future perspectives. *Chemical Society Reviews* **2017,** *46* (2), 337-365.

68. Shinagawa, T.; Garcia-Esparza, A. T.; Takanabe, K., Insight on Tafel slopes from a microkinetic analysis of aqueous electrocatalysis for energy conversion. *Scientific Reports* **2015,** *5*.

69. Zhang, G.; Wang, H.; Yang, J.; Zhao, Q.; Yang, L.; Tang, H.; Liu, C.; Chen, H.; Lin, Y.; Pan, F., Temperature Effect on Co-Based Catalysts in Oxygen Evolution Reaction. *Inorganic Chemistry* **2018,** *57* (5), 2766-2772.
70. Zhang, X.; Li, X.; Li, R.; Lu, Y.; Song, S.; Wang, Y., Highly Active Core–Shell Carbon/NiCo2O4 Double Microtubes for Efficient Oxygen Evolution Reaction: Ultralow Overpotential and Superior Cycling Stability. *Small* **2019,** *15* (42).
71. Kang, Z.; Guo, H.; Wu, J.; Sun, X.; Zhang, Z.; Liao, Q.; Zhang, S.; Si, H.; Wu, P.; Wang, L.; Zhang, Y., Engineering an Earth-Abundant Element-Based Bifunctional Electrocatalyst for Highly Efficient and Durable Overall Water Splitting. *Advanced Functional Materials* **2019,** *29* (9).
72. Abdou, E. S.; Nagy, K. S. A.; Elsabee, M. Z., Extraction and characterization of chitin and chitosan from local sources. *Bioresource Technology* **2008,** *99* (5), 1359-1367.
73. Bei, H.; Shim, S.; George, E. P.; Miller, M. K.; Herbert, E. G.; Pharr, G. M., Compressive strengths of molybdenum alloy micro-pillars prepared using a new technique. *Scripta Materialia* **2007,** *57* (5), 397-400.
74. Beil, S.; Schamberger, A.; Naumann, W.; MacHill, S.; Van Pée, K. H., Determination of the degree of N-acetylation (DA) of chitin and chitosan in the presence of water by first derivative ATR FTIR spectroscopy. *Carbohydrate Polymers* **2012,** *87* (1), 117-122.
75. Bertoni, F. A.; Medeot, A. C.; González, J. C.; Sala, L. F.; Bellú, S. E., Application of green seaweed biomass for MoVI sorption from contaminated waters. Kinetic, thermodynamic and continuous sorption studies. *Journal of Colloid and Interface Science* **2015,** *446*, 122-132.
76. Bezerra, M. A.; Santelli, R. E.; Oliveira, E. P.; Villar, L. S.; Escaleira, L. A., Response surface methodology (RSM) as a tool for optimization in analytical chemistry. *Talanta* **2008,** *76* (5), 965-977.
77. Blanes, P. S.; Bordoni, M. E.; González, J. C.; García, S. I.; Atria, A. M.; Sala, L. F.; Bellú, S. E., Application of soy hull biomass in removal of Cr(VI) from contaminated waters. Kinetic, thermodynamic and continuous sorption studies. *Journal of Environmental Chemical Engineering* **2016,** *4* (1), 516-526.
78. Bof, M. J.; Bordagaray, V. C.; Locaso, D. E.; García, M. A., Chitosan molecular weight effect on starch-composite film properties. *Food Hydrocolloids* **2015,** *51*, 281-294.
79. Bohart, G. S.; Adams, E. Q., Some aspects of the behavior of charcoal with respect to chlorine. *Journal of the American Chemical Society* **1920,** *42* (3), 523-544.
80. Dodbiba, G.; Fujita, T.; Kikuchi, T.; Manjanna, J.; Matsuo, S.; Takahashi, H.; Tohji, K., Synthesis of iron-based adsorbents and their application in the adsorption of molybdenum ions in nitric acid solution. *Chemical Engineering Journal* **2011,** *166* (2), 496-503.
81. SAEGEBARTH, K. A., Mechanism of the Tungstic Acid Catalyzed Hydroxylation of Olefins. *The Journal of Organic Chemistry* **1959,** *24* (9), 1212-1214.
82. Seabold, J. A.; Choi, K.-S., Efficient and stable photo-oxidation of water by a bismuth vanadate photoanode coupled with an iron oxyhydroxide oxygen evolution catalyst. *Journal of the American Chemical Society* **2012,** *134* (4), 2186-2192.
83. Wasmi, B. A.; Al-Amiery, A. A.; Kadhum, A. A. H.; Mohamad, A. B., Novel approach: tungsten oxide nanoparticle as a catalyst for malonic acid ester synthesis via ozonolysis. *Journal of Nanomaterials* **2014,** *2014*.
84. Dubey, S. S.; Gupta, R. K., Removal behavior of Babool bark (Acacia nilotica) for submicro concentrations of Hg2+ from aqueous solutions: A radiotracer study. *Separation and Purification Technology* **2005,** *41* (1), 21-28.
85. Elwakeel, K. Z.; Atia, A. A.; Donia, A. M., Removal of Mo(VI) as oxoanions from aqueous solutions using chemically modified magnetic chitosan resins. *Hydrometallurgy* **2009,** *97* (1-2), 21-28.
86. Faghihian, H.; Malekpour, A.; Maragheh, M. G., Adsorption of molybdate ion by natrolite and clinoptilolite-rich tuffs. *International Journal of Environment and Pollution* **2002,** *18* (2), 181-189.
87. Freundlich, H., Over the adsorption in solution. *Z. Phys. Chem.* **1906,** *57*, 385-470.

88. Fu, F.; Wang, Q., Removal of heavy metal ions from wastewaters: A review. *Journal of Environmental Management* **2011,** *92* (3), 407-418.

89. Chippindale, A. M.; Cheetham, A. K., Chapter 3 - The Oxide Chemistry of Molybdenum. In *Studies in Inorganic Chemistry*, Braithwaite, E. R.; Haber, J., Eds. Elsevier: 1994; Vol. 19, pp 146-184.

90. Wriedt, H. A., The O-W (oxygen-tungsten) system. *Bulletin of Alloy Phase Diagrams* **1989,** *10* (4), 368-384.

91. Cora, F.; Patel, A.; Harrison, N. M.; Dovesi, R.; Catlow, C. R. A., An ab initio Hartree− Fock study of the cubic and tetragonal phases of bulk tungsten trioxide. *Journal of the American Chemical Society* **1996,** *118* (48), 12174-12182.

92. Cui, M.; Mohajerin, T. J.; Adebayo, S.; Datta, S.; Johannesson, K. H., Investigation of tungstate thiolation reaction kinetics and sedimentary molybdenum/tungsten enrichments: Implication for tungsten speciation in sulfidic waters and possible applications for paleoredox studies. *Geochimica et Cosmochimica Acta* **2020,** *287*, 277-295.

93. Liu, Y.; Li, L.; Wang, R.; Li, J.; Huang, J.; Zhang, W., Multi-mode photocatalytic performances of CdS QDs modified CdIn 2 S 4 /CdWO 4 nanocomposites with high electron transfer ability. *Journal of Nanoparticle Research* **2018,** *20* (12).

94. Yang, J. H.; He, L. H.; Liu, X. H.; Ding, W. T.; Song, Y. F.; Zhao, Z. W., Comparative kinetic analysis of conventional and ultrasound-assisted leaching of scheelite by sodium carbonate. *Transactions of Nonferrous Metals Society of China (English Edition)* **2018,** *28* (4), 775-782.

95. Schreiber, R. E.; Avram, L.; Neumann, R., Self-Assembly through Noncovalent Preorganization of Reactants: Explaining the Formation of a Polyfluoroxometalate. *Chemistry - A European Journal* **2018,** *24* (2), 369-379.

96. Kapustin, V.; Chernysheva, E.; Maximova, A.; Zinchenko, Y., Development of new catalytic processes for processing petroleum feedstock. *Pure and Applied Chemistry* **2017,** *89* (10), 1579-1585.

97. Singh, K. B.; Maret, W., The interactions of metal cations and oxyanions with protein tyrosine phosphatase 1B. *BioMetals* **2017,** *30* (4), 517-527.

98. Sartzi, H.; Miras, H. N.; Vilà-Nadal, L.; Long, D. L.; Cronin, L., Trapping the δ Isomer of the Polyoxometalate-Based Keggin Cluster with a Tripodal Ligand. *Angewandte Chemie - International Edition* **2015,** *54* (51), 15488-15492.

99. Dunnick, K. M.; Badding, M. A.; Schwegler-Berry, D.; Patete, J. M.; Koenigsmann, C.; Wong, S. S.; Leonard, S. S., The Effect of Tungstate Nanoparticles on Reactive Oxygen Species and Cytotoxicity in Raw 264.7 Mouse Monocyte Macrophage Cells. *Journal of Toxicology and Environmental Health - Part A: Current Issues* **2014,** *77* (20), 1251-1268.

100. Shi, P.; Xia, Z.; Molokeev, M. S.; Atuchin, V. V., Crystal chemistry and luminescence properties of red-emitting CsGd 1-xEux(MoO4)2 solid-solution phosphors. *Dalton Transactions* **2014,** *43* (25), 9669-9676.

101. Liu, Y.; Wang, Y.; Wang, L.; Gu, Y. Y.; Yu, S. H.; Lu, Z. G.; Sun, R., General synthesis of LiLn(MO4)2:Eu3+ (Ln = La, Eu, Gd, Y; M = W, Mo) nanophosphors for near UV-type LEDs. *RSC Advances* **2014,** *4* (9), 4754-4762.

102. Yu, Y.; Sun, C. Y.; Song, Z. G.; Zhang, X. R. In *The mechanism on separation of scheelite and calcium minerals in heating cleaning process*, IMPC 2014 - 27th International Mineral Processing Congress, 2014.

103. 2013 International Conference on Applied Science, Engineering and Technology, ICASET 2013. In *Advanced Materials Research*, 2013; Vol. 709.

104. Nsouli, N. H.; Chubarova, E. V.; Al-Oweini, R.; Bassil, B. S.; Sadakane, M.; Kortz, U., Organoruthenium-containing heteropoly-23-tungstate family [{Ru(L)} 2(α-XW11O39)2WO 2]m- (L = benzene, p-cymene; X = GeIV, Si IV, m = 10; BIII, m = 12). *European Journal of Inorganic Chemistry* **2013,** (10-11), 1742-1747.

105. Topa, D.; Makovicky, E., Eclarite: New data and interpretations. *Canadian Mineralogist* **2012,** *50* (2), 371-386.

106. Arakcheeva, A.; Logvinovich, D.; Chapuis, G.; Morozov, V.; Eliseeva, S. V.; Bünzli, J. C. G.; Pattison, P., The luminescence of Na xEu 3+(2-x)/3MoO 4 scheelites depends on the number of Eu-clusters occurring in their incommensurately modulated structure. *Chemical Science* **2012,** *3* (2), 384-390.

107. Qin, J.; Cao, M.; Li, N.; Hu, C., Graphene-wrapped WO3 nanoparticles with improved performances in electrical conductivity and gas sensing properties. *Journal of Materials Chemistry* **2011,** *21* (43), 17167-17174.

108. Brandão, T. A. S.; Robinson, H.; Johnson, S. J.; Hengge, A. C., impaired acid catalysis by mutation of a protein loop hinge residue in a YopH mutant revealed by crystal structures. *Journal of the American Chemical Society* **2009,** *131* (2), 778-786.

109. Barker, R. S.; Evans, I. R., Structural characterization of RE10W22O81 rare-earth tungstates (RE = Ce, Nd). *Acta Crystallographica Section B: Structural Science* **2008,** *64* (6), 708-712.

110. Yu, J.; Guo, H.; Davis, S. A.; Mann, S., Fabrication of hollow inorganic microspheres by chemically induced self-transformation. *Advanced Functional Materials* **2006,** *16* (15), 2035-2041.

111. Alyea, E. C.; Craig, D.; Dance, I.; Fisher, K.; Willett, G.; Scudder, M., The crystallisation of polyoxo-molybdate and -tungstate anions with phenylated phosphonium and arsonium cations, in relation to the crystal packing and species in solution. *CrystEngComm* **2005,** *7*, 491-503.

112. Neiman, A. Y.; Guseva, A. F.; Trifonova, M. V.; Sukhankina, I. V., Reactive surface diffusion during synthesis of molybdates and tungstates: The role of the phase constitution of products. *Russian Journal of Inorganic Chemistry* **2005,** *50* (3), 319-324.

113. Boulon, G., Yb3+-doped oxide crystals for diode-pumped solid state lasers: Crystal growth, optical spectroscopy, new criteria of evaluation and combinatorial approach. *Optical Materials* **2003,** *22* (2), 85-87.

114. Fauman, E. B.; Yuvaniyama, C.; Schubert, H. L.; Stuckey, J. A.; Saper, M. A., The x-ray crystal structures of Yersinia tyrosine phosphatase with bound tungstate and nitrate. Mechanistic implications. *Journal of Biological Chemistry* **1996,** *271* (31), 18780-18788.

115. Engelhardt, G.; Koller, H.; Sieger, P.; Depmeier, W.; Samoson, A., 27Al and 23Na double-rotation NMR of sodalites. *Solid State Nuclear Magnetic Resonance* **1992,** *1* (3), 127-135.

116. Van der Vlies, A.; Kishan, G.; Niemantsverdriet, J.; Prins, R.; Weber, T., Basic reaction steps in the sulfidation of crystalline tungsten oxides. *The Journal of Physical Chemistry B* **2002,** *106* (13), 3449-3457.

117. Bai, P.; Xing, W.; Yan, Z., Synthesis and characterization of mesostructured tungsten nitride by using tungstic acid as the precursor. *Journal of Porous Materials* **2006,** *13* (2), 173-180.

118. Cao, J.; Luo, B.; Lin, H.; Xu, B.; Chen, S., Thermodecomposition synthesis of WO3/H2WO4 heterostructures with enhanced visible light photocatalytic properties. *Applied Catalysis B: Environmental* **2012,** *111*, 288-296.

119. Eda, K.; Uno, Y.; Nagai, N.; Sotani, N.; Whittingham, M. S., Crystal structure of cobalt molybdate hydrate CoMoO 4· nH 2 O. *Journal of Solid State Chemistry* **2005,** *178* (9), 2791-2797.

120. Apblett, A. W.; Chehbouni, M.; Reinhardt, L. E., Novel routes to ferroelectric gadolinium molybdenum oxides. *Ceram. Trans.* **2006,** *174* (Advances in Dielectric Materials and Electronic Devices), 39-46.

121. Chehbouni, M. Environmental, synthetic, and materials applications of molybdenum trioxide. Ph.D. Dissertation, Oklahoma State University, 2006.

122. Chehbouni, M.; Al-Busaidi, H.; Apblett, A. W., Green process for uranium separations utilizing molybdenum trioxide. *ACS Symp. Ser.* **2010,** *1046* (Nuclear Energy and the Environment), 155-167.

123. Chehbouni, M.; Apblett, A. W., Molybdenum-oxide based sorbents for toxic metals. *Ceram. Trans.* **2006,** *176* (Environmental Issues and Waste Management Technologies in the Ceramic and Nuclear Industries XI), 15-23.

124. Alrashidi, K. Synthesis of lanthanide molybdates via reaction of molybdenum (VI) oxide with aqueous acetate salts. Oklahoma State University, 2018.

125. Goutenoire, F.; Isnard, O.; Suard, E.; Bohnke, O.; Laligant, Y.; Retoux, R.; Lacorre, P., Structural and transport characteristics of the LAMOX family of fast oxide-ion conductors, based on lanthanum molybdenum oxide La2Mo2O9. *Journal of Materials Chemistry* **2001,** *11* (1), 119-124.

126. Li, Q.; Lu, T.; Schiemer, J.; Laanait, N.; Balke, N.; Zhang, Z.; Ren, Y.; Carpenter, M. A.; Wen, H.; Li, J.; Kalinin, S. V.; Liu, Y., Giant thermally-enhanced electrostriction and polar surface phase in $\mathrm{L}{\mathrm{a}}_{2}\mathrm{M}{\mathrm{o}}_{2}{\mathrm{O}}_{9}$ oxygen ion conductors. *Physical Review Materials* **2018,** *2* (4), 041403.

127. Cheng, Q.; Ren, F.; Lin, Q.; Tong, H.; Miao, X., High quantum efficiency red emitting α-phase La2W2O9:Eu3+ phosphor. *J. Alloys Compd.* **2019,** *772*, 905-911.

128. Song, K.; Li, G.-M., Electrospinning synthesis, characterization and luminescence properties of La2W2O9: Eu3+ nanofibers. *J. Mater. Sci.: Mater. Electron.* **2016,** *27* (2), 1227-1231.

129. Zhang, J.; Yang, Y.; Yu, F.; Liu, Y.; Han, B.; Mi, C.; Liu, L., Synthesis and luminescence properties of La2W2O9:Eu3+ micron crystals. *J. Nanosci. Nanotechnol.* **2016,** *16* (4), 3852-3856.

130. Asiri Naidu, S.; Boudin, S.; Varadaraju, U. V.; Raveau, B., Photoluminescence Properties of Rare Earths (Eu3+, Tb3+, Dy3+ and Tm3+) Activated NaInW2O8 Wolframite Host Lattice. *J. Solid State Chem.* **2012,** *185*, 187.

131. Grobelna, B., Luminescence Based on Energy Transfer in Xerogels Doped with Ln2–xTbx(WO4)3. *J. Alloys Compd.* **2007,** *440*, 265.

132. Naruke, H.; Obaid, D. M., Structure Dependence of Near-Infrared Stimulated Blue Emission in Polycrystalline Ln2(WO4)3 (Ln = Gd and Lu) Doped with Tm and Yb. *J. Lumin.* **2009,** *129*, 1132.

133. Shivakumara, C.; Saraf, R.; Behera, S.; Dhananjaya, N.; Nagabhushana, H., Scheelite-Type MWO4 (M = Ca, Sr, and Ba) Nanophosphors: Facile Synthesis, Structural Characterization, Photoluminescence, and Photocatalytic Properties. *Mater. Res. Bull.* **2015,** *61*, 422.

134. Wang, Z. J.; Zhong, J. P.; Liang, H. B.; Wang, J., Luminescence Properties of Lutetium Based Red-Emitting Posphor NaLu(WO4)2:Eu3+. *Opt. Mater. Express* **2013,** *3*, 418.

135. Singh, K.; Vaidyanathan, S., Novel narrow band red emitters based on mixed metal oxides and their application in hybrid white light-emitting diodes. *Luminescence* **2021,** *36* (3), 576-587.

136. Zhou, W.; Liu, Y.; Sun, Q.; Ye, J.; Chen, L.; Wang, J.; Li, G.; Lin, H.; Ye, Y.; Chen, W., High Near-Infrared Reflectance Orange Pigments of Fe-Doped La2W2O9: Preparation, Characterization, and Energy Consumption Simulation. *ACS Sustainable Chem. Eng.* **2021,** *9* (36), 12385-12393.

137. Laligant, Y.; Le Bail, A.; Goutenoire, F., Ab Initio Structure Determination of Lanthanum Cyclo-tetratungstate α-La2W2O9 from X-ray and Neutron Powder Diffraction. *Journal of Solid State Chemistry* **2001,** *159* (1), 223-227.

138. Marrero-López, D.; Peña-Martínez, J.; Ruiz-Morales, J. C.; Núñez, P., Phase Stability and Ionic Conductivity in Substituted La2W2O9. *J. Solid State Chem.* **2008,** *181*, 253.

139. Deacon, G. B.; Phillips, R. J., Relationships between the carbon-oxygen stretching frequencies of carboxylato complexes and the type of carboxylate coordination. *Coordination Chemistry Reviews* **1980,** *33* (3), 227-250.

140. Carcelli, M.; Ianelli, S.; Pelagatti, P.; Pelizzi, G.; Rogolino, D.; Solinas, C.; Tegoni, M., Synthesis and characterization of new lanthanide complexes with hexadentate hydrazonic ligands. *Inorganica Chimica Acta* **2005,** *358* (4), 903-911.

141. Edwards, D. A.; Hayward, R. N., Transition metal acetates. *Canadian Journal of Chemistry* **1968,** *46* (22), 3443-3446.

142. Ribot, F.; Toledano, P.; Sanchez, C., X-ray and spectroscopic investigations of the structure of yttrium acetate tetrahydrate. *Inorganica Chimica Acta* **1991,** *185* (2), 239-245.
143. Benetollo, F.; Bombieri, G.; Vallarino, L. M., A lanthanium(III) complex of a six-nitrogen donor macrocyclic ligand with aromatic sidechains: synthesis, crystal structure and spectra. *Polyhedron* **1994,** *13* (4), 573-578.
144. Saleem, S. S.; Aruldhas, G., Raman and infrared spectra of lanthanum molybdate. *Journal of Solid State Chemistry* **1982,** *42* (2), 158-162.
145. Tarte, P.; Liegeois-Duyckaerts, M., Vibrational studies of molybdates, tungstates and related compounds—I: New infrared data and assignments for the scheelite-type compounds XIIMoO4 and XIIWO4. *Spectrochimica Acta Part A: Molecular Spectroscopy* **1972,** *28* (11), 2029-2036.
146. Kuriakose, S.; H, H.; Jose, A.; John, M.; Varghese, T., Structural and optical characterization of lanthanum tungstate nanoparticles synthesized by chemical precipitation route and their photocatalytic activity. *Optical Materials* **2020,** *99*, 109571.
147. da Rocha, S. M. R.; da Silva Queiroz, C. A.; Abrão, A. d., Synthesis and characterization of lanthanum acetate for application as a catalyst. *Journal of Alloys and Compounds* **2002,** *344* (1), 389-393.
148. AlKahlaway, A. A.; Betiha, M. A.; Aman, D.; Rabie, A. M., Facial synthesis of ferric molybdate (Fe2(MoO4)3) nanoparticle and its efficiency for biodiesel synthesis via oleic acid esterification. *Environ. Technol. Innovation* **2021,** *22*, 101386.
149. Bhuvana, C. V.; Viswanathan, B.; Sastri, M. V. C., Studies on the catalytic oxidation of propylene on ferric molybdate. *React. Kinet. Catal. Lett.* **1980,** *14* (3), 375-80.
150. Chapman, S.; Brookes, C.; Bowker, M.; Gibson, E. K.; Wells, P. P., Design and stabilisation of a high area iron molybdate surface for the selective oxidation of methanol to formaldehyde. *Faraday Discuss.* **2016,** *188* (Designing New Heterogeneous Catalysts), 115-129.
151. Chellappa, A. S.; Viswanath, D. S., Partial Oxidation of Methane Using Ferric Molybdate Catalyst. *Ind. Eng. Chem. Res.* **1995,** *34* (6), 1933-40.
152. Edwards, J.; Nicolaidis, J.; Cutlip, M. B.; Bennett, C. O., Methanol partial oxidation at low temperature. *J. Catal.* **1977,** *50* (1), 24-34.
153. Madhok, K. L.; Srivastava, K. P., Ferric molybdate - a catalyst for the oxidation of toluene. *Proc. - Indian Acad. Sci., [Ser.]: Chem. Sci.* **1981,** *90* (6), 527-35.
154. Novotny, P.; Yusuf, S.; Li, F.; Lamb, H. H., Oxidative dehydrogenation of ethane using MoO3/Fe2O3 catalysts in a cyclic redox mode. *Catal. Today* **2018,** *317*, 50-55.
155. Parveen, S.; Bhatti, I. A.; Ashar, A.; Javed, T.; Mohsin, M.; Hussain, M. T.; Khan, M. I.; Naz, S.; Iqbal, M., Synthesis, characterization and photocatalytic performance of iron molybdate (Fe2(MoO4)3) for the degradation of endosulfan pesticide. *Mater. Res. Express* **2020,** *7* (3), 035016.
156. Srihari, V.; Viswanath, D. S., Oxidation of ethanol over ferric molybdate catalyst. *J. Chem. Technol. Biotechnol.* **1982,** *32* (9), 868-76.
157. Suresh, P.; Umabala, A. M.; Siva Rao, T.; Prasada Rao, A. V., Visible light induced synergistic degradation of Rhodamine-B, Methylene blue and Malachite green by Fe2(MoO4)3 and MoO3. *J. Appl. Chem. (Lumami, India)* **2014,** *3* (2), 696-701, 6 pp.
158. Umapathy, V.; Manikandan, A.; Ramu, P.; Antony, S. A.; Neeraja, P., Synthesis and characterization of Fe2(MoO4)3 nano-photocatalyst by simple sol-gel method. *J. Nanosci. Nanotechnol.* **2016,** *16* (1), 987-993.
159. Wu, L.-b.; Wu, L.-h.; Yang, W.-m.; Frenkel, A. I., Study of the local structure and oxidation state of iron in complex oxide catalysts for propylene ammoxidation. *Catal. Sci. Technol.* **2014,** *4* (8), 2512-2519.
160. Sklute, E. C.; Jensen, H. B.; Rogers, A. D.; Reeder, R. J., Morphological, structural, and spectral characteristics of amorphous iron sulfates. *J Geophys Res Planets* **2015,** *120* (4), 809-830.

161. Ventruti, G.; Della Ventura, G.; Gomez, M. A.; Capitani, G.; Sbroscia, M.; Sodo, A., High-temperature study of basic ferric sulfate, FeOHSO4. *Physics and Chemistry of Minerals* **2020,** *47* (10), 43.
162. Forray, F. L.; Drouet, C.; Navrotsky, A., Thermochemistry of yavapaiite KFe(SO4)2: Formation and decomposition. *Geochimica et Cosmochimica Acta* **2005,** *69* (8), 2133-2140.
163. Sadeghi, O.; Zakharov Lev, N.; Nyman, M., Aqueous formation and manipulation of the iron-oxo Keggin ion. *Science* **2015,** *347* (6228), 1359-1362.
164. Sejkora, J.; Čejka, J.; Malíková, R.; López, A.; Xi, Y.; Frost, R. L., A Raman spectroscopic study of a hydrated molybdate mineral ferrimolybdite, Fe2(MoO4)3·7–8H2O. *Spectrochimica Acta Part A: Molecular and Biomolecular Spectroscopy* **2014,** *130*, 83-89.
165. Kerr, P. F.; Thomas, A. W.; Langer, A. M., The nature and synthesis of ferrimolybdite. *American Mineralogist* **1963,** *48* (1-2), 14-32.
166. Zhang, J.; Wang, S.; Ma, X.; Yao, S.; Lv, H.; Pan, Y.; Chernikov, R.; Heredia, E.; Lin, J.; Jia, Y., Observation of surface precipitation of ferric molybdate on ferrihydrite: Implication for the mobility and fate of molybdate in natural and hydrometallurgical environments. *Science of The Total Environment* **2022,** *807*, 150749.
167. Horn, E.; Kurahashi, M.; Huang, D.; Wu, C., Crystal data and X-ray powder-diffraction data for ferrimolybdite, Fe2(MoO4)36.8(H2O). *Powder Diffraction* **1995,** *10* (2), 101-103.
168. Bissonnette, J.; Essilfie-Dughan, J.; Moldovan, B. J.; Hendry, M. J., Sequestration of As and Mo in uranium mill precipitates (pH 1.5–9.2): An XAS study. *Applied Geochemistry* **2016,** *72*, 20-33.
169. Apblett, A. W.; Chehbouni, M.; Reinhardt, L. E., Novel Routes to Ferroelectric Gadolinium Molybdenum Oxides. *Ceramic Transactions* **2012,** *174*, 39-46.
170. Chapman, S.; Brookes, C.; Bowker, M.; Gibson, E. K.; Wells, P. P., Design and stabilisation of a high area iron molybdate surface for the selective oxidation of methanol to formaldehyde. *Faraday Discussions* **2016,** *188* (0), 115-129.
171. Zhang, X.; Gu, X.; Han, Y.; Parra-Álvarez, N.; Claremboux, V.; Kawatra, S., Flotation of iron ores: A review. *Mineral processing and extractive metallurgy review* **2021,** *42* (3), 184-212.
172. Heimbach, J.; Rieth, S.; Mohamedshah, F.; Slesinski, R.; Samuel-Fernando, P.; Sheehan, T.; Dickmann, R.; Borzelleca, J., Safety assessment of iron EDTA [sodium iron (Fe3+) ethylenediaminetetraacetic acid]: summary of toxicological, fortification and exposure data. *Food and chemical toxicology* **2000,** *38* (1), 99-111.
173. Souri, M. K., Aminochelate fertilizers: the new approach to the old problem; a review. *Open Agriculture* **2016,** *1* (1).
174. Mohanty, M.; Dhal, N. K.; Patra, P.; Das, B.; Reddy, P. S. R., Phytoremediation: a novel approach for utilization of iron-ore wastes. *Reviews of Environmental Contamination and Toxicology Volume 206* **2010**, 29-47.
175. Jones, A. M.; Griffin, P. J.; Waite, T. D., Ferrous iron oxidation by molecular oxygen under acidic conditions: The effect of citrate, EDTA and fulvic acid. *Geochimica et Cosmochimica Acta* **2015,** *160*, 117-131.
176. Willett, A. I.; Rittmann, B. E., Slow complexation kinetics for ferric iron and EDTA complexes make EDTA non-biodegradable. *Biodegradation* **2003,** *14* (2), 105-121.
177. Namduri, H.; Nasrazadani, S., Quantitative analysis of iron oxides using Fourier transform infrared spectrophotometry. *Corrosion Science* **2008,** *50* (9), 2493-2497.
178. Chehbouni, M. Environmental, synthetic, and materials applications of molybdenum trioxide. Ph.D., Oklahoma State University, Ann Arbor, 2006.
179. Malik, L. A.; Bashir, A.; Qureashi, A.; Pandith, A. H., Detection and removal of heavy metal ions: a review. *Environmental Chemistry Letters* **2019,** *17* (4), 1495-1521.
180. Anbia, M.; Ashrafizadeh, S. N., Nanoporous Lanthanum Tungstate: A Viable Adsorbent for Heavy Metals and Organic Pollutants. *Chinese Journal of Chemistry* **2010,** *28* (7), 1147-1152.

181. Bertoni, F. A.; González, J. C.; García, S. I.; Sala, L. F.; Bellú, S. E., Application of chitosan in removal of molybdate ions from contaminated water and groundwater. *Carbohydrate polymers* **2018,** *180*, 55-62.

VITA

Khalid Abdullah Alrashidi
Candidate for the Degree of
Doctor of Philosophy

Dissertation: DEVELOPMENT OF METAL OXIDE/METAL CARBOXYLATE CHEMISTRY FOR THE SYNTHESIS OF METAL TUNGSTATES, MOLYBDATES, AND FERRITES AND EXTRACTION OF IRON FROM ORES.

Major Field: Chemistry
Biographical:
Education:

Completed the requirements for the Doctor of Philosophy in Chemistry at Oklahoma State University, Stillwater, Oklahoma in May, 2022.

Completed the requirements for the Master of Science in Chemistry at Oklahoma State University, Stillwater, Oklahoma in 2018.

Completed the requirements for the Bachelor of Science in Chemistry at King Saud University, Riyadh, Saudi Arabia in 2011.

Experience:

Employed by King Saud University, Riyadh, Kingdom of Saudi Arabia as a teaching assistant from 2012 to 2016.